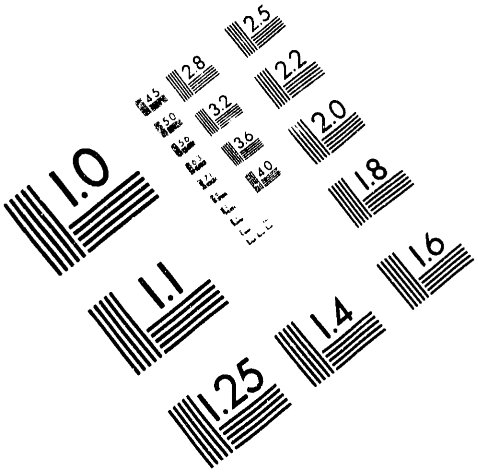

AIIM

Association for Information and Image Management

1100 Wayne Avenue, Suite 1100
Silver Spring, Maryland 20910

301/587-8202

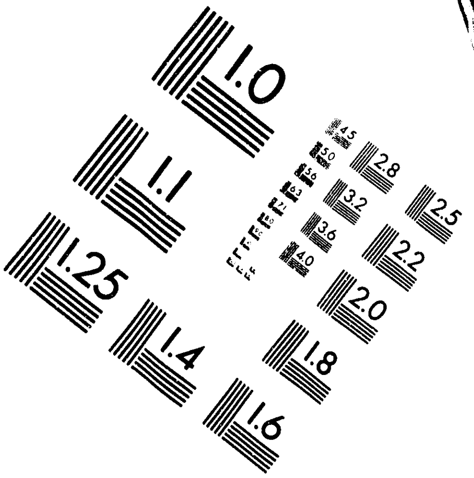

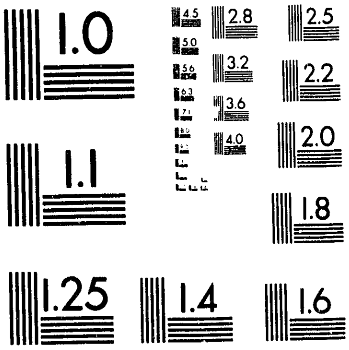

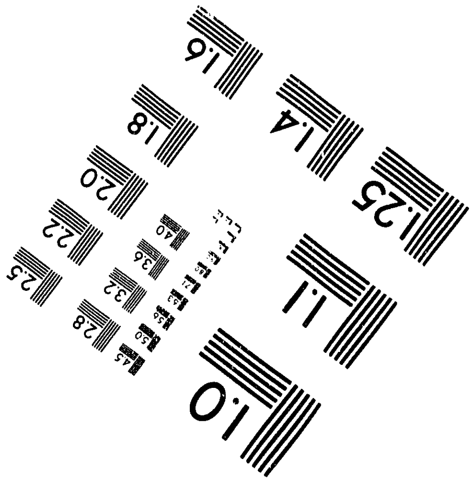

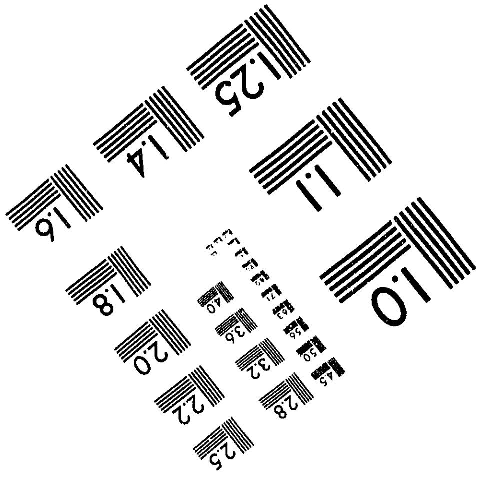

MANUFACTURED TO AIIM STANDARDS
BY APPLIED IMAGE, INC.

1 of 2

LBL-33984

Heterogeneous Slip and Rupture Models of the San Andreas Fault Zone Based upon Three-Dimensional Earthquake Tomography

William Foxall

(Ph.D. Thesis)

Earth Sciences Division
Lawrence Berkeley Laboratory
University of California
Berkeley, California 94720

November 1992

This work was supported by the Director, Office of Energy Research, Office of Basic Energy Sciences, of the U.S. Department of Energy under Contract No. DE-AC03-76SF00098.

MASTER

Heterogeneous Slip and Rupture Models of the San Andreas Fault Zone based upon Three-Dimensional Earthquake Tomography

Copyright © 1992

by

William Foxall

The United States Department of Energy has the
right to use this thesis for any purpose whatsoever
including the right to reproduce all or any part thereof.

ABSTRACT

Heterogeneous Slip and Rupture Models of the San Andreas Fault Zone based upon Three-Dimensional Earthquake Tomography

by

William Foxall

Doctor of Philosophy in Geophysics

University of California at Berkeley

Professor Thomas V. McEvilly, Chair

Crustal fault zones exhibit spatially heterogeneous slip behavior at all scales, slip being partitioned between stable frictional sliding, or fault creep, and unstable earthquake rupture. An understanding the mechanisms underlying slip segmentation is fundamental to research into fault dynamics and the physics of earthquake generation. This thesis investigates the influence that large-scale along-strike heterogeneity in fault zone lithology has on slip segmentation. Large-scale transitions from the stable block sliding of the Central Creeping Section of the San Andreas fault to the locked 1906 and 1857 earthquake segments takes place along the Loma Prieta and Parkfield sections of the fault, respectively, the transitions being accomplished in part by the generation of earthquakes in the magnitude range 6 (Parkfield) to 7 (Loma Prieta). Information on sub-surface lithology interpreted from the Loma Prieta and Parkfield three-dimensional crustal velocity models computed by Michelini (1991) is integrated with information on slip behavior provided by the distributions of earthquakes located using the three-dimensional models and by surface creep data to study the relationships between large-scale lithological heterogeneity and slip segmentation along these two sections of the fault zone. The velocity models are calibrated using published velocity-pressure and velocity-temperature data for basement rock types that outcrop within the study areas, and both models are in good agreement with published refraction surveys. Both image a large anomalous high-velocity body at mid-crustal depths underlying the fault zone that probably has a gabbroic or other mafic composition. The active plane of the San Andreas fault cuts through each body. A model is proposed in which these high-velocity bodies act as barriers that arrest stable sliding. Concentration of stress on the strong, frictionally unstable fault contacts within the bodies causes them to evolve as the asperities that nucleate the Loma Prieta and Parkfield earthquakes. The fault system also responds to the barriers by transferring slip to secondary structures and attempting to slide around the barriers on new splay faults that form at frictionally favorable lithological contacts. It is proposed that this is often the fundamental mechanism underlying the observed relationship between the segmentation of earthquake rupture and fault geometry. Development of splay faults is the mature stage of the formation of a damage zone of intense fracturing in front of the barriers. The damage zone at Parkfield is imaged directly as a prominent positive V_p/V_s anomaly under Middle Mountain. Three-dimensional imaging of lithological barrier/asperities by earthquake tomography represents a significant step forward in quantitative modeling of fault zone dynamics, since it provides not only the locations and geometries of the barrier/asperities but also realistic estimates of their fracture, frictional and *in situ* elastic properties.

Thomas V. McEvilly 21 Nov 92

Thomas V. McEvilly

Dissertation Committee Chair

In memory of my mother and father,

Molly and Bill Foxall

TABLE OF CONTENTS

ACKNOWLEDGMENTS

Dr. Tom McEvilly served as my advisor throughout my graduate career at Berkeley, and as chair of my dissertation committee. Tom has been a constant, tolerant and energetic source of support and encouragement to me, for which I am deeply grateful. His unflagging efforts in Washington and Menlo Park drumming up funds are appreciated by us all at the Center for Computational Seismology, and to me personally have meant that I have never had to worry about financial support. Dr. Lane Johnson has continued to stimulate my interest in every aspect of seismology, and has always been available and willing to give freely of his time and knowledge. Dr. Neville Cook helped to awaken my interest in the mechanics of crustal deformation and the earthquake source.

My warmest thanks to my colleague and friend, Dr. Alberto Michelini, who did all the really hard work upon which this thesis is based. From our earliest graduate student days, beating sense out of Bruce Bolt's problem sets in the Cafe Depresso, or beating to windward on the Bay, Alberto has always been my chief source of inspiration -- although, judging from the seemingly acrimonious flavour of our debate, others may have doubted it.

My work at Berkeley has been greatly aided by the computing and other resources provided by the Center for Computational Seismology at the Lawrence Berkeley Laboratory, and I thank Tom McEvilly, Ernie Majer and Karl Olson, among others, for maintaining the excellence of this facility. Karl has also succeeded in keeping me humble on the squash court. Barbara Jones, Andre Bell, Pat Bronnenburg and Dee Schmidt display saint-like patience, good humour and tolerance in sheltering students from the harsh reality of a bureaucratic world.

Thanks to Eleni Karageorgi, Tom Daley, Peter Fuller, Valeri Korneev, and my fellow students, Mike Antolik, Bob Nadeau, Joel Ita and Don Vasco, for their help and support and stimulating discussions over the years. Christy Butterfield has been a stalwart and faithful friend, and provided invaluable assistance in

the final preparation of this dissertation.

My amazing and wonderful children, Sarah and Sam, have given me the joy that has sustained me over the last difficult months, and have borne my preoccupation with understanding and without complaint. My graduate career would never have been possible without the security provided by the support and sacrifice of my wife, Mary. To her I owe the greatest debt of all.

This work was supported by the U.S. Department of the Interior, U.S Geological Survey, under NEHRP award 14-08-0001-G1840, through the Director, Office of Energy Research, Office of Basic Energy Sciences, of the U.S. Department of Energy under contract No. DE-AC0376SF00098.

CHAPTER 1

INTRODUCTION

Displacement on active faults within the brittle crust of the Earth takes place either as stick-slip, a mechanical instability that results in earthquakes, or stable sliding, which is a quasi-static process termed fault "creep". Partitioning between these two modes of slip along the strikes of crustal fault zones has become recognized as a fundamental characteristic of the faulting process at all scales. An understanding of the underlying causes of slip segmentation would allow us to design appropriate techniques to best model fault zone deformation, dynamics and evolution, and would provide realistic data on fault zone structure and the properties of fault zone materials upon which to base the models. This in turn would provide constraints, such as the locations, geometries and elastic properties of rupture planes, on models of individual earthquake ruptures to enhance our fundamental understanding of the physics of the earthquake source. From the practical standpoint of seismic risk assessment, not only would we be able to predict where along major fault zones damaging earthquakes are likely to be located, but also, through adequately constrained modeling of the earthquake cycle, when such earthquakes might occur. Similarly, properly constrained modeling of potential rupture zones would allow more accurate prediction of the strong ground motions produced by earthquakes.

To date, most studies of the causes of fault zone segmentation have concentrated on the geometrical segmentation evident in the zones at the Earth's surface. While geometry-based theories can explain, at least in part, how earthquake ruptures are nucleated and arrested, they fall short in addressing the more fundamental question of slip segmentation along fault zones as a whole. This thesis explores the role of the second potential cause of slip segmentation - heterogeneity in fault zone material properties due to variable lithology. Surface mapping tells us that the geology along the strike directions of most major fault zones is highly variable, and the significance of lithological heterogeneity as a potential cause of slip segmentation has long been recognized but has remained almost uninvestigated. This has been due to the lack until recently of tools adequate to image the lithology of fault zones at seismogenic depths. This lack is beginning to be remedied by the advent of crustal tomography using earthquakes as energy sources, the technique upon which the research described in this thesis is based. The research itself deals exclusively with the San Andreas fault zone (SAFZ) in central California, but many of the results are applicable to faults in general.

The remainder of this chapter is devoted to a review of the characteristics and scaling of fault zone segmentation, and a brief examination of the hypotheses that have been advanced to explain it. Chapter 2 examines the potential causes of slip heterogeneity in more detail in the context of current theories of fault strength and frictional stability. Chapter 3 describes the method of analysis. Chapters 4 and 5 discuss the application of the technique to two sections of the SAFZ and develops slip and rupture models of these two sections. Chapter 6 explores the generalization of these models and Chapter 7 summarizes the work.

1.1 Scaling of Slip Heterogeneity

At the largest scale, on the order of 100 km, major fault zones are observed to be divided into segments having distinctly different slip behaviors. The best studied example of such large-scale segmentation is the San Andreas Fault Zone (SAFZ) between Cape Mendocino and San Bernadino, California (Allen, 1968, 1981) (Figure 1.1). This stretch of the fault is divided into two "locked" segments, separated by a central creeping segment. The two locked segments generate infrequent major stick-slip events but exhibit a very low level of microseismicity and little or no measurable surface fault creep. The 450 km-long segment between Cape Mendocino and San Juan Bautista and the 300 km-long segment between Parkfield and San Bernadino were entirely ruptured by the great earthquakes of 1906 and 1857, respectively. In sharp contrast, the measured surface creep rate along the 150 km-long Central Creeping Section increases from less than 1mm/yr at either end to greater than 30 mm/yr along its 50-km long central zone (Burford and Harsh, 1980), but apparently does not generate major earthquakes. Since the creep rate along the central zone approximately accounts for the entire relative motion between the Pacific and North American plates (DeMets et al., 1987), slip is essentially purely stable block sliding here whereas it is essentially stick-slip along the locked segments. Present research results suggest that stable sliding on the scale observed on the

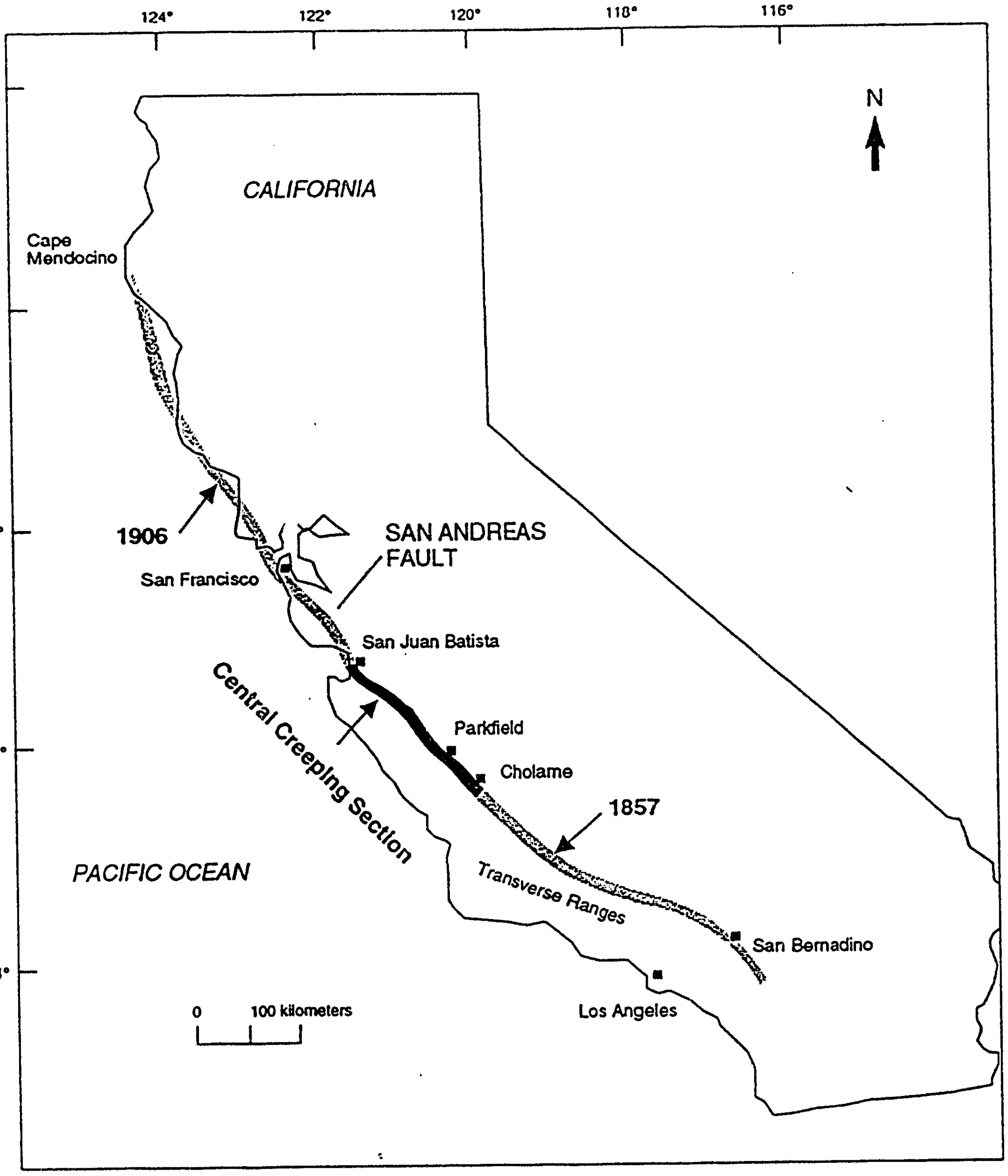

Figure 1.1: Map of California showing segmentation of the San Andreas fault.

Central Creeping Section is unique among crustal fault zones. However, the large, well-defined contrasts in slip behavior that result from its presence provide an ideal opportunity to study slip segmentation in detail

Examination of the Central Creeping Section reveals that it is itself segmented at scale lengths on the order of 10 km between the constant creep-rate central zone and the transition zones to the NW and SE along which the creep rate declines. Microseismicity accompanies stable sliding within all three of these zones, but the NW and SE transition zones also generate relatively frequent earthquakes in the magnitude range 5 to 6. Evidently slip within these transition zones is partitioned between stable and unstable sliding. Slip heterogeneity along the Central Creeping Section is clearly revealed by the strong correlation between intense clusters of microearthquakes and steep spatial gradients in the creep rate (Wesson et al., 1973).

Slip heterogeneity at the 10-100 m scale is revealed in kinematic and dynamic models of the ruptures of individual earthquakes, which usually show complex variations in slip velocity along the rupture surface (e.g. Beroza and Spudich, 1988; Steidl et al., 1991), and at even finer scales in the rich high-frequency content of recorded seismograms (e.g. Haskell, 1964; Madariaga, 1977; Hanks and McGuire, 1981).

An important aspect of slip heterogeneity is its stability in space and time. Paleoseismicity studies of, for example, the 1857 segment of the SAFZ (Seih, 1984: Seih and Jahns, 1984) show that major earthquakes repeatedly rupture the same planes within the fault zone and suggest that the segments retain their identities over time periods at least as long as 10^4 years. Within the historical seismicity record, the moderate earthquakes that occur along the SE transition segment of the central creeping section of the SAFZ at Parkfield apparently repeat every 22 years, on average. These events also appear to rupture exactly the same planes within the fault zone, as shown both by the almost identical seismograms that these events write (Bakun and McEvilly, 1984) and by the identical coseismic surface ruptures they produce (Brown, 1970). These observations have led to the "characteristic earthquake" concept (Shimazaki and Nakata, 1980; Bakun and McEvilly, 1984: Schwartz and Coppersmith, 1984), in which certain fault segments rupture repeatedly in similar earthquakes.

There is evidence that characteristic fault behavior also operates at small scales. Within the SAFZ Central Creeping Section the distributions of both seismicity and creep appear to be stationary in time for periods of at least tens of years (Wesson et al., 1973). A very striking illustration of this stationarity at scales as small as 10 m is provided by results of high-resolution studies of microearthquakes within the nucleation zone of the Parkfield earthquakes (Foxall and McEvilly, 1987, 1988; Antolik et al., 1991). Approximately 50 percent of the earthquakes within this zone recorded by the Parkfield downhole, broad bandwidth High Resolution Seismic Network belong to clusters of events that write identical seismograms to frequencies as high as 75 Hz, and are therefore located within tens of meters of each other. The clusters are concentrated on fault patches having dimensions on the order of 100 m. Members of the clusters occur over time periods ranging from seconds to (at the time of writing) several years, which indicates that the repeated failure of the same limited number of fault patches is an important, and perhaps the dominant, mode of minor seismic failure accompanying stable sliding within this zone. A second important result of this work is that seismograms from neighboring clusters are quite different. This can even be the case when a cluster member is closer to events in the adjacent cluster than it is to those within its own cluster, which illustrates the heterogeneity of the fault zone at this small scale. In fact, we see no fine-scale limit.

1.2 Geometrical and Material Heterogeneity of Fault Zones

The stability of the distributions of seismicity and fault creep suggests that segmentation of slip results from heterogeneity of strength and frictional properties along fault zones. Earthquake ruptures apparently are repeatedly nucleated and arrested by the same local features along faults, the arresting features delimiting the fault segments. In essence, what is required is variation in the *effective* fracture strength and frictional stability of the fault with respect to the tectonic loading at the fault plane. Variations in effective strength or frictional properties can be achieved by heterogeneity in either fault zone geometry (King and Nabelek, 1985; King, 1986) or in the intrinsic strength and frictional properties of fault zone materials (Husseini et al., 1975), including their degree of fluid saturation and pore pressure.

1.2.1 Summary of Present State of Knowledge

1.2.1.1 Geometrical Segmentation

Faults are geometrically segmented even when viewed as a single trace on a small-scale map . The SAF, for example, has prominent large-scale variations in geometry at scales on the order of 100 km, an extreme example being the 30° change in strike at the "Big Bend" where the SAFZ enters the California Transverse Ranges (fig. 1.1). *En echelon* offsets along the fault can be as large as 1.5 to 2 km, such as the right step at Cholame.

Viewed in more detail, fault zones in general are geometrically complex zones of brittle deformation. At all scales, they appear as sets of anastomosing and offset traces and splays (Brown, 1970; Tchalenko and Berberian, 1975). In a detailed study of faulting in three dimensions, Wallace and Morris (1986) found that individual trace segment lengths varied from a few meters to a few km, and they observed large changes in strike and dip over distances as small as a few hundred meters, both along-strike and vertically. At the finest scales, Wallace and Morris (1986) and Chester and Logan (1986) found that an individual fault consists of a gouge layer at its center and a breccia zone of sheared rock grading outwards to a zone of fracture and subsidiary faults. Thus, size scales range from the dimensions of gouge grains through increasingly larger breccia blocks to the lengths of fault segments.

There have been numerous detailed studies that indicate that earthquake ruptures can be nucleated and arrested or impeded at even relatively modest fault bends and offsets (King and Nabelek, 1985; Sibson, 1986. King, 1986). For example, the 1857 earthquake on the southern SAF probably nucleated close to the prominent 1.5-2 km offset in the main fault trace near Cholame (Bakun and McEvilly, 1984): Lindh and Boore (1981) argue that the 1966 Parkfield earthquake nucleated at a slight (5°) bend in the main fault trace and the coseismic rupture terminated at the offset at Cholame: Coseismic slip during the 1979 Coyote Lake earthquake on the Calaveras fault similarly was arrested at a fault offset (Reasenberg and Ellsworth, 1982).

It is important to note, however, that by no means all moderate and major earthquakes can be shown to be nucleated or arrested by geometrical irregularities, nor do prominent fault bends and offsets arrest all ruptures. A good example of the latter case is the 1968 Borrego Mountain earthquake on the Coyote Creek fault, which, although it was only a little larger in magnitude (M_L 6.4) than the Coyote Creek earthquake (M_L 5.9), ruptured through two offsets of similar size to that at Cholame (Sibson, 1986).

At smaller scales we have no direct evidence relating slip heterogeneity to geometrical complexity. Several workers (e.g., Aviles, et al., 1987; Scholz, 1990) have suggested that the segment lengths of the SAF main trace form a self-similar fractal set, which can be directly related to the empirical Gutenberg-Richter power law distribution of earthquake size within restricted magnitude ranges. Whereas King (1983) has shown how this association can be applied to a fault *system* as a whole, it is not clear yet that it can be applied to the immediate fault *zone* in isolation. Aviles et al. (1987) showed only that the SAF may be very weakly fractal at scale lengths greater than 1 km. Okubo and Aki (1987) obtained a similar result, but concluded that the fault zone within 1 km of the main trace is not self similar. Scholz (1990, p. 151), on the other hand, concludes that the fault trace is probably fractal up to segment lengths of about 20 km, above which fractal scaling does not apply.

1.2.1.2 Segmentation in Fault Zone Material Properties

Investigations into the role of fault zone lithology in segmentation have been more general in nature. Allen (1968) first suggested that segmentation of the SAFZ may be influenced by the types of rock in contact at the fault, and went on to say (Allen, 1981) that "... the concept that basement rock types can affect the mode of surficial strain release appears to be more and more valid." Allen's observations, however, were limited to noting that fault creep appears to coincide with the presence of serpentinite outcrops and that the 1857 segment begins where, it was believed at that time, the NE wall rock of the fault changes from Franciscan formation to Sierran basement. Irwin and Barnes (1975) refined Allen's hypothesis regarding the association of fault creep with serpentinite by pointing out that creep actually corresponds to the occurrence of the nappe of the Great Valley sequence overlying the Franciscan formation at the fault. Serpentinite occurs at the base of the Great Valley sequence as part of the Coast Range ophiolite. They pointed out that not only is the Great Valley sequence present along the Central Creeping Section of the SAFZ, but is also the eastern wall rock of the Calaveras and Hayward faults, along which creep continues to the northwest of the Central Creeping Section, rather than on the main SAF trace.

Since fluid effects on fault slip behavior are controlled by the permeability of fault zone materials and the adjacent country rocks, they can also be regarded as being related to lithology. Berry (1973) and Irwin and Barnes (1975, 1980) postulated that creep along the SAF system is related to high fluid pore pressures within the Franciscan formation NE of the fault zone. Irwin and Barnes proposed that metamorphic fluids are pressurized by the production of abundant CO_2 within the Franciscan, and flow to the fault zone through the relatively permeable Franciscan rocks where the Franciscan is capped by the low-permeability rocks of the Coast Range ophiolite. Other studies have focused on the presence and properties of fault gouge within the SAFZ (Wang et al., 1978; Stierman, 1984; Wang, 1984; Wang et al., 1986, Mooney and Ginzburg, 1986). These studies have generally indicated that the fault zone is characterized by low seismic velocities and low densities that are consistent with the presence of gouge and damage zones, but they have lacked the resolution to investigate the actual structure of the fault zone at depth.

The detailed studies of the role of fault zone geometry in slip segmentation contrast with the few, superficial studies of the role of along-strike lithological heterogeneity. Lack of progress on this front has stemmed from the difficulty inherent in attempting to relate variations in mapped surface geology to fault slip at depth in a systematic fashion. Variations in subsurface fault zone lithology have rarely been observable. This has been a result of the availability until recently of only one-dimensional crustal velocity models in earthquake seismology, and from the difficulty of imaging localized fault zones, with their often severe vertical and lateral velocity gradients, by conventional reflection and refraction techniques (Feng and McEvilly, 1983; McBride and Brown, 1986; Louie et al., 1988). Such surveys provide images of twodimensional slices of the crust, and the cost of attempting surveys at high resolution for large distances along the strike of a major fault zone would be prohibitive.

1.3 Fault Zone Imaging Using Three-Dimensional Earthquake Tomography

Computational methods for three-dimensional structural imaging using earthquake sources (e.g. Thurber, 1983; Eberhart-Phillips, 1989; Michelini and McEvilly, 1991, Michelini, 1991) have advanced during the past decade to a degree that makes it possible to define major subsurface lithologic inhomogeneities along well-instrumented active fault zones to a resolution of a few km. This is sufficient to permit study of the large- and intermediate-scale (on the order of 10-100 km) segmentation of fault zone lithology, and thus to investigate the role of inhomogeneous material properties in fault zone dynamics. Recent application of this method by Michael (1988) and Michael and Eberhart-Phillips (1991) have pointed to a general correlation between variations in seismicity along sections of the SAF system and P-velocity anomalies at depth.

In this thesis I make detailed interpretations of existing three-dimensional tomographic velocity models of the transition zones at either end of the Central Creeping Section of the SAFZ computed by A. Michelini (Michelini, 1991; Michelini and McEvilly, 1991). These sections of the fault zone, near Loma Prieta and Parkfield, are where the changes in slip mode from creeping to locked are the most dramatic and both have experienced significant earthquakes during the past 30 years Therefore, we would expect to see correspondingly large changes in fault zone structure or composition, or both, along these sections. Abundant travel time data are available from the dense seismograph coverage of each section to constrain the three-dimensional models. The models are "calibrated" against laboratory velocity data for basement rock types on either side of the fault and available seismic refraction models. This enables anomalous velocity bodies to be identified and candidate lithologies for them to be investigated. Information about fault slip is provided by the locations of earthquakes computed using the three-dimensional velocity models and from geodetic data. Information on the influence of lithology on slip stability is therefore contained in the relationships between the seismicity and surface displacement and the velocity models. I also investigate the relationships between variations in lithology and surface fault geometry.

Lithological interpretations for the Loma Prieta section are based on only the P velocity model available for this section. Both P and S velocity models are available for the Parkfield section, which provide enhanced constraint on candidate mineralogies, and also permit investigation of the role of porosity, fluid saturation and pore pressure in fault processes. In addition, the P and S models enable realistic estimates of *in situ* elastic constants to be made, which provide important input to numerical models of fault deformation.

CHAPTER 2

STRENGTH AND SLIP STABILITY OF HETEROGENEOUS FAULTS

In this chapter I examine the conditions necessary for unstable versus stable slip on a fault, and for the nucleation and arrest of dynamic rupture. I then explore the ways in which these conditions can be achieved within a fault zone in the brittle crust of the Earth. The description of fault stability is based upon current theories of frictional mechanics. The equivalence between frictional and fracture theories of dynamic failure allows concepts of fault strength to be expressed by the same set of material-dependent parameters as fault stability.

The strength of a frictional contact can be expressed as the shear stress necessary to initiate sliding at the contact by a linear constitutive law of the type (Jaeger and Cook, 1979, p.56):

$$\sigma_s = \sigma_0 + \mu\sigma_n \tag{2.1}$$

where σ_s and σ_n are the shear and normal stresses, respectively, σ_0 the cohesion and μ the coefficient of friction. To first order, base frictional strength as expressed by this equation is found to be essentially constant and the same for most rocks (including fault gouge but not some clays) above a normal stress of a few hundred bars (Byerlee, 1978), and is insensitive to temperatures below about 400° C (Stesky et al., 1974), surface roughness, and displacement and displacement rate. There are two ways to change the effective base frictional strength of a fault. Following Anderson (1951), the first way is to change the fault's orientation with respect to the local tectonic stress field, thus changing the resolved shear and normal stresses on the fault plane (see, for example, Jaeger and Cook, 1979, p.65). The second way is to introduce pore fluids at pressure P, which reduces the effective normal stress at the fault so that (2.1) becomes:

$$\sigma_s = \sigma_0 + \mu(\sigma_n - P) \tag{2.2}$$

In the absence of either variations in geometry or pore fluid pressure, the notion of what is meant by fault "strength" in the context of earthquake rupture becomes more complex. This is discussed in Section 2.2 below. It is also important to realize that Equation (2.1) tells us nothing about fault stability, which depends upon second-order perturbations about the base friction, as described in the following section.

2.1 Frictional Stability

It has long been known that μ drops appreciably from its static value to a kinetic value once surfaces in contact are in motion. This is termed "slip weakening". It is this perturbation about the base frictional strength, coupled with the response of the surrounding elastic system, that determines whether slip will be stable or unstable. If μ falls off more rapidly with displacement, u, than the elastic system, stiffness K, can respond, then a dynamic instability occurs, as expressed by (Scholz, 1990, p.74):

$$\left| \sigma_n \frac{\partial \mu}{\partial u} \right| > K \tag{2.3}$$

Slip weakening is sufficient to explain how an instability can begin but not how it can be arrested. However, laboratory experiments have shown that friction during sliding is a function of sliding velocity, rather than displacement (e.g. Dieterich, 1979; Tullis and Weeks, 1986: For a review, see Sholz, 1990, chap. 2). These velocity weakening constitutive laws provide the necessary mechanism for strength to be regained to arrest the instability after sliding has begun. In addition to a direct velocity dependence, these laws also include dependence on one or more state variables, ψ, which, in a general way, express the dependence of friction on the micromechanical state of the frictional contact as it evolves during sliding. General forms of these state- and rate-dependent laws are given by, for example, Ruina (1983) and Tullis and Weeks (1986). A single state variable form given by Scholz (1990, p.79) is:

$$\mu(t) = \mu_0 + b\psi(t) + a\,\ln(V/V^*) \qquad (2.4a)$$

$$\frac{d\psi}{dt} = -\frac{V}{D_c}\left[\psi(t) + \ln(V/V^*)\right] \qquad (2.4b)$$

where μ_0 is the base frictional strength, V^* is some reference velocity, and a, b and D_c are constants. The third term in (2.4a) gives the direct dependence on sliding velocity and the second the dependence on ψ, the evolution of which is given by (2.4b). Figure 2.1 shows the response to a step in velocity from V^* to eV^*, where I have set $\mu=\mu_l$ for $V=V^*$ From this figure the direct velocity effect is given by:

$$\mu_y = \mu_l + a \qquad (2.5)$$

at which time ψ begins to evolve to its new steady-state value at the new velocity over characteristic distance D_c, and μ drops from μ_y to its new steady-state kinetic value:

$$\mu_k = \mu_l - b \qquad (2.6)$$

Hence the dynamic stress drop from μ_l to μ_k is given by:

$$\Delta\mu = a - b \qquad (2.7)$$

and for velocity *weakening*:

$$(a - b) < 0 \qquad (2.8)$$

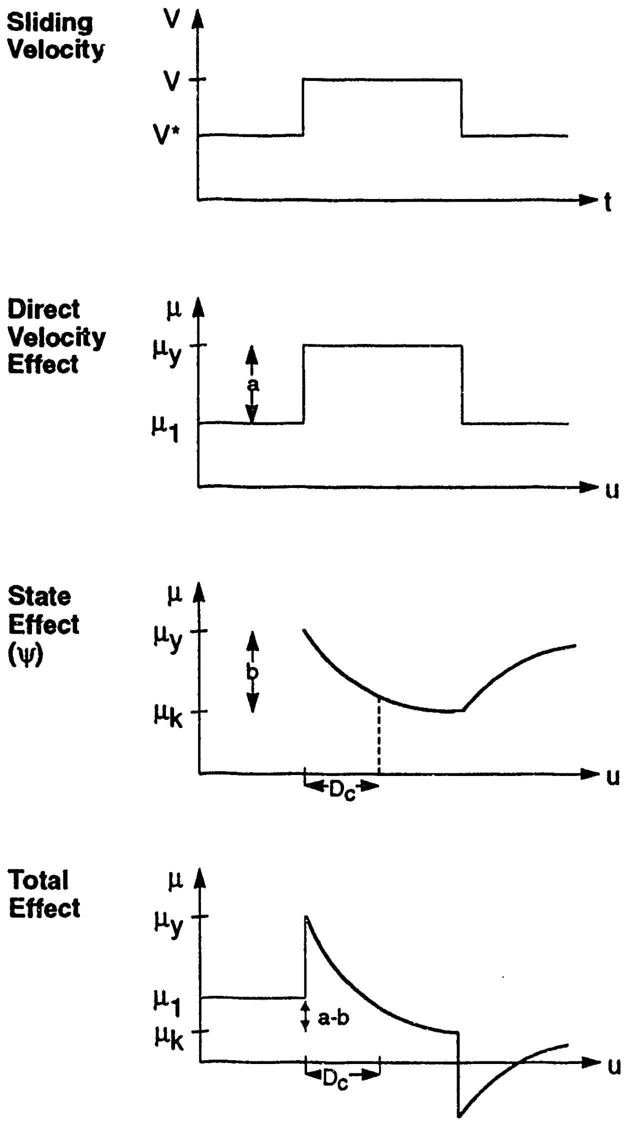

Figure 2.1: Response of rate- and state-dependent friction constitutive law to an e-fold change in sliding velocity.

From (2.4) we have:

$$\frac{\partial \mu}{\partial u} = -\frac{1}{D_c}(\mu - \mu_k) = \frac{1}{D_c}(b - a) \tag{2.9}$$

and from (2.3) the stability criterion is:

$$a - b < \frac{D_c K}{\sigma_n} \tag{2.10}$$

Rice and Ruina (1983), Gu et al. (1984) and Tullis and Weeks (1986) show that there are three possible stability states:

1. Velocity strengthening, $(a - b) > 0$: system is always STABLE.

2. Velocity weakening, $(a - b) < 0$

   System will always be UNSTABLE if the stiffness of the elastic system is less than some critical stiffness:

$$K_c = \frac{\sigma_n(b - a)}{D_c} \tag{2.11}$$

If $K > K_c$ the system is *CONDITIONALLY* UNSTABLE; i.e. it will be stable unless it experiences a sudden large velocity jump. A conditionally stable crustal fault will slip stabley under normal steady-state tectonic loading, but will fail unstably under high dynamic loading during an earthquake.

2.1.1 Factors Affecting Sliding Stability

The parameters a, b and D_c of (2.4) are identified with the micromechanical properties of the frictional contact and are therefore intrinsic material properties. In the interpretation of Dieterich (1979), for example, D_c is identified as the mean asperity radius. In this interpretation, the state variable, ψ, assumes the role of the average lifetime of an asperity contact. Thus the second-order perturbations, $\frac{\partial \mu}{\partial u}$, on the base frictional strength that govern the stability of sliding *are* very sensitive to the properties of the materials in contact, and also to the environmental factors that in turn affect those properties.

Byerlee (1970) identified the predominant mechanism of unstable sliding to be brittle fracture of asperities. Byerlee and Brace (1968) and Brace (1972) found that the following factors promote unstable sliding: (1) Low porosity, siliceous rocks, especially those containing quartz; (2) Smooth surfaces with small thicknesses of fault gouge; (3) high normal stress; and (4) low temperature. Factors which favor stable sliding are platey, soft and ductile materials, thick gouge layers, and the presence of fluids.

The dependence on normal stress is expressed in Equation (2.3) and results from an increase in the real area of contact as asperities deform under increased normal stress. The dependence on temperature in multi-mineralogic rock is more complex (Stesky, et al. 1974, Stesky, 1978), but stems from a change from brittle to ductile mechanisms of asperity failure at high temperatures. The effects of fluids are twofold. First, fluid pore pressure reduces the effective normal stress as explained above. Secondly, water (specifically) weakens asperity contacts owing to its chemical reactivity with silica. In addition, fluids significantly alter the characteristics of fault gouge, both by chemical alteration and by enhancing cataclasis and acting as lubricants (Moody and Hundley-Gough, 1980).

Apart from the environmental effects discussed above, the factors that affect slip stability are directly related to lithology. The first intrinsic lithological factor results from the presence of specific weak or ductile materials, such as serpentine, talc and calcite. Byerlee and Brace (1968) found that as little as 3 percent of serpentine drastically modified the slip behavior of gabbro towards stable sliding, and serpentine has generally been proposed as a stabilizing agent along fault zones (Allen, 1968; Irwin and Barnes, 1975). The second lithological factor, the thickness and nature of gouge, assumes importance for lithologies in general.

2.1.1.1 Wear and the Production of Gouge

Once a gouge layer has formed between two sliding surfaces, high shear strain becomes localized within it. Therefore, the fault "surface" is actually the gouge layer, and it is the properties of the gouge that determine the characteristics of frictional sliding at the contact. Sammis et al. (1986) and Chester and Logan (1986) describe the development of gouge both within natural fault zones and in laboratory experiments. The final characteristic self-similar or log-normal distributions of gouge particle sizes (Sammis et al., 1986; Marone et al., 1990)) result from comminution of sharp, angular breccia fragments produced by the damage and wear processes that are described below. Shear deformation within a mature gouge layer is localized on discrete shear planes within the gouge and at the gouge/rock (or gouge/damage zone) interface, and takes place by a combination of grain boundary sliding and rotation, and dilatation. Chester and Logan (1986) observed significant variations in the stiffness and strength of the gouge layer along strike arising from small-scale variations in the properties of the wall rocks and from localized geometrical irregularities. They go on to describe the development of the damage zone between the core gouge layer and intact rock resulting from continued fault displacement. The damage zone grades outwards through increasingly larger breccia fragments to fractured rock and subsidiary faults.

Marone et al. (1990) investigated the dependence of sliding stability on gouge thickness in terms of a rate- and state-dependent constitutive law of the type outlined above. They found that the parameter (a - b) is directly proportional to gouge thickness. Therefore, thick gouge layers are velocity srengthening and inherently result in stable sliding. Their results indicate that this velocity strengthening is the result of dilatancy, which means that in natural fault zones stable sliding is favored in unconsolidated gouge or shallow sediments. This introduces a further dependence on normal stress, since increasing normal stress will compact granular materials. The parameter D_c was found not to be a function of gouge particle size or layer thickness.

Three main frictional wear mechanisms have been identified (Scholz and Engelder, 1976; Engelder and Scholz, 1976; Logan and Teufel, 1986; Scholz, 1990, chap.2): (1) Brittle fracture of asperities; (2) Plastic deformation of asperities followed by shearing off of the asperities (adhesive wear); and (3) Ploughing of asperities through the opposite surface. The first mechanism characterizes the contact of two hard rocks, the second the contact of two soft rocks, and the third the sliding of a hard rock across a soft one. Thus, for example, wear at a sandstone/sandstone contact takes place by brittle fracture of quartz asperities, at a limestone/limestone contact by flattening and shearing of calcite asperities, and at a sandstone/limestone contact by ploughing of quartz asperities through the calcite substrate of the limestone. (Scholz, 1990, p.61).

In general, wear between rocks of contrasting hardness, but when both hardnesses are relatively high, involves both Mechanisms 1 and 3. The asperities fractured off by Mechanism 1 become sharp, angular gouge fragments. In addition, microfracturing behind an asperity sliding across the opposite surface results in the formation of relatively large particles which are eventually plucked out of the substrate. These "pluck-outs" significantly increase the volume of gouge produced (Moody and Hundley-Gough, 1980). The plucking process is particularly important when there is a significant hardness contrast between the two surfaces and Mechanism 3 operates in addition to Mechanism 1. This is because the lower grain boundary strength of the softer rock allow microfracturing to occur more easily.

In summary, laboratory results indicate that abrasive wear and plucking are the predominant mechanisms of gouge production in quartzo-feldspathic rocks. The dominant factor controlling the volume of gouge produced appears to be the hardness ***contrast*** between the surfaces in contact. Distinction between the three basic mechanisms described above is based upon the hardnesses of the individual mineral constituents of the rocks. However, the plucking mechanism appears to depend on *bulk* hardness, which is a measure of the grain boundary strength of the rock. This was suggested by Scholz (1990, p.70), who compared the wear rates at a sandstone/sandstone contact with those at a granite/granite contact. Although the significant mineral hardness of both rocks is that of quartz, the wear rate of the sandstone was 3 to 4 times higher than that of the granite. This difference is explained by plucking, the bulk hardness (as measured by uniaxial strength) of sandstone being about three times lower than that of granite.

I have discussed in this section the basic theory of slip stability as it is described by state-and rate-dependent frictional laws, and the factors that determine slip stability in nature. The main limitation at present in applying these empirical laws is uncertainty in scaling the laboratory-derived values of the parameters (a - b) and D_c to crustal faults. In particular, no guides presently exist as to what might be appropriate values for D_c on crustal faults. In order to obtain geophysically reasonable results, Tse and Rice (1986) had to assume a value for D_c of about 1 cm, which is three orders of magnitude greater than laboratory-determined values. The constitutive laws have been investigated in the laboratory for only a few of the rock types likely to be encountered in fault zones. In particular, the stability behavior of different rock types in contact has not been investigated, and no wear data presently exist for frictional sliding between quartzo-feldspathic rocks having different hardnesses.

Further application of these ideas to crustal fault zones is deferred until I have discussed the concept of fault strength and described a unified fault model.

2.2 Fault Strength

Current models of earthquake nucleation and arrest of dynamic rupture propagation envision a fault as having an heterogeneous distribution of strength. However, as I noted at the beginning of this chapter, according to Byerlee's law, the base frictional strength should not vary significantly over a fault plane. For a more or less straight fault, then, and in the absence of pore fluid effects, how can variations in frictional "strength" be achieved? Clearly the "strength" incorporated into the dynamic rupture models cannot be the base frictional strength.

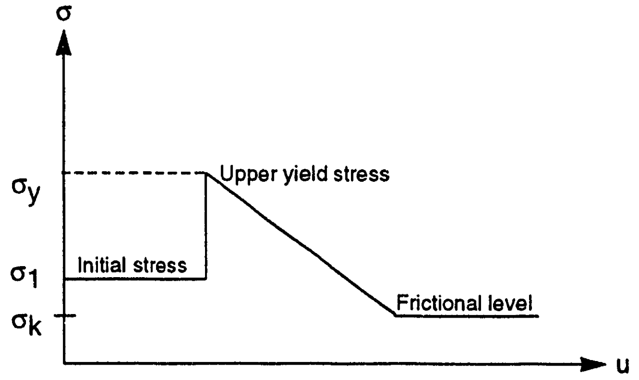

Figure 2.2: Slip-weakening instability model.

Fracture mechanics treats a slipping fault as propagating shear crack. For propagation, the crack driving force per unit length of crack extension, G, must exceed a critical value, G_c. The crack driving force at any point along the crack front is supplied by the local applied shear stress, σ_l. In the case of dynamic rupture, σ_l is the sum of the local ambient shear stress and the dynamic stress field in front of the propagating crack. Behind the crack front, the crack slips at its kinetic frictional level, σ_k. G_c corresponds to the intrinsic fracture strength of the material, σ_y, the crack propagating dynamically when σ_l reaches σ_y. In order for the stress at the crack front to remain finite, the stress must fall from σ_y to the frictional level, σ_k, over a finite distance, d_0, immediately behind the crack front, which means that a critical crack length ("nucleation length") must be attained before dynamic rupture can propagate. A crack-front slip weakening model of this type (Andrews, 1976) is shown in Figure 2.2. In this fracture-mechanical formulation, G_c and σ_y are material properties that can vary over the fault surface, thus providing the source of one type of strength heterogeneity.

Comparing Figures 2.1 and 2.2 we see that the form of the fracture slip-weakening model is the same as the state- and rate-dependent frictional model if σ_y is set equal to $\mu_y \sigma_n$. This says that the direct analog of the fracture strength σ_y must be the friction level that results from the direct velocity effect in Equation 2.4a, which is always positive. Therefore, this frictional strength depends on the parameter a and is a *material* property (as required by its equivalence to σ_y) which can vary over the fault plane under the influence of the same factors that control frictional stability. For these two equivalent formulations of dynamic fault rupture we define the quantities dynamic stress drop:

$$\Delta\sigma = (\sigma_l - \sigma_k) = (a - b) \sigma_n \qquad (2.12)$$

and "strength excess":

$$(\sigma_y - \sigma_l) = a \sigma_n \qquad (2.13)$$

The strength parameter that governs dynamic rupture is the dimensionless ratio of the strength excess (i.e. the increase in stress above σ_l required to initiate dynamic rupture) to stress drop (Das and Aki, 1977; Okubo, 1989; Scholz, 1990, p.170):

$$S = \frac{\sigma_y - \sigma_l}{\sigma_l - \sigma_k} = \frac{a}{a - b} \qquad (2.14)$$

S is a measure of strength in that it expresses the resistance of a fault to dynamic rupture, and is again a material property. Note that because S is dependent on σ_l it may vary through the earthquake cycle. In particular, S depends on the previous history of fault rupture, since σ_l includes contributions from dynamic loading by previous earthquakes as well steady-state tectonic loading. The use of the word "strength" throughout the remainder of this thesis, unless otherwise qualified, refers to the fracture strength, σ_y, and its frictional equivalent.

2.3 Models of Fault Stability and Strength Heterogeneity

I have shown how two measures of fault strength, S and σ_y, can be expressed in terms of the same parameters that control fault stability. This enables a unified heterogeneous fault model to be developed that combines concepts of earthquake nucleation and arrest with partitioning of slip stability. For this purpose it is useful to introduce the "seismic coupling" parameter, χ, which is defined as the ratio of coseismic moment release rate to total moment release rate as calculated from geological slip rate or from relative plate motion (Scholz, 1990, p.284). This parameter is a measure of the degree of stability of a fault.

Two models have been proposed to explain earthquake nucleation and arrest and the observed heterogeneity in dynamic rupture during earthquakes. These are the barrier and asperity models. The barrier concept was originally introduced to explain the arrest of dynamic rupture at localized "high-strength" patches on a fault (Das and Aki, 1977; Madariaga, 1977; Aki, 1979; Papageorgiou and Aki, 1983a,b). A barrier, therefore, is a patch having relatively high rupture resistance, S. Equation (2.14) shows that this can be achieved in two ways. The first is that the intrinsic strength of the fault at that point, σ_y, is high. This is termed a "strength barrier" (Aki, 1979) or "fracture energy barrier" (Husseini et al., 1975) and is a permanent feature of the fault. The second way to achieve high S is for the local applied stress, σ_1, available to drive the dynamic rupture to be low. This is termed a "driving stress barrier" (Husseini et al., 1975) or "relaxation barrier" (King, 1986). Since σ_1 may depend on the stage in the seismic cycle the fault patch is at, a relaxation barrier may not be a permanent feature. On the other hand, σ_1 on a fault segment that always slides stably will always be close to zero, so such a segment can act as a permanent relaxation barrier. It is important to note that in order to achieve the long-term segmentation demanded by the characteristic earthquake model, certain barriers must be permanent, and not rely on variations in σ_1 through the seismic cycle for their existence.

An asperity was originally defined as a area having relatively high stress drop on a fault that nucleates dynamic rupture and does not slip otherwise (Lay and Kanamori, 1980; Lay et al., 1982; Rudnicki and Kanamori, 1981; Kanamori, 1986). The high stress drop is usually attributed to a large σ_1 in (2.12) resulting from stress being concentrated at "strong" patches on a fault plane (analogous to asperities in the micro-mechanics of friction) during tectonic loading. If such an asperity is a patch that has a high σ_y, then that patch could evolve from a barrier to an asperity through the seismic cycle: S falls from the high value it has when the patch acts as a barrier as σ_1 increases due to loading by the arrest of successive earthquakes and at the steady-state tectonic rate. The patch fails when σ_1 equals σ_y (S=0). Because σ_y is high, σ_1 at the time of failure is also high, so the resulting stress drop is large and the patch acts as an asperity.

According to the definition above, an asperity need not necessarily be a particularly strong patch on the fault, but merely one that fails *unstably* and nucleates dynamic rupture on the surrounding fault plane. This could happen at a low value of σ_y if, for example, σ_k were small. Therefore, the essential attribute of an asperity, unstable slip, derives from the frictional constitutive law that governs slip stability on that part of the fault compared with the surrounding fault. Following Scholz (1990, chap.7), this realization, together with the fact that the strength, σ_y, of a fault can also be expressed in terms of the same constitutive parameters, leads to a heterogeneous fault model that is based upon frictional stability. In this model each part of a fault can behave in one of the following ways:

1. Always slide stably. This is the velocity strengthening case, for which $(a - b) > 0$ in Equation (2.10). This behavior characterizes creeping parts of a fault. $\sigma 1$ is low, and these parts of a fault can act as relaxation barriers to arrest earthquake rupture. χ is zero. The central zone of the Central Creeping Section of the SAFZ is an example.

2. Slide stably under steady-state tectonic loading, but unstably under dynamic loading. This is the *conditionally stable* case for which $(a - b) < 0$. This behavior characterizes the "locked" parts of faults, which do not nucleate earthquakes but which rupture dynamically during earthquakes. In

this case we can regard the "locked" parts of fault zones as creeping at a very slow, perhaps imperceptible rate. χ is approximately 1. The 1906 and 1857 earthquake segments, except within the hypocentral zones and possibly where the ruptures are arrested, are examples of this kind of behavior.

3. Slip only unstably. This is the unstable case for which $(a - b) < 0$. These parts of the fault are the *asperities* where earthquakes are nucleated, and are envisioned as being of limited extent compared with the dimensions of the "locked" parts that rupture during earthquakes. χ is 1.

These are the three basic types of fault contact. Mixed zones exist containing the three basic types of contact in varying proportions. Examples of mixed zones are the NW and SE transition zones of the Central Creeping Section of the SAFZ. χ for these zones is some intermediate value between 0 and 1.

Having developed this self-consistent model of a heterogeneous fault based upon frictional stability, what remains is to explore how these stability transitions can be achieved along the strike of a fault zone.

2.4 Stability Transitions

2.4.1 Stability Transitions with Depth

Empirical laws of the type described in Section 2.1 have been applied to crustal faults to investigate transitions between stable and unstable sliding with depth. Tse and Rice (1986) obtained a realistic simulation of the seismic cycle and depth distribution of earthquakes on the SAF by using laboratory-derived relationships between $(a - b)$ and pressure and temperature. In this model, the bottom of the seismogenic zone occurs as a temperature-induced transition from unstable to stable sliding. The upper bound of the seismogenic zone is similarly identified as an unstable-stable transition caused by the reduction of normal stress and changes in the stiffnesses of the surrounding rocks at shallow depths, according to Equation (2.3). Marone and Scholz (1988) proposed an alternative explanation of this upper stability transition based upon the intrinsic properties of the fault zone materials. In this model, the transition to stable sliding results from the inherent velocity strengthening properties of poorly consolidated fault gouge or sedimentary rocks at shallow depths, as described in Section 2.1.1.1. This is an indirect result of decreasing normal stress, since the degree of compaction of the gouge or sediments is proportional to normal stress.

In terms of the unified stability-based model, the one-dimensional model of a typical active crustal fault is: surface to upper stability transition, Type 1, always stable; upper stability transition to lower stability transition, Type 2, conditionally stable, or mixed Types 1, 2 and 3; lower stability transition to final brittle-ductile transition (semi-brittle zone), Type 2. Scholz (1990, chap.7) used the compaction mechanism of Marone and Scholz (1988) in his application of the stability-based heterogeneous fault model to subduction zones. In this application, variations in (a -b) are a function of compaction of subducted sediments under varying normal stress.

2.4.2 Stability Transitions Along Fault Strike

The factors that are responsible for the vertical stability transitions discussed above are temperature and pressure. In the along-strike dimension we are faced with a different set of choices. At a given depth within the seismogenic range, the temperature does not vary sufficiently to induce slip stability transitions, and the lithostatic pressure is essentially constant. To account for along-strike stability transitions, therefore, we are left with a choice of variations in effective normal stress caused by fault geometry or fluid pore pressure, or variations in the properties and amounts of fault zone materials brought about by lithological heterogeneity or by alteration by fluids.

The geometry-based models described in Chapter 1 play an important role in explaining nucleation and arrest of dynamic rupture along fault zones. Geometry, therefore, provides one type of physical barrier.

Fault steps are strength barriers (Husseini et al., 1975; King, 1986) because at them rupture on a fault segment is terminated upon encountering intact rock. Steps of either sense act in this way. Bends change the fault orientation with respect to the local driving stress (σ_1) field, thus altering the resolved normal and shear stresses on the plane. In general, compressional bends (e.g. a left bend on a right-lateral strike-slip fault) result in an increase in the normal stress across a fault and so impede rupture. Geometrical features can also act as asperities, either because they act to increase the strength, σ_y, of the fault and perhaps follow the barrier-asperity evolution model described above, or because the resolved normal stress across the fault acts either directly or indirectly (through increased gouge compaction, for example) to increase the instability of the fault at that point.

Geometry, therefore, can explain fault zone segmentation in terms of delimiting segments that rupture independently during earthquakes by providing a physical explanation for barriers and asperities. However, because geometrical irregularities are essentially localized, they cannot explain segmentation at the more fundamental level embodied in the stability-based model, and in particular, why some fault segments slip stably whereas other, roughly parallel, segments fail in earthquakes.

What we are left with, therefore, upon which to base an overall along-strike stability-based segmentation model, is a set of parameters that depend either directly or indirectly upon lithological heterogeneity along a fault zone. This considers that fluid and pore pressure effects depend upon the permeabilities of fault zone materials and the surrounding rocks. The important intrinsic lithological factors are the presence of specific weak minerals, the thickness of gouge, and the relative hardnesses of fault wall rocks from which the gouge is produced. In the case of fluid-related effects, the important parameters are porosity, permeability and degree of saturation. All of these lithological factors are to some degree amenable to study through seismic subsurface imaging.

CHAPTER 3

METHOD OF ANALYSIS

I use existing three-dimensional crustal velocity models of two sections of the SAFZ in central California computed by A. Michelini (Michelini, 1991; Michelini and McEvilly, 1991) to study the relationships among lithological heterogeneity at seismogenic depths within the fault zone and variations in slip, earthquake nucleation and rupture, and the surface geometry of the fault. The locations of the study areas, the first centered on Loma Prieta and the second on Parkfield, are shown in Figure 3.1. The Loma Prieta section straddles the final transition at Pajaro Gap from the NW end of the Central Creeping Section to the locked 1906 segment (see Section 1.1). The Parkfield section covers the final stages of the fall-off in creep rate at the SE end of the Central Creeping Section but does not extend beyond Gold Hill into the locked 1857 segment.

These two fault sections are almost ideally located to attain the objectives of the present study. The transitions from the Central Creeping Section to the locked 1906 and 1857 segments are the most profound changes in the large-scale slip behavior of the SAFZ between its ends. The Loma Prieta section includes the rupture zone of the M_L7.0 October 18, 1989 UTC Loma Prieta earthquake. The Parkfield section includes the rupture zone of the M_L5.5 June 27, 1966 UTC earthquake as far as 4 km NW of Gold Hill. Therefore, I am able to relate both the transitions in the overall slip behavior of the fault and the dynamic ruptures of two earthquakes to lithological inhomogeneities interpreted from the models.

The aftershocks of the 1989 earthquake and intense pre-mainshock, "background", microseismicity in the southeastern half of the section recorded on the U.S. Geological Survey's (USGS) permanent CALNET seismographic network provide abundant data to constrain the Loma Prieta P velocity model. The level of seismicity within the Parkfield study area is lower, but this is partially compensated for by the dense, high sensitivity seismographic coverage in this area. Most importantly, the Parkfield instrumentation records three components of ground motion, which permitted an S velocity model to be computed in addition to the

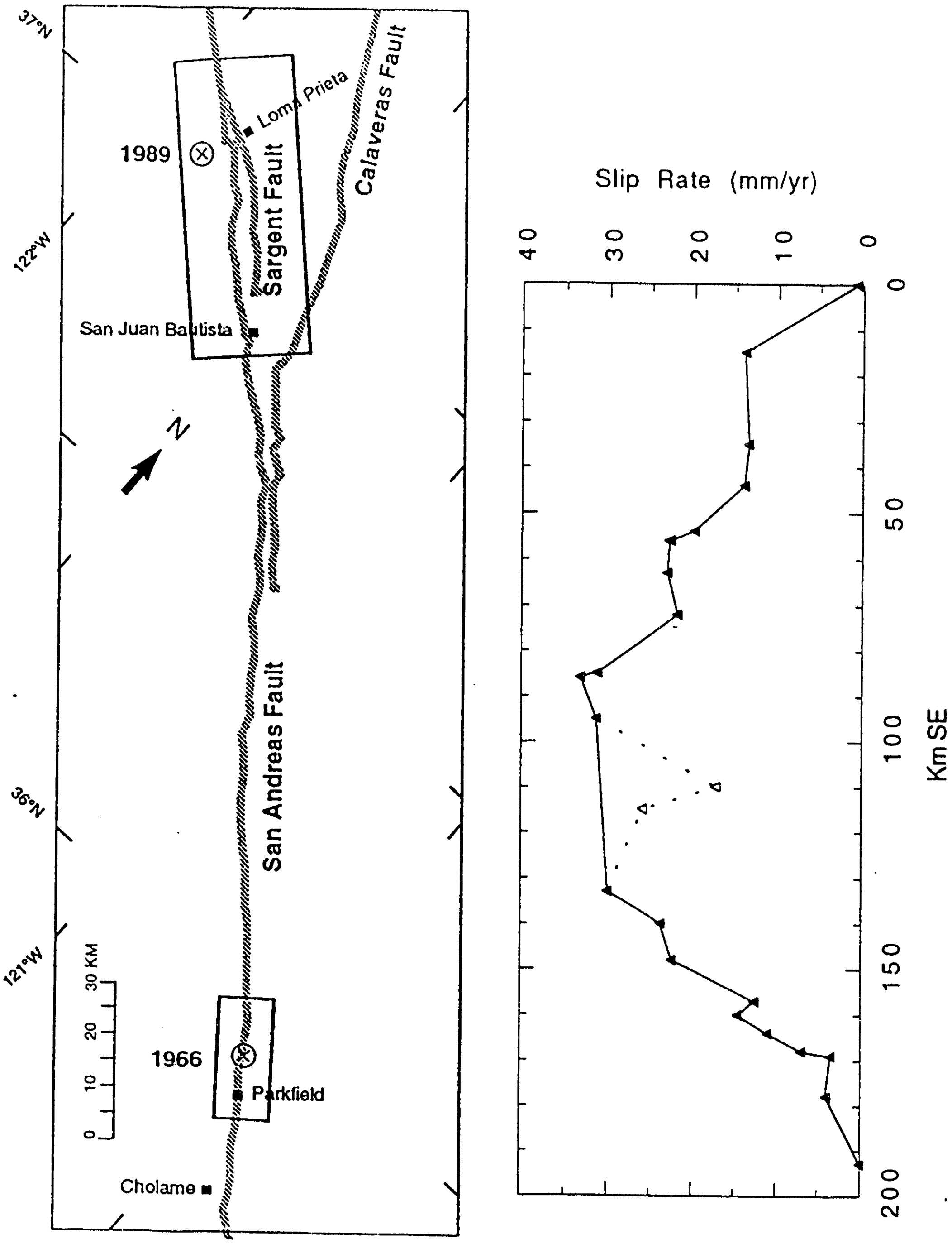

Figure 3.1: Map of San Andreas fault between Lake Elsman and Cholame showing Central Creeping Section and Loma Prieta and Parkfield study areas. Epicenters of 1989 Loma Prieta and 1966 Parkfield earthquakes shown as crosses. Creep profile based on data from Burford and Harsh (1980) and Schulz et al. (1982).

P model. In addition to the seismographic data, both sections of the fault zone are being intensely studied using a wide variety of geophysical and geological techniques. These studies, particularly the geological and geodetic investigations, provide constraint on lithological interpretations and slip distributions.

3.1 Method

The research described here is based primarily upon three data sets. The first set is the P and, for Parkfield, the S velocity model, from which lithological and structural interpretations are made. The second data set consists of the seismicity, variations in which reflect the slip stability of the fault contact. Long-term background microseismicity contains information about large- and intermediate-scale stable slip on the fault, while mainshocks and aftershocks provide information on unstable slip (dynamic rupture). The third, geodetic, data set is taken from published sources and provides information on long-term slip.

Analysis and interpretation follow the following scheme:

1. Well-resolved parts of the near-surface P velocity (V_p) model are compared with geology maps. This first enables the general quality of the model to be assessed by ensuring that the overall velocity pattern agrees with the distribution of outcrops (relatively high velocities) and surficial sediments (low velocities). The shallow models are also compared with gravity and aeromagnetic maps. Secondly, the shallow V_p model can be "calibrated" against outcropping basement lithologies.

2. To extend the interpretation to depth, "normal" basement V_p-depth ($V_p[z]$) profiles are computed for the uppermost 15 km of the crustal blocks on both sides of the SAFZ, based upon published laboratory V_p-pressure and V_p-temperature data for specific basement rocks that outcrop in the study areas or for other rocks that are possibly representative of the central California Coast Ranges. Velocity is computed as a function of depth using the following equation:

$$V(z) = V_0 + \left[g\bar{\rho} \frac{\partial V}{\partial P} + \frac{\partial V}{\partial T} \frac{dT}{dz} \right] z \qquad (3.1)$$

where V_0 is the surface velocity and $\bar{\rho}$ the average density of the rock between the surface and depth z. The first term in the brackets assumes lithostatic overburden pressure. The geotherm, dT/dz, is taken as San Andreas Profile "A" of Lachenbruch and Sass (1973), which is approximately 30°C/km in the upper 15 km of crust. The partial differentials are published velocity-pressure and velocity-temperature gradients for given rock types. Most of the published sources give actual velocities at discreet pressures and room temperature so, after the pressure values are converted to depth assuming lithostatic pressure, (3.1) reduces to:

$$V(z) = V(z,T{=}20) + \frac{\partial V}{\partial T} \frac{dT}{dz} z \qquad (3.2)$$

Certain sources do not give the temperature derivatives of velocity. For these cases an average value of $-8.(10)^{-4}$ km/s/°C was used. As the temperature derivatives of velocity are about two orders of magnitude less than the pressure derivatives, this does not introduce appreciable error.

The velocity-pressure relationship for a particular rock type derived in the laboratory at pressures greater than about 0.1-0.2 GPa (crustal depths of 4-8 km) is usually considered to be applicable at any location within the crust at or below those depths (Christensen and Salisbury, 1975). Measurements made at lower pressures, on the other hand, are in general heavily dependent upon the porosity, particularly the fracture porosity, of the particular laboratory sample, so the behavior of a specific rock type at shallow crustal depths may vary significantly from location to location. Therefore, although the laboratory data are probably representative in an average sense, they are not expected to represent near-surface *in situ* velocities in detail.

Suitable laboratory data are not available for certain rock types of known composition that outcrop within the Loma Prieta and Parkfield study areas. For these cases, theoretical rock velocities can be estimated as averages of the velocities of their major mineral constituents, as follows:

$$V_r = p_1V_1 + p_2V_2 + \cdots\cdots + p_iV_i \tag{3.3}$$

where V_r is the rock velocity, and p_i and V_i are the percentages and velocities of the constituent minerals, respectively. Following Christensen (1966a), the relationships between mineral composition and velocity can conveniently be expressed using triangle diagrams in which the apexes are the velocities of reasonably pure monomineralic aggregates of the three major constituents taken from published sources. Agreement to within a few percent between theoretical velocities calculated in this way and velocities measured in the laboratory has been found for ultramafic (Christensen, 1966a; Christensen and Salisbury, 1975), mafic (Christensen and Salisbury, 1975), and metamorphic (Christensen, 1965, 1966b) rocks, at pressures of 0.1-0.2 GPa.

3. Further constraint on the sub-surface V_p structure is provided by published regional and local seismic refraction models.

4. Vertical profiles through the three-dimensional V_p models are made at various locations, including at basement outcrops and through the surficial sediments. Comparison of these profiles with the refraction models and laboratory $V_p(z)$ data enables the surface calibration made in (1) above to be continued to depth, and major sub-horizontal subsurface geological contacts to be identified in the three-dimensional models.

5. The three-dimensional V_p models are now examined for significant anomalies with respect to the normal basement velocities. Possible rock types that these inhomogenieties could be composed of are assessed by comparing their velocities with the laboratory data.

6. Poisson's ratio, or equivalently, the V_p/V_s ratio, is especially diagnostic of certain mineralogies. For Parkfield, a V_p/V_s model is derived from the V_p and V_s models and used to refine the constraint on candidate anomalous rock types.

7. Gravity, aeromagnetic and reflection data are examined for evidence of the inhomogeneities identified, and these data are used to constrain further their lithologies.

8 Porosity and the influence of pore fluids is investigated within the Parkfield zone by interpreting the V_p/V_s model using relationships between V_p/V_s and fracture density and fluid saturation (O'Connell and Budiansky, 1974).

9. The interpreted velocity models are now correlated with the spatial distributions and mechanisms of background seismicity, mainshocks and aftershocks located using the three-dimensional models, and with published geodetic data. This enables qualitative correlation of slip stability and earthquake nucleation with the lithology and porosity models.

3.2 Joint Inversion for Velocity Structure and Hypocenter Relocations

The tomographic inversions for the Loma Prieta and Parkfield three-dimensional velocity models are described in Michelini (1991) and Michelini and McEvilly (1991), and are briefly summarized here. The method is a progressive joint inversion for P and S velocity models and hypocenter locations. The models are parameterized on a grid of nodes in terms of cubic B-spline basis functions. This parameterization yields inherently smooth models, since the B-spline basis functions are everywhere continuous up to and including the second spatial derivatives of velocity, and, being cubic, are defined on 64 contiguous nodes. This intrinsic smoothing forms part of the regularization of the inherently under-determined seismic tomography problem. The relatively accurate cubic interpolation limits bias caused by the parameterization of the model, and the smooth model retains the principal features of the velocity distribution.

The resolution matrix of the inverse solution was computed and from it a scalar "spread function" (e.g Toomey and Foulger, 1989) was derived that enables the resolution of the model to be shown graphically in a meaningful manner. The spread function for any particular node is essentially a weighted sum of the elements of the row of the resolution matrix corresponding to that node, the weights (or penalties) corresponding to the distances from that node to the rest of the nodes in the grid. The row of the resolution matrix for a perfectly resolved node will have all elements zero except for the diagonal element, and since this is multiplied by a distance penalty of zero, the spread function will be zero. Large off-diagonal elements at large distances will correspondingly rapidly inflate the spread function. Therefore, the scalar value of the spread function is a measure of how peaked (i.e close to a delta function) the estimated velocity is at a particular node. The spread function field is superimposed on the velocity model display, as shown on Figures 4.4-4.7.

The ultimate resolution of a computed model is limited by the uneven source-receiver geometry, and hence non-uniform ray coverage and sampling of the model volume, that is a fundamental problem in earthquake tomography. The V_s model is always less well resolved and inherently less accurate because of the relative paucity and lower accuracy of S travel-time data. The different ray coverages for P and S causes the V_p/V_s model to be particularly susceptible to instabilities, which appear as spurious V_p/V_s anomalies. This is mitigated to some extent by the smoothing intrinsic in the cubic B-spline parameterization. In addition, the coupling between P and S can be controlled as an *a priori* constraint, and V_p/V_s is stabilized about some preset average value. Resolution is also determined by the node spacing in the grid, since this imposes a spatial sampling limit on the data.

Michelini (1991, chap. 3) tested the performance of the method in terms of V_p and V_s resolving power, stability and accuracy by an exhaustive series of synthetic tests. The variables in these tests were node spacing, and *a priori* conditioning on damping, smoothing, ray-density weighting, and V_P-V_S coupling Michelini set up two test models. The first, a "spike" test, contained several small, intense velocity anomalies of alternating sign and having a wavelength of 2 to 3 km. The second was a simulated one km-wide low-velocity fault zone having steep, 1.2 km-wide gradients on either side, and a +0.3 V_P/V_S anomaly within the fault zone. The exact Parkfield source-receiver geometry was imbedded in both models and synthetic travel times generated by ray tracing. Node spacing in km for the spike tests was (x[across-strike], y [along-strike], z [depth]) = (2, 5, 2.5), and for the fault test (1.2, 5, 2.5). Michelini shows the results of these tests are in the (x,z) plane, which contains all of the velocity variation in the fault model, and the most severe variation in the spike model.

In general, the method recovered smooth versions of the true models within the central part of the model volume. For example, a positive spike anomaly having a width of 2 to 3 km would be imaged as a 4 to 5 km wide feature of lower (about 5%) amplitude. Positive anomalies are smeared into the adjacent lows with an attendant reduction of the core anomaly amplitude. Negative anomalies tended to be obliterated at the expense of the highs. The absolute resolving power appears from this test to be approximately 2+ km, i.e approximately the node spacing. The edges of the recovered models are generally not accurate and exhibit instabilities, but this is usually indicated by high values of the spread function. The spread function does a good job in indicating model resolution overall. Shallow structure is resolved better than deeper parts of the model because of the improved ray coverage. The S models have significantly smaller well-resolved volumes, concentrated in the middle of the model volume.

In the fault model test, the overall 3 km width of the fault zone, almost three times the node spacing, was accurately recovered, but with somewhat gentler gradients. On the high-velocity side of the fault the imaged model is accurate towards the center but velocity contours at the (apparently well resolved) edge of the model are systematically pulled about 1 km too deep. The position of the V_P/V_S anomaly was accurately recovered, but it is smeared laterally to a width of about 4 km and compressed vertically, with a corresponding 10% reduction in its core amplitude to about 1.9.

In general, the recovered models are only mildly sensitive to reasonable variations in *a priori* conditioning, except that explicit smoothing tends to degrade and de-stabilize the models. V_p/V_s conditioning was found to be effective in limiting instabilities and improving the accuracies of the V_p/V_s models, and also improved the fit of the S models in the inner parts of the model volume. Absolute hypocenter mislocations for earthquakes within well-resolved central part of the fault model average about 0.75 to 1 km, the locations being systematically too shallow by up to about 0.5 km and pulled into the high-velocity block by as much as 1 km. The across-fault mislocation systematically increased with depth.

Michelini (1991) concluded that the resolving power of the Parkfield data set is sufficient to recover the main features of the V_p, V_s and V_p/V_s structures there. For the actual Parkfield inversion, Michelini used the same node spacing [(1.2, 5, 2.5) km] as for the fault model tests. The above discussion indicates that this model should be able to resolve features as small as 2 to 3 km. Michelini also checked the robustness of the inversions with respect to the choice of grid at both Parkfield and Loma Prieta, and obtained very similar models in all cases. For Parkfield he also examined robustness with respect to the *a priori* conditioning options mentioned above, and with respect to different combinations of sub-sets of data. Here again, he found only minor differences in the resulting models.

CHAPTER 4

LOMA PRIETA

4.1 Joint Inversion

Michelini's (1991) inversion for the Loma Prieta V_p model used 5422 P-wave arrival times from 173 earthquakes - aftershocks of the October 18, 1989 earthquake and pre-mainshock "background" events (since January, 1984) recorded at a minimum of 25 and 30 local stations, respectively, of the USGS CALNET central California network. The accuracy of these well-recorded P-wave onsets is estimated to be ±0.02 sec. The starting model for the three-dimensional inversion was a one-dimensional inversion result from the linear B-splines method of Thurber (1983), a model which yielded a weighted RMS residual of 0.236 sec.

The model is discretized in the 9x11x6-point (X x Y x Z), 594-node grid shown in Figure 4.1. Node spacings are 3, 7, and 3 km, respectively, in the X, Y, and Z directions. The XY coordinate system is rotated 45° counterclockwise to align approximately along the SAF trace. Figure 4.1 also shows the 173 earthquakes and the stations used in the velocity inversion. After seven iterations the final three-dimensional model yielded a weighted RMS residual of 0.092 sec. Interpretations are conservatively based on the well-determined aspects of the model.

The part of the model volume considered in the present study is contained within the dashed box in Figure 4.1, and extends along strike from y= -45 km to y= 15 km. A total of 717 earthquakes (424 background seismicity events, the 1989 mainshock and 292 aftershocks) of magnitude (M_L) 1.5 and greater that lie within this volume were relocated with the three-dimensional model determined from the simultaneous inversion, and are shown in Figure 4.2. The mainshock focal depth is 15.9 km. Fault-plane solutions for all of these earthquakes were computed using the take-off angles of the relocations as input to the program FPFIT of Reasenberg and Oppenheimer (1985). Representative mechanisms are shown in Figure 4.2. The

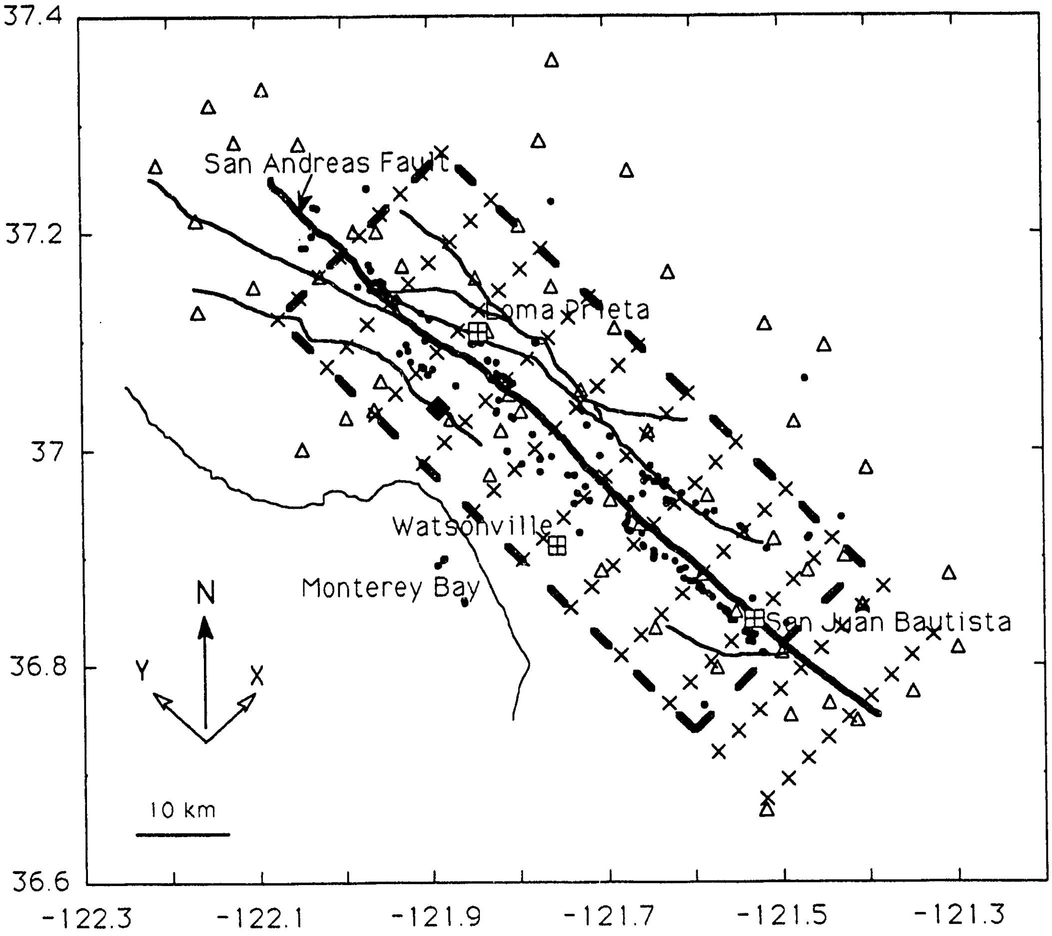

Figure 4.1: Map of southern Santa Cruz Mountains region showing horizontal distribution of node points (crosses), earthquakes (dots) and CALNET stations (triangles) used in Loma Prieta simultaneous inversion. Loma Prieta mainshock epicenter indicated by diamond. Major faults shown as bold lines. Inversion grid extends from (x,y) = (-9 km,-55 km) at lower left corner to (15,15) at upper right. Study volume (heavy dashed line) extends from y = -45 to 15 km. Based upon Michelini (1991), fig. 5.1.

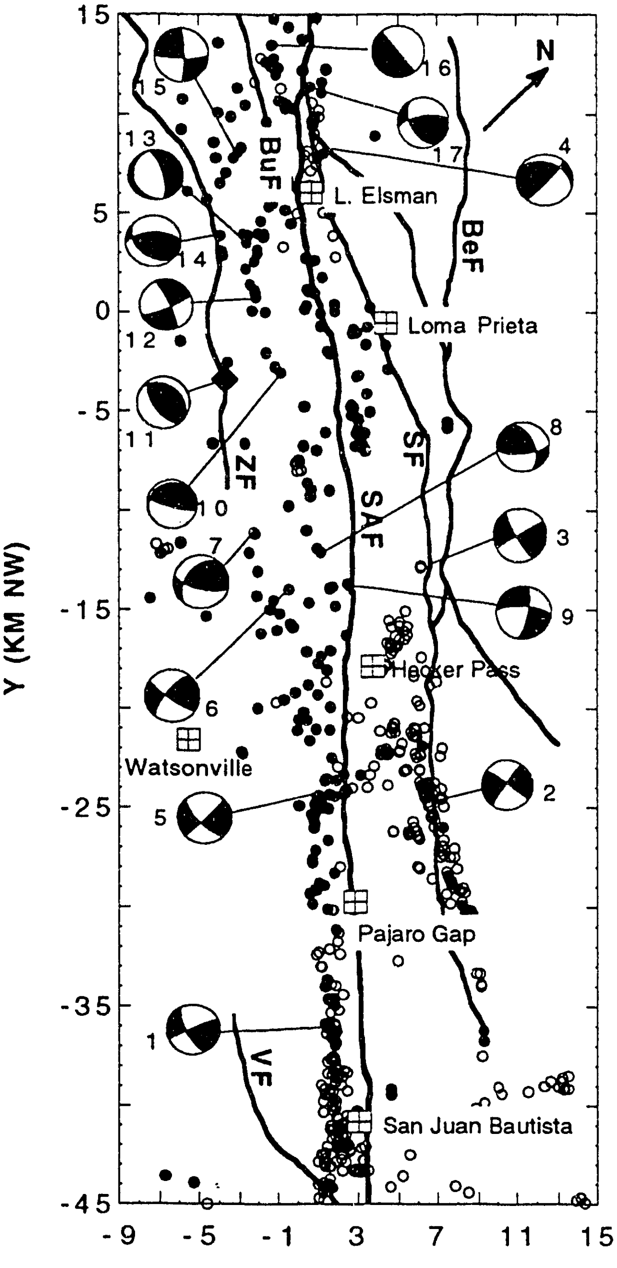

Figure 4.2: Map of Loma Prieta study area showing 1989 mainshock (diamond), October ($M \geq 2.5$) and November, 1989 ($M \geq 1.5$) aftershocks (filled circles), pre-mainshock seismicity ($M \geq 1.5$) (open circles), and representative focal mechanism solutions. Major faults: **BeF**, Berrocal; **BuF**, Butano; **SAF**, San Andreas; **SF**, Sargent; **VF**, Vergeles; **ZF**, Zayante. See fig. 4.1 for map orientation.

rotated X-Y (NE-NW) position convention of Figure 4.2 will be used in figures throughout this section on Loma Prieta.

4.2 The Loma Prieta Velocity Model

Figure 4.3 shows the map view of the near-surface (z= -3 km) V_p model for comparison with the surface geology and isostatic gravity data also shown in this figure. Map views of the model at deeper horizons are shown in Figure 4.4. Figures 4.5 and 4.6 are across-strike (SW-NE) and along-strike (SE-NW) depth sections through the velocity model at specified values of Y and X, respectively. The velocity field is shown both by contours and by color *hue* . Values of the spread function are indicated by color *saturation*, fading to white for no resolution. The hypocenters shown on Figures 4.4 - 4.6 are projected onto the planes of section as described in the individual figure captions.

4 2.1 Relation Between the Velocity Model and Surface Geology

The near-surface velocity structure in Figure 4.3 is well correlated with the surface geology and gravity data. The four major surface geological units within the area are seen in the velocity model and marked in the figure as regions I, II, III, and IV.

Region I. The elongated velocity high enclosed within the 5.2 km/s contour on the NE side of the San Andreas and Sargent faults between y= -30 and y= 12 coincides with an outcrop of Franciscan basement rocks. The Franciscan complex is a highly deformed, heterogeneous assemblage consisting chiefly (about 90%) of late Jurassic to Cretaceous altered and unaltered graywacke and shale (Bailey et al., 1964; Page, 1981; Irwin, 1990). These rocks range from unmetamorphosed graywacke to high-grade (jadeite facies) metagraywacke (Ernst, 1971; Lin and Wang, 1980; Stewart and Peselnick, 1977, 1978). To the SE of here, along the Diablo Range antiform, the Franciscan rocks are overlain by the nappe of the Great Valley

Figure 4.3: **(left)** Simplified surface geology, based on Jennings (1977); **(center)** map view of Loma Prieta 3-D V_p model at depth 3 km (below msl), contour interval 0.2 km/s; **(right)** isostatic gravity, contour interval 5 mGal. Main geologic units: **KJf** and **Ku**, Franciscan complex; **gm**, Salinian block; **gb**, gabbro, **Q**, Quaternary sediments. See fig. 4.2 for fault identification.

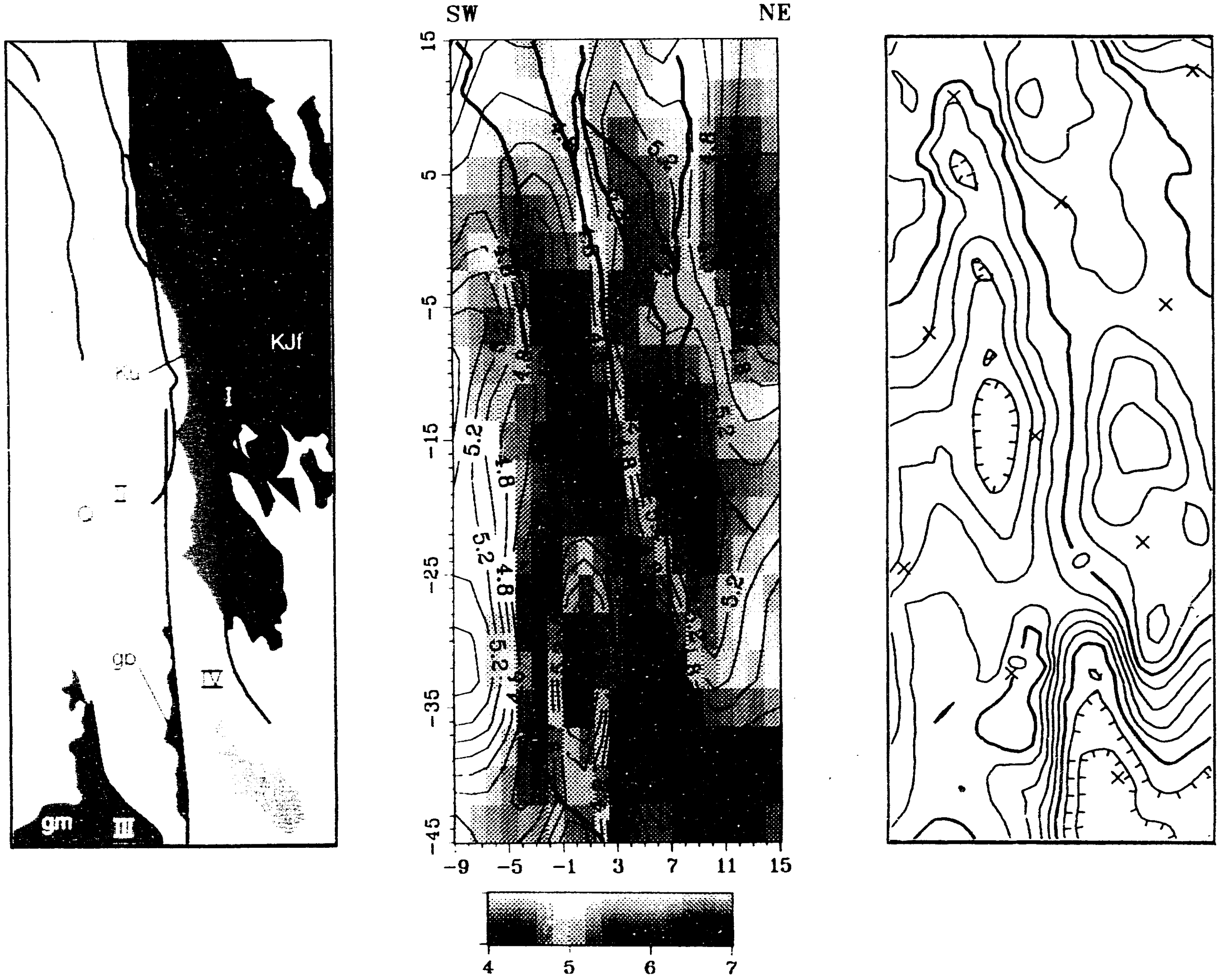
KJf
I
Ku
II
O
gb
IV
gm
III
SW
NE
15
5
−5
−15
−25
−35
−45
−9
−5
−1
3
7
11
15
5.2
4.8
4
5
6
7
0

Figure 4.3

Figure 4.4: Map views of Loma Prieta 3-D V_p model at depths (below msl) of: (**a**) 6 km; (**b**) 8 km; (**c**) 10 km; (**d**) 12 km. Contour interval 0.2 km/s. Interpretative panel in **b.** outlines anomalous high-velocity bodies. See fig 4.2 for fault identification. Filled red circle is 1989 mainshock epicenter. Aftershocks (filled black circles) and background earthquakes (open circles) projected from depth intervals: (**a**) 3-8 km; (**b**) 5-9 km; (**c**) 9-12 km; (**d**) 11-13 km.

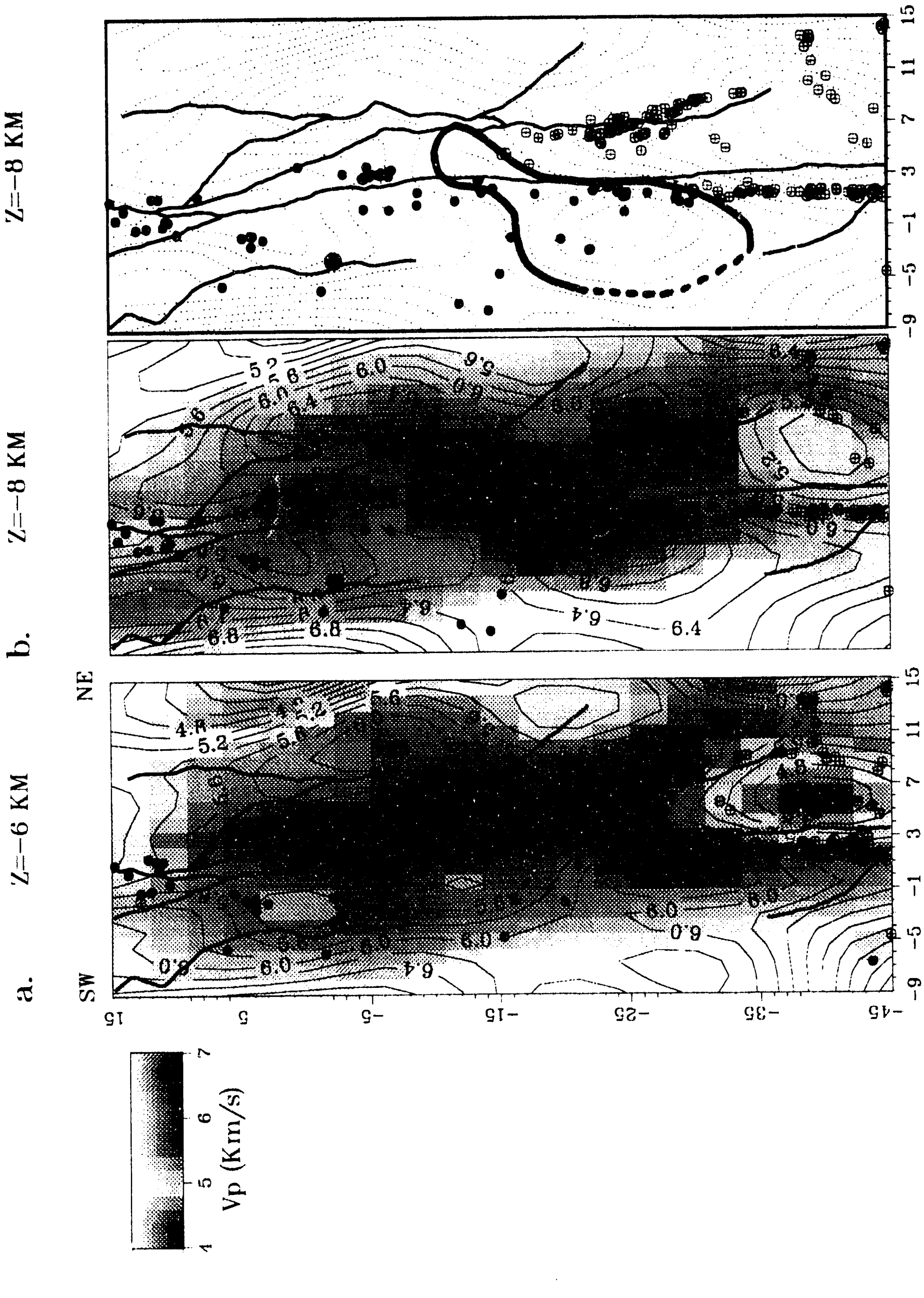
a.
Z=-6 KM
b.
Z=-8 KM
Z=-8 KM
SW
NE
15
5
-5
-15
-25
-35
-45
-9
-5
-1
3
7
11
15
4.8
5.2
5.6
6.0
6.4
6.8
Vp (Km/s)
4
5
6
7

Figure 4.4a,b

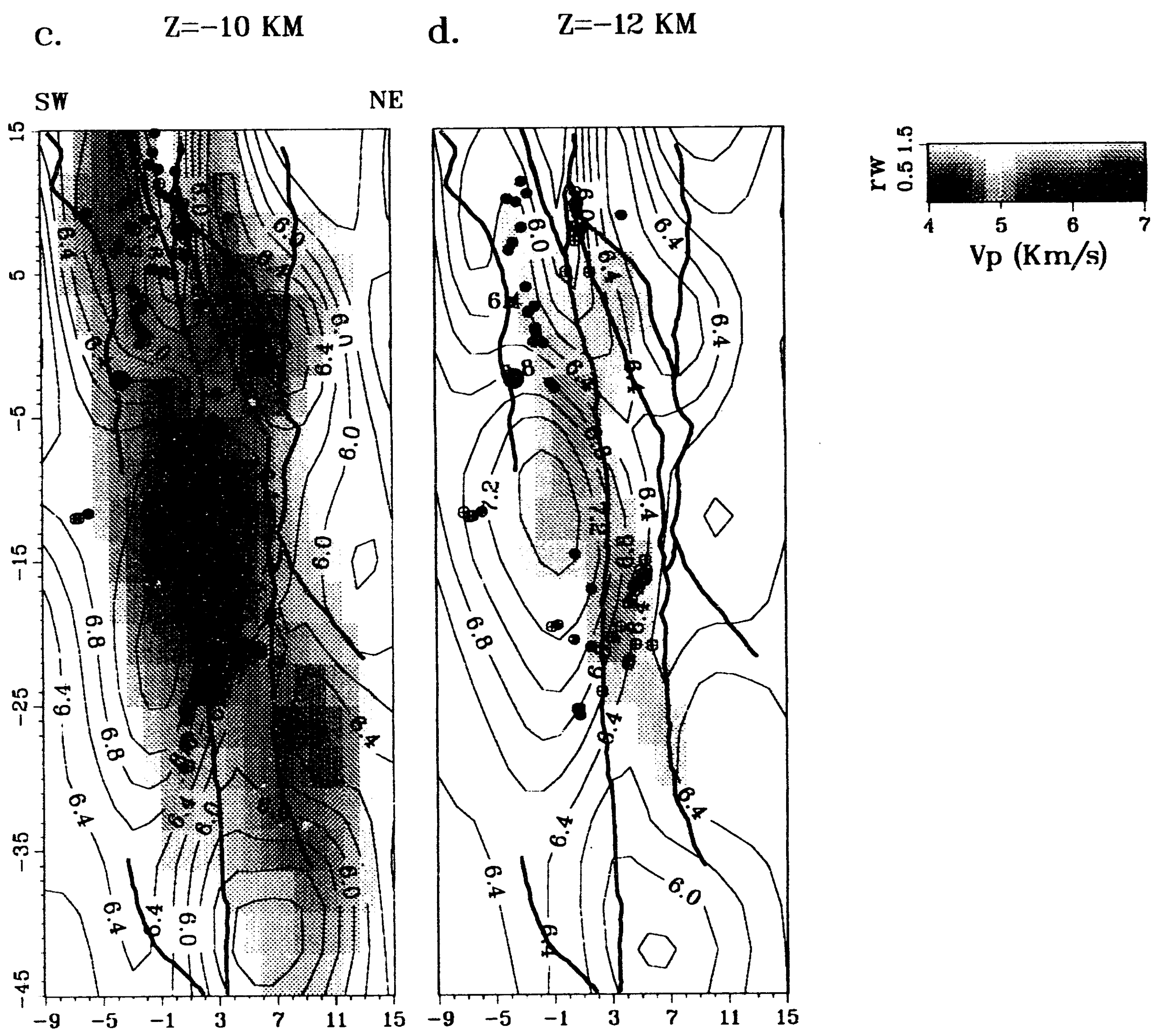
c.
Z=−10 KM
d.
Z=−12 KM
SW
NE
15
5
−5
−15
−25
−35
−45
−9
−5
−1
3
7
11
15
6.0
6.4
6.8
7.2
rw
0.5 1.5
4
5
6
7
Vp (Km/s)

Figure 4.4c,d

Figure 4.5: Across-strike (SW-NE) sections through Loma Prieta 3-D V_p model. Contour interval 0.2 km/s. Bottom panel of each figure shows lithological interpretation. Lithological units: **gm**, Salinian block; **KJf**, Franciscan formation; **Tm**, Tertiary marine sediments; **JT**, Jurassic-Tertiary marine and non-marine sediments; **gb**, gabbro. Arrows indicate major faults (see fig 4.2) and locations of velocity profiles A-E shown in fig 4.7. 1989 mainshock shown as filled red circle in **g**. Aftershocks (filled circles) and background earthquakes (open circles) projected from 1.5 km on either side of section plane.

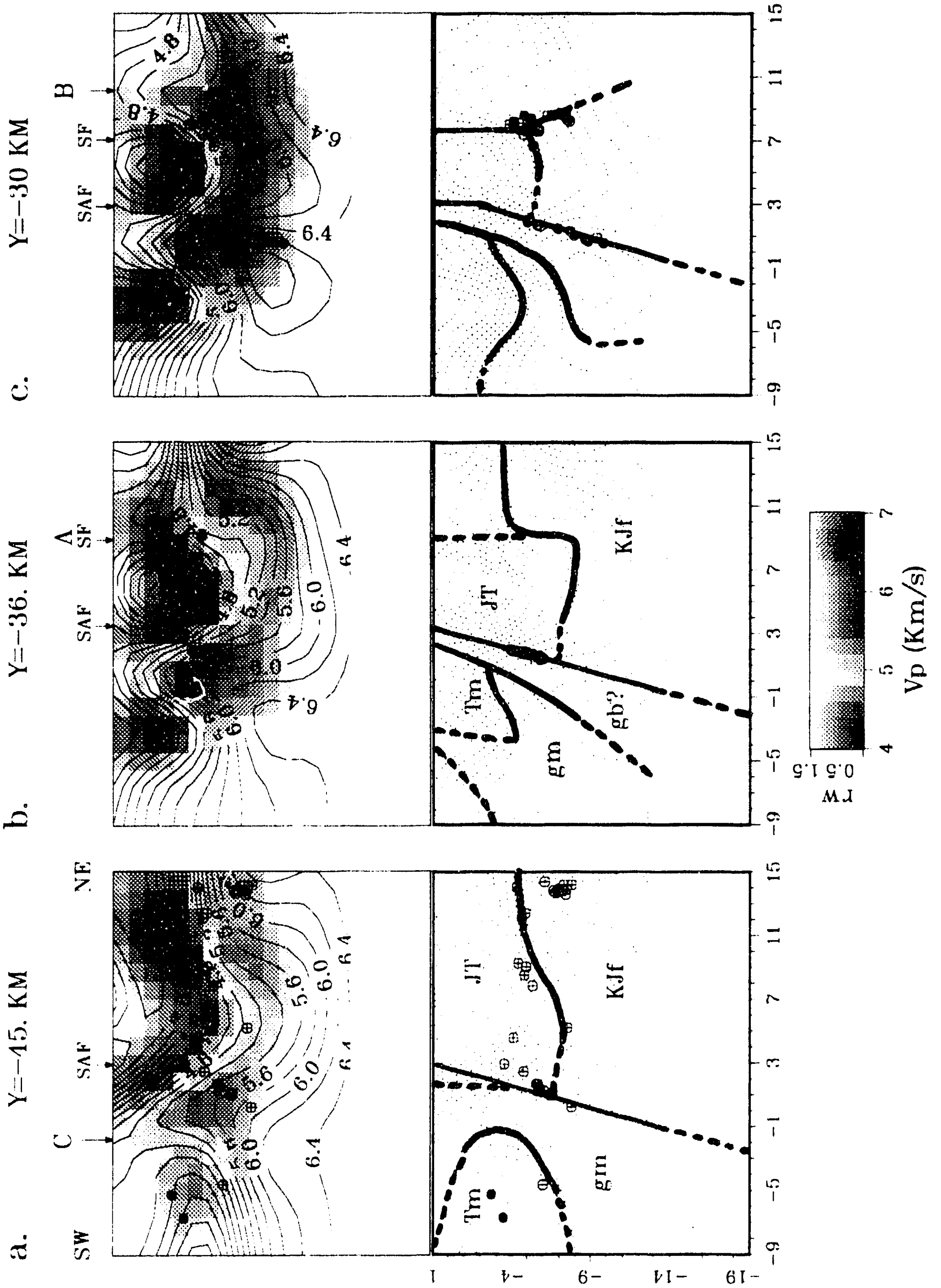

Figure 4.5a,b,c

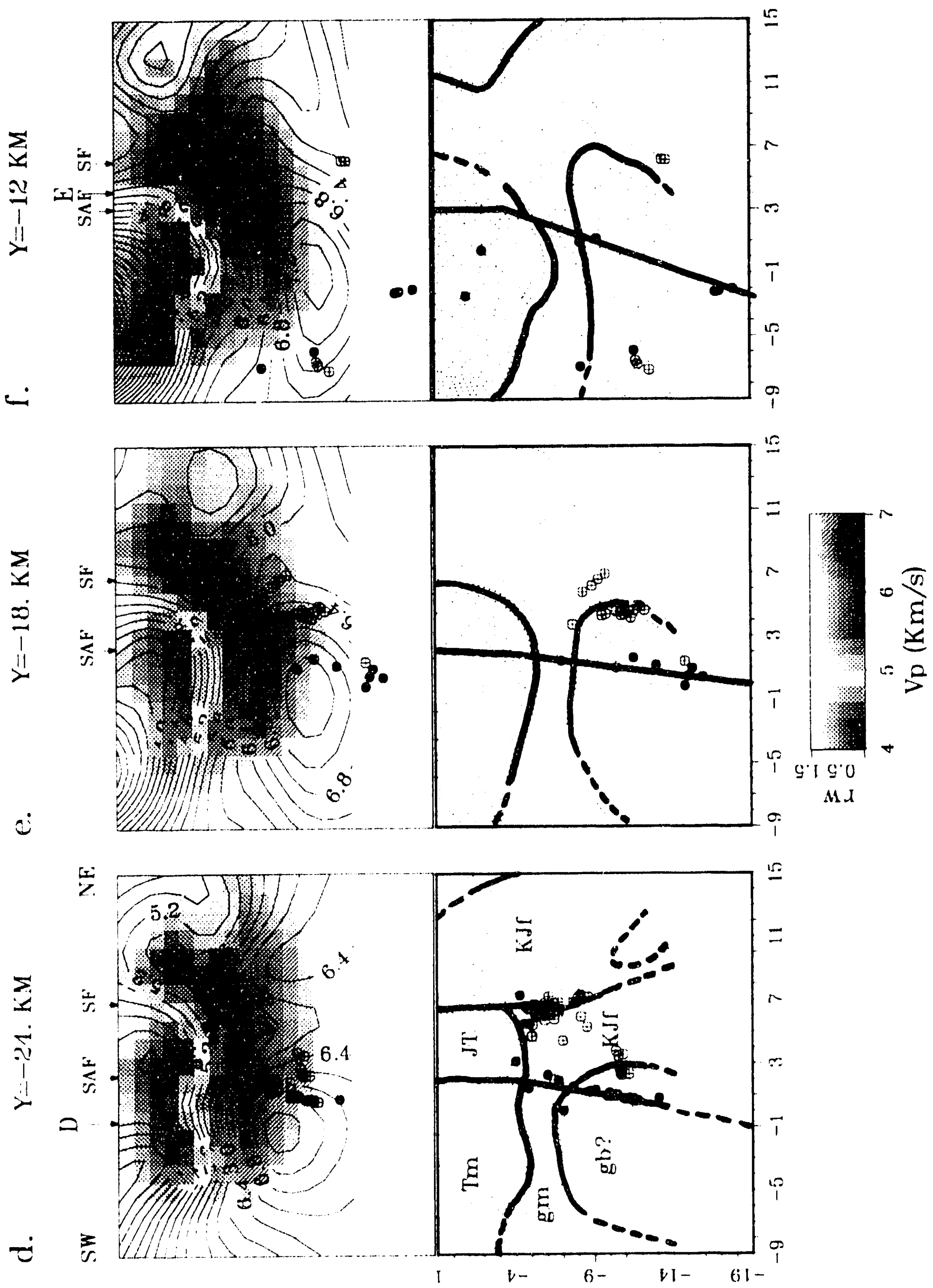

Figure 4.5d,e,f

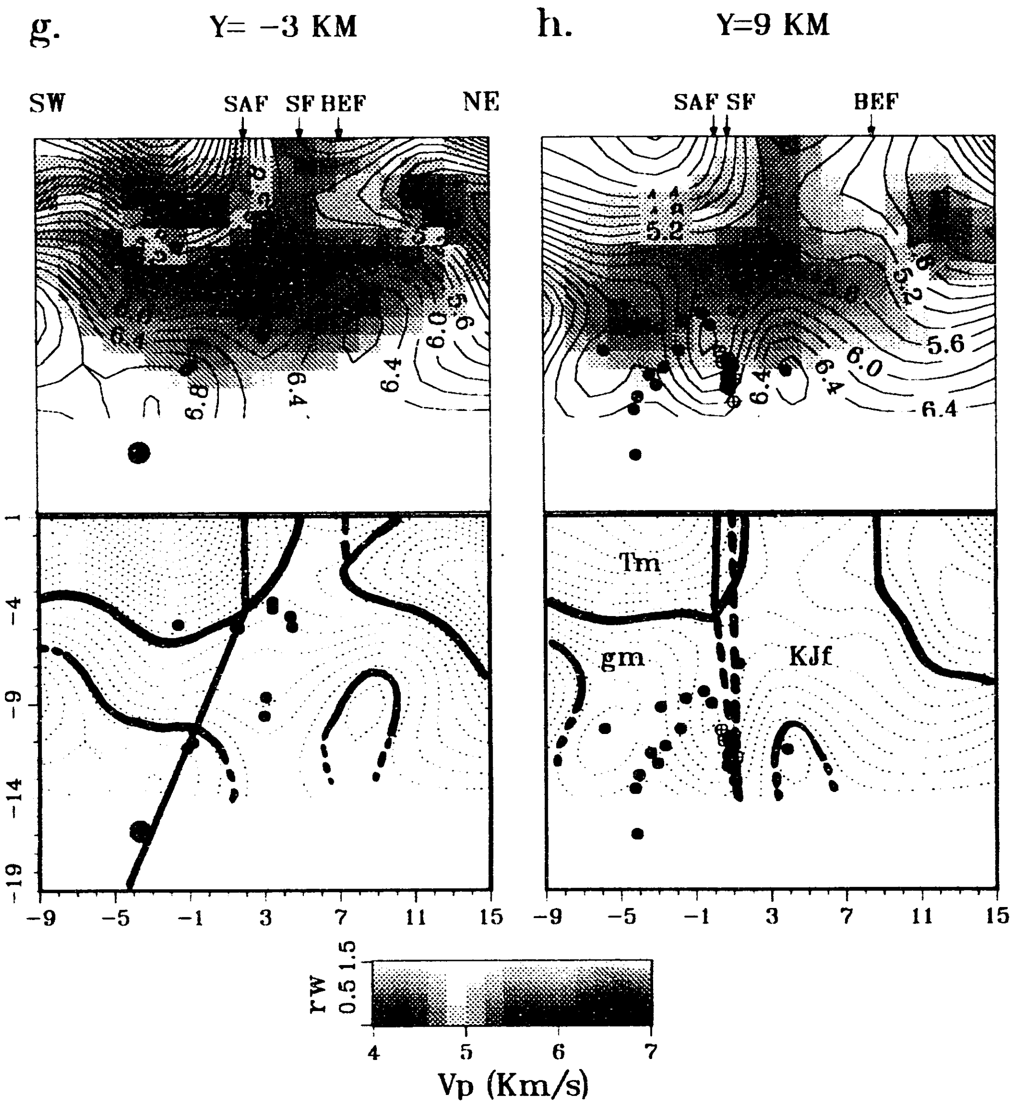
g.
Y= −3 KM
h.
Y=9 KM
SW
SAF
SF
BEF
NE
SAF
SF
BEF
5.2
5.6
6.0
6.4
6.8
Tm
gm
KJf
1
−4
−9
−14
−19
−9
−5
−1
3
7
11
15
rW
0.5 1.5
4
5
6
7
Vp (Km/s)

Figure 4.5g,h

Figure 4.6: Along-strike (SE-NW) sections through Loma Prieta 3-D V_p model. Contour interval 0.2 km/s. Bottom panel of **b.** shows lithological interpretation at x=-0.6 km (see fig 4.5 for explanation). Aftershocks (filled circles) and pre-mainshock earthquakes (open circles) projected from 1.5 km on either side of section plane except in **c**, where they are from x= -3.1 to 1.5 km. Mainshock hypocenter (red circle) projected on to all sections and shown as filled symbol in its appropriate section (x=-3). Arrow in **b.** shows position of Pajaro Gap.

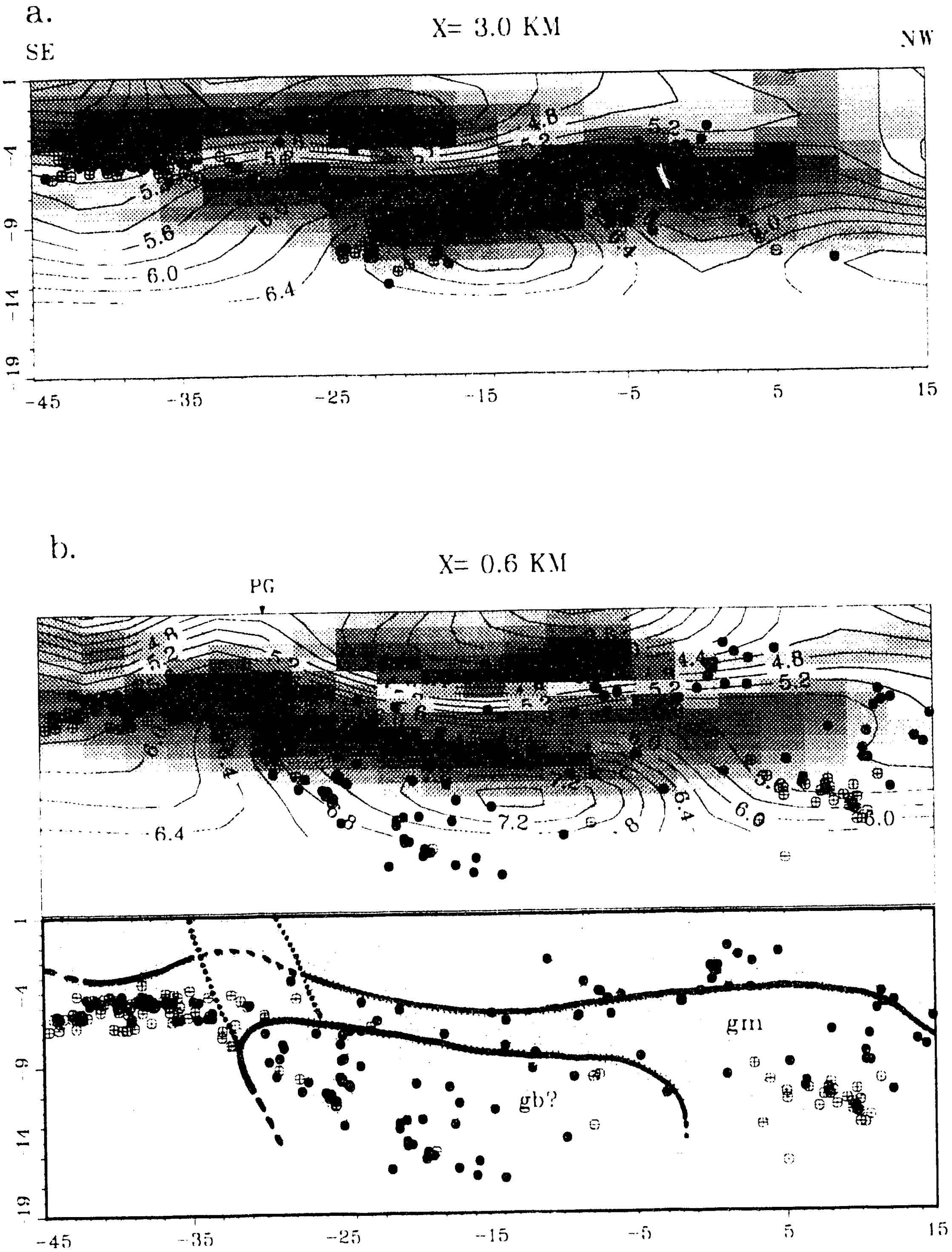
a.
X= 3.0 KM
SE
NW
4.8
5.2
5.6
6.0
6.4
1
-4
-9
-14
-19
-45
-35
-25
-15
-5
5
15
b.
X= 0.6 KM
PG
4.4
4.8
5.2
6.0
6.4
7.2
gm
gb?

Figure 4.6a,b

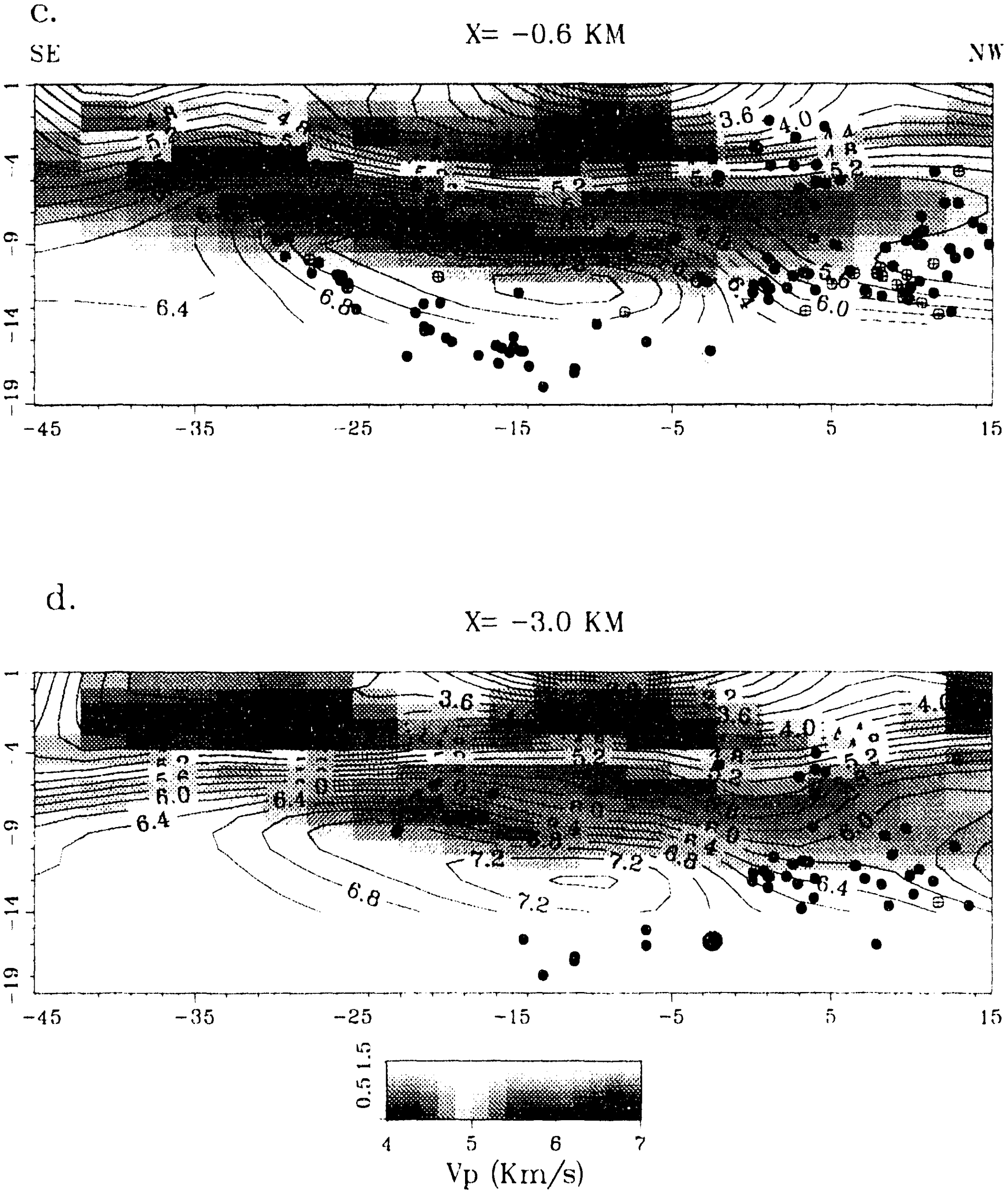
c.
X= −0.6 KM
SE
NW
1
−4
−9
−14
−19
−45
−35
−25
−15
−5
5
15
3.6
4.0
4.8
5.2
6.0
6.4
6.8
d.
X= −3.0 KM
3.6
4.0
5.2
6.0
6.4
6.8
7.2
0.5 1.5
4
5
6
7
Vp (Km/s)

Figure 4.6c,d

sedimentary sequence, except at New Idria and east of Parkfield, where the Franciscan basement is exposed (Page, 1981; Irwin, 1990).

Region II. The narrow velocity low SW of the SAF extending from y= 10 to y= -40 corresponds to the thick section of Tertiary marine sediments underlying the Watsonville Valley (Clark and Rietman, 1973; Irwin, 1990; Fuis and Mooney, 1990) and overlying the Salinian basement, which is composed of Paleozoic(?) metamorphic rocks that have been extensively intruded by granitic plutons of Cretaceous age. The metamorphic rocks are moderate- to high-grade gneiss, granofels and impure quartzite and, within the Loma Prieta model volume, the granite is predominantly quartz monzonite (Ross, 1978).

Region III. The Salinian basement outcrops SW of the SAF as the Gabilan Range at the extreme southeastern edge of the model. This outcrop is bounded to the NW by the Vergeles fault, and it correlates with the relatively high velocities (III) centered on x=0 SE of y= -43. In Figure 4.3, it also appears that the elongated velocity high between y= -25 and y= -40 might correspond to a buried northwesterly extension of the Gabilan Range, but this is probably not the case, as I will discuss later.

Region IV. Finally, the wedge of low-velocity material between the San Andreas and Sargent faults SE of y= -26 corresponds to a very thick section of marine and non-marine sediments having the Great Valley sequence of upper Cretaceous sedimentary and volcanic rocks as its lower constituent This sequence rests on the Coast Range ophiolite, which is in fault contact with the underlying Franciscan rocks at the Coast Range thrust (Bailey et al., 1970; Irwin, 1990). The rocks of the Great Valley sequence are relatively undeformed compared with the Franciscan. The area between the San Andreas and the Sargent faults to the NW of the apex of this low-velocity wedge is a zone of imbricated SW-dipping reverse faults that juxtapose thin fault-sheared slivers of Great Valley sequence, Coast Range ophiolite and Tertiary marine and non-marine sediments (McLaughlin et al., 1988).

The quadrant pattern of alternating high- and low-velocity bodies defines the San Andreas and Sargent faults as near-vertical boundaries coincident with strong lateral velocity gradients. A similar pattern of alternating high and low gravity anomalies separated by steep lateral gradients is seen in the gravity map (fig. 4.3). In general, the shallow velocities in the model are encouragingly correlative with the geology and gravity, providing a reasonable degree of confidence for quantitative analysis of the deeper features in the resolved model.

4.2.2 Interpreting Deeper Features in the Model

Figure 4.7a shows the V_p model and laboratory velocity-depth [$V_p(z)$] profiles for the Franciscan terrane NE of the San Andreas and Sargent faults. The laboratory data include end members of the Franciscan metamorphic suite from the work of Stewart and Peselnick (1977, 1978) and Lin and Wang (1981). Figure 4.7b shows the model and laboratory $V_p(z)$ profiles for the Salinian block. The QM1 profile is for the Gabilan quartz monzonite sample of Lin and Wang (1981), and GR2 and GR3 are granite samples from Birch (1960). Gneiss data shown in both Figures 4.7a and 4.7b are taken from Kern and Richter (1981). Both figures also show profiles for mafic and ultramafic rocks. The gabbro sample of Lin and Wang (1981) is from the Point Sal, California ophiolite, as are the metagabbro and partially-serpentinized peridotite sample (PSP1) of Christensen (1978). Partially-serpentinized peridotite sample PSP3 is from Burro Mountain in the Santa Lucia Range, California (Christensen, 1966a).

The seismic refraction profile of Mooney and Colburn (1985) spans the model from SW to NE at about y= -20. The SW-NE profile of Mooney and Leutgert (1982) covers x= 10 to x= 15 at y= -32. These transverse profiles sample only the uppermost (depth to 3 km) Salinian and Fransican basement velocities in the model volume. The profile of Walter and Mooney (1982) from Big Basin at (x,y) = (-9, 29) along the axis of the Gabilan Range, runs along the southwestern edge of the model, penetrating the entire crustal thickness, but provides only coarse resolution in any particular area. A profile through this model at y= -50km is shown in Figure 4.7b. These three studies are combined into a regional transect through the Santa Cruz Mountains in Fuis and Mooney (1990).

Figure 4.7: Loma Prieta model (bold curves) and experimental $V_p(z)$ profiles for (**a**) Franciscan formation and (**b**) Salinian block. Locations of model profiles A-E shown on Figure 4.5. Ordinate is depth below surface. Sources of experimental data: (1) Lin and Wang (1980); (2) Stewart and Peselnick (1977, 1978); (3) Christensen (1978); (4) Christensen (1966a); (5) Kern and Richter (1981); (6) Birch (1960).

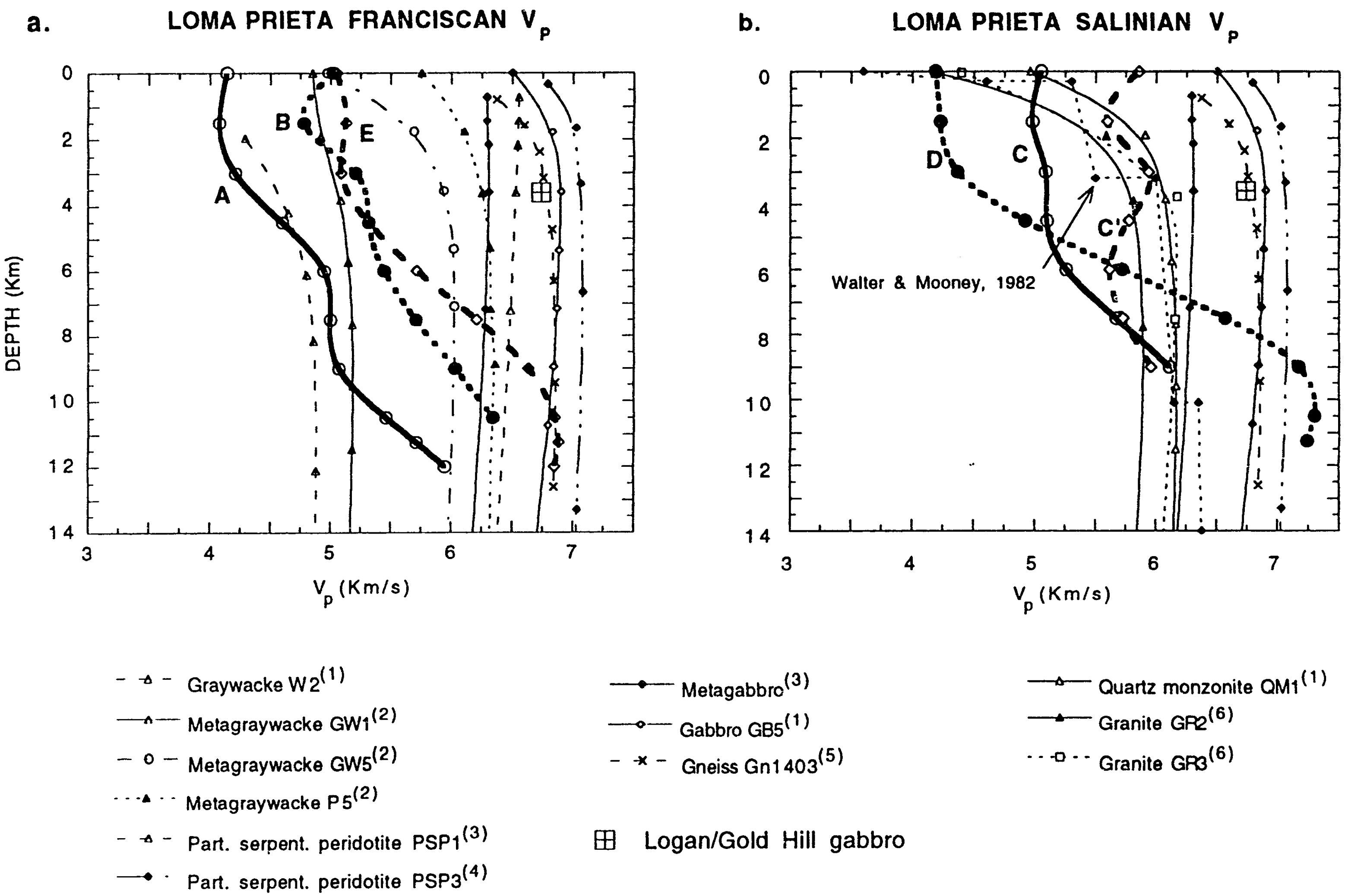
a.
LOMA PRIETA FRANCISCAN V_p
b.
LOMA PRIETA SALINIAN V_p
DEPTH (Km)
0
2
4
6
8
10
12
14
3
4
5
6
7
V_p (Km/s)
A
B
C
C'
D
E
Walter & Mooney, 1982
Graywacke W2(1)
Metagraywacke GW1(2)
Metagraywacke GW5(2)
Metagraywacke P5(2)
Part. serpent. peridotite PSP1(3)
Part. serpent. peridotite PSP3(4)
Metagabbro(3)
Gabbro GB5(1)
Gneiss Gn1403(5)
Logan/Gold Hill gabbro
Quartz monzonite QM1(1)
Granite GR2(6)
Granite GR3(6)

Figure 4.7

The locations of the model $V_p(z)$ profiles, labeled A-E, shown in Figure 4.7 are given on the cross-sections of Figure 4.5.

Profiles A and B. Profile A (y=-36 km) at the Sargent fault reaches the lower bound of Franciscan velocities at a depth around 6 km, and remains within the Franciscan velocity range to the limits of model resolution at about 11 km depth. The very thick section of low-velocity material above the Franciscan at this location is the Great Valley sequence and overlying Cenozoic sediments. This section is thickest here, thinning both vertically and laterally as it pinches out between the San Andreas and Sargent faults to the NW. Profile B at y= -30 km, east of the Sargent fault, is within the Franciscan band of velocities from the surface down to 10 km depth, corresponding to the outcropping Franciscan rocks at that location.

Profile C. Profile C at y= -45 km is through the Gabilan Range SW of the Vergeles fault, and corresponds to granitic basement at the surface. The surface velocity is in fair agreement with the zero-pressure velocity for quartz monzonite QM1, but the model velocities fall significantly below the laboratory values for that sample. This is probably due in part to the lateral smoothness of the model, which broadens the abrupt transition in the upper crust from fast Salinian basement to the very slow Tertiary sediments of the Watsonville Valley at the Vergeles fault. Farther into the Gabilan, SE of y= -50 km, the shallow velocities of Profile C' agree more closely with the QM1 values. However, the modal composition of QM1 (Lin and Wang, 1981, Table 1) is in poor agreement with the composition of the most abundant granitic rock type in the northern Gabilan Range, the quartz monzonite of Fremont Peak, identified by Ross (1972). The QM1 sample has 23% more quartz than the Fremont Peak quartz monzonite (Ross, 1972, Table 6), at the expense of feldspars. Sample GR2 (Birch, 1960, Table 4) is almost identical in composition to Ross' sample, and agrees fairly well with Profile C' at depths below 1-2 km. The GR2 profile is close to the $V_p(z)$ profile through the refraction model of Walter and Mooney (1982) at y= -50 km (fig. 4.7b). The laboratory data do not account for possible macroscopic fracturing and associated low velocities in the Gabilan rocks adjacent to the SAF that may be associated with the intense microseismicity within the depth range 4-8 km, as suggested by Feng and McEvilly (1983). In fact, the C' velocity profile matches very closely in the 1-10 km depth interval the $V_p(z)$ at a location 10 km SW of the SAF in the Gabilan range found by Feng and McEvilly (1983) from a 22 km long seismic reflection profile which crossed the SAF at a location y=-75 km in the Loma Prieta model coordinate system.

The smoothness of the model makes it difficult to resolve the contact between the Salinian basement and the overlying sediments to better than about 2-3 km. The refraction profiles of Mooney and Colburn (1985) and Walter and Mooney (1982) have uppermost Salinian basement velocities in the range 5.3-5.5 km/s. This range corresponds to the steepest vertical velocity gradient in the three-dimensional model on the SW side of the SAF. Therefore, we take the 5.3 km/s contour as the sediment/Salinian contact. With this definition, the velocity cross-sections in Figure 4.5 indicate that the sediments under Watsonville Valley reach a maximum depth of 4-5 km. Mooney and Colburn (1985) show a maximum sediment depth of 2.5-4 km between the Zayante-Vergeles and San Andreas faults.

Profiles D and E. Apart from the major outcropping units described thus far, the most striking feature imaged by the three-dimensional model is the large, SE-NW elongated dome of high velocity rock extending from depth to as shallow as 7-8 km within the southwestern two-thirds of the model (figs. 4.4 and 4.5). The best view of this high-velocity rock mass is in Figure 4.6 on the longitudinal cross-section at x= 0.6 km. A high-velocity body was also imaged in this vicinity by Eberhart-Phillips et al. (1990) and Michael and Eberhart-Phillips (1991). At depths greater than 8 km, the body extends to the NE, cutting across the trace of the SAF. Profiles D, SW of the SAF, and E, to the NE, show that the well-resolved velocities within this body are much too high for both granite and Franciscan rocks. I am confident of the existence of this high-velocity rock mass at depths as shallow as 7-8 km, and the body would still be evident even if these apparently well-resolved high velocities are overestimated by as much as 0.4 km/s (which seems unlikely given the good agreement attained with independently determined velocity data in the rest of the model), although the anomalous rock mass would then be considerably smaller than it presently appears. Furthermore, the discussion of Section 3.2 suggests that the smoothing inherent in the cubic B-spline parameterization tends to smear and lower the velocities at the cores of high-velocity anomalies. I use the 6.4-6.5 km/s contour as the boundary of this rock mass, this velocity being substantially higher than the highest granitic and Franciscan velocities predicted for these depths.

A second, much smaller high-velocity body within the Franciscan to the north, between y= -5 and y= 10, and perhaps a third body to the east are also suggested in Figures 4.4 and 4.5. These may be three separate units, or they may be peaks on the irregular upper surface of a single, large rock mass at depth. Because the model is not well resolved below 12 km I cannot differentiate between the two possibilities. The main (southwestern) mass may also extend beyond the model towards the SW at depths below 9 km and NW of y= -20 km, but the model resolution precludes clear definition.

4.2.3 Other Data on the Extent of the Deep High-Velocity Body

Refraction studies to date have not recognized the high velocity body. The southwestern edge of the well-resolved part of the main body is grazed by the regional profile of Walter and Mooney (1982), who report either a locally faster basement or a rise in the basement elevation near the Santa Cruz Mountains. Mooney and Colburn (1985) observed a wide-angle reflection from a reflection point at a depth of 8.5 km below (x,y) = (9,-20). The velocity under this reflector is estimated to be greater than 6.3 to 6.4 km/s. This depth is in good agreement with the top of the high-velocity body at y= -20 km, and the reflection point is located 2-3 km to the east of the 6.4 km/sec contour.

Zandt (1981) found a relatively large-scale 4% high-velocity anomaly within the upper 10 km of crust in the Southern Santa Cruz mountains area using teleseismic P-wave travel-time tomography. The shape of his anomaly is similar to the one described here, elongated NW-SE and located on the southwestern side of the SAF with the northern end bending eastward to cross the SAF (see his Figure 6). Zandt's anomaly is displaced some 10 km to the SE of the high-velocity body in Figure 4.4, but the resolution of his model in the upper crust is only 10 km.

Zandt's anomaly retains its amplitude and shape into Layer 2 of his model, which extends from 10 to 30 km depth (see his Figure 2). Even though the resolution of Zandt's model in Layer 2 is 20 km, his result does suggest that a large body extends into the middle crust and, probably, the lower crust. Layer 2 encompasses roughly equal thicknesses of lower crust and mantle in this area and contains the 1989 Loma Prieta hypocenter.

One explanation for the presence of a mass of high-velocity rock at shallow and middle crustal depths is that it has been upthrust from below the Salinian and Franciscan basements. Figure 4.7 shows that the velocities within the body approximate those of mafic rocks, moderately serpentinized ultramafic rocks or the highest grades of gneiss. On a regional scale, velocities of 6.8 km/s are observed underlying the Franciscan at depths between 12 and 16 km (Stewart and Peselnick, 1977; Lin and Wang, 1981; Walter and Mooney, 1982; Fuis and Mooney, 1990). These authors have tentatively argued for an oceanic mafic sub-basement under the Franciscan, to which Walter and Mooney (1982) added the possibility of high-grade gneiss or norite.

The preferred Gabilan model of Walter and Mooney (1982) has a 6.35 km/s refractor at a depth of 10 km, which they tentatively identify as a gneissic sub-basement underlying the Salinian block (see also Fuis and Mooney, 1990). Details of their model in the lower crust are not well-constrained but a mafic lower crust having velocities of 6.6 to 6.8 km/s at depths of 16-17 km under the Watsonville Valley is permitted by their data. It seems feasible, therefore, that the high-velocity body is up-thrust sub-basement rock. The presence of a continuous upthrust rock mass beneath both the Salinian and the Franciscan favors a common sub-basement, counter to the preferred interpretation of Walter and Mooney (1982) and Fuis and Mooney (1990). Healy and Peake (1975), however, found evidence for a 6.8 km/s layer at a depth of 10-15 km adjacent to, and on both sides of the SAF in the Bear Valley region, 40 km SE of San Juan Bautista. It is also possible that the upthrusted high-velocity sub-basement consists of an underplated crustal section. The onset at the focus of the reverse faulting in the Loma Prieta earthquake occurred in the lower crust, demonstrating emphatically the presence of major thrusting within the lowermost crust in this region.

Alternatively, the high-velocity rock masses are rootless, drifting along in the mid-crustal fault zone. The apparent depth extent of the anomaly in Zandt's model argues against this model. Or, the main high-velocity body may consist of a relatively small mass on the NE side of the SAF, juxtaposed with a larger block on the SW side by right-lateral displacement along the SAF system.

4.2.4 High-Velocity Body Composition and the Logan Gabbro

The only exposure of basement rocks between the Zayante-Vergeles and San Andreas faults is not Salinian basement but an outcrop 0.5 to 1 km wide of hornblende-quartz and lesser anorthositic gabbro near Logan on the SW side of the SAF, between y= -38 and y= -29 km (see fig. 4.3). This outcrop coincides with the northeastern edge of the narrow velocity high NW of that associated with the Gabilan. The Logan gabbro body was originally identified by Ross (1970) as a fault sliver correlative with slivers of similar composition to the SW at Gold Hill and at Eagle Rest Peak in the San Emigdio Mountains. However, the positive gravity and magnetic anomalies located immediately to the SW of the Logan body led Hanna et al. (1972), Clark and Rietman (1973) and Brabb and Hanna, (1981) to suggest that it is merely a small surface exposure of a large gabbro body that extends to the SW in the subsurface, possibly as far as the Vergeles fault. Hanna et al. (1972) further proposed that a continuation of this gabbro body would be the most likely source of the large, elongated positive magnetic anomaly centered between the Zayante and Butano faults. In fact, Ross (1978, 1984) speculates that, based upon these data, the area between the Zayante and Butano faults is a suture zone of oceanic gabbroic crust that subdivides the Salinian block.

The average composition of the hornblende-quartz gabbro of Logan and Gold Hill given by Ross (1972, Table 12) is 45% plagioclase, 40% hornblende, 11% quartz, and 4% minor minerals (average density 2840

kg/m^3). The quartz content, which ranges from 10% to 20%, makes this a highly unusual composition, which is not matched by any of the gabbro samples for which velocity data are available (including sample GB5 in Figure 4.7). The theoretical velocities for this composition are estimated from the triangle diagrams shown in Figure 4.8. The end members in these diagrams are aggregate velocities at 0.1 Gpa for α quartz (Montana quartzite, Birch, 1960, Table 5), plagioclase and hornblende (Christensen and Salisbury, 1975, fig. 15). The V_p of 6.74 km/s at 3.6 km depth estimated from Figure 4.8a is plotted on the $V_p(z)$ profiles in Figure 4.7, and is probably roughly the same at 7-8 km depth. This estimate is in good agreement with the velocity of the high-velocity body NE of the SAFZ, but low for the highest velocities within the body to the SW.

Following the surface expression of the Logan body to depth in the velocity model (see figs. 4.5 and 4.6), we see an elongated near-vertical slab of relatively high velocities in the uppermost 6 km. The slab is about 3 km wide and is sandwiched between low-velocity sedimentary sections. The model velocities within this slab are much lower than the estimated value for the Logan gabbro; the 3-km x-node spacing of the model cannot resolve such a narrow feature, producing instead a 3-km wide anomaly having velocities that match averages of high gabbro velocity and the low velocities on either side. The Logan velocity anomaly may be an extension of the southeastern "nose" of the deep body, which supports the hypothesis that the deep body may be gabbro, as suggested by Hanna et al. (1972) and Clark and Rietman (1973). However, the NW end of the high-velocity body is approximately coincident with the southeastern extent of the most intense part of the Zayante-Butano magnetic anomaly, so the velocity model does not support the hypothesis that the gabbro extends between the Zayante and Butano faults to north of Ben Lomond Mountain.

4.2.4.1 An Oceanic Basement Southwest of the San Andreas Fault?

The contact between Salinian basement and the overlying sediments is not resolved to better than 2-3 km. The band between the 5.3 and 6.5 km/s contours, which we take as the top of basement and the boundary of the high velocity mass, respectively, is 2-3 km wide even where the top of the high velocity body is most

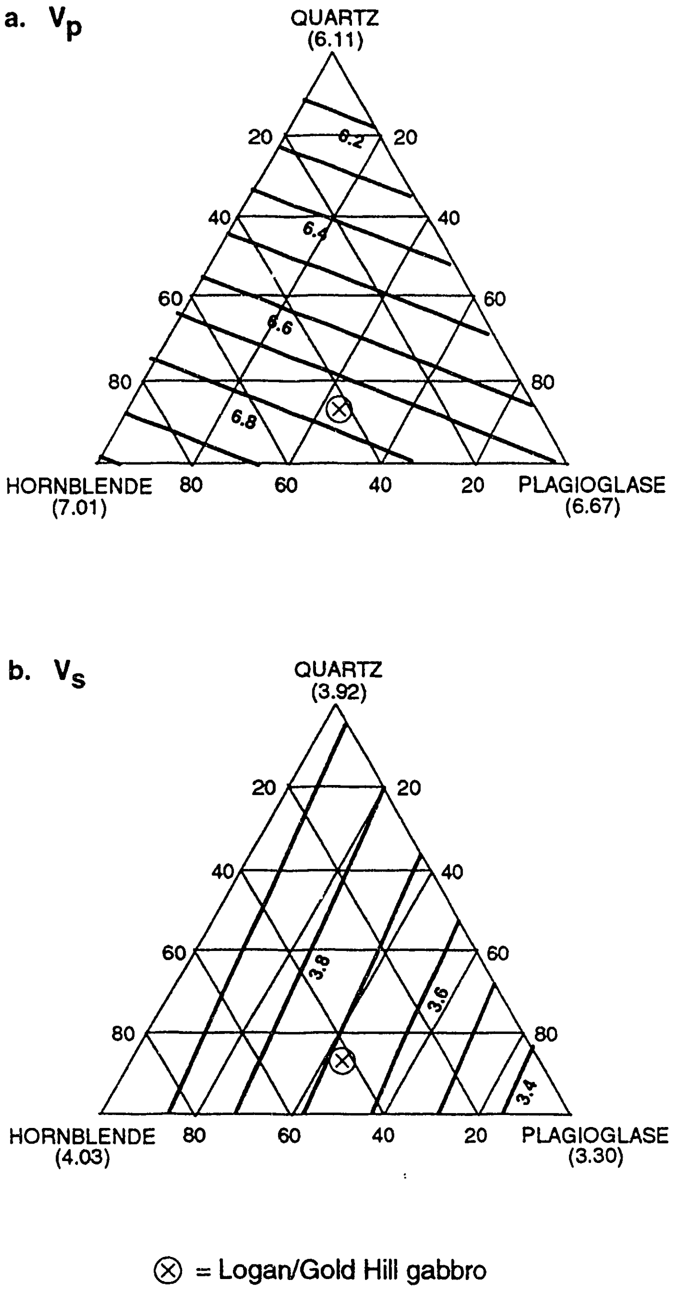

Figure 4.8: Triangle diagrams for (a) V_p and (b) V_s for the Logan/Gold Hill gabbro composition of Ross (1972)

shallow. The speculation of Ross (1984) that the basement between the Zayante and Butano faults is oceanic does not appear to be supported by the velocity model. Rather, there appears to be a slice 2-3 km thick of Salinian basement overlying the high velocity body. This is consistent with the refraction model of Mooney and Colburn (1985), which has an average uppermost basement velocity between the Zayante and San Andreas faults (at y= -20 km) of 5.45 km/s. A similar interpretation also appears to be supported by modeling of the magnetic and gravity data (R. Jachens, U.S. Geological Survey, personal communication, 1992).

4.2.5 Model Summary

The three-dimensional velocity model, along with auxiliary crustal data, suggests a mid- and upper-crustal rock mass having anomalously high velocity underlying both the Salinian and Franciscan basements in the hypocentral zone of the Loma Prieta earthquake. This body is seen through the entire thickness of the crust in a regional tomographic model and its existence, at least SW of the SAF, is also suggested by magnetic and gravity data. The full extent of the body is not constrained by either our model or the regional models. The evidence favors this massive body being an up-thrust section of sub-basement rock. The rather tenuous link between the high-velocity body and the unusual outcrop of gabbro SE of Logan suggests gabbroic composition, in which case it may be similar to the sub-basement underlying the Franciscan assemblage. The velocity model permits a variety of alternative explanations, including intrusive emplacement and crustal underplating, with elevation by repeated earthquakes of the Loma Prieta type near the base of the crust. This massive body appears to play an important role in determining the mode of strain release within the southern Santa Cruz Mountains segment of the SAF zone. Even with only this limited knowledge of the origin and composition of the high-velocity body, I am able to construct a model of how the fault zone behavior is controlled in this segment by along-strike variations in lithology. I continue with a discussion of the relation of earthquake activity to features of the model.

4.3 Relationship of Seismicity to Fault Zone Lithology

In the final transition from the Central Creeping Section of the SAF on the SE to the locked 1906 segment to the NW, the fault creep rate drops from 14 mm/yr at San Juan Bautista to less than 1mm/yr at Pajaro Gap (see fig. 3.1). This drop occurs in an abrupt fashion NW of San Juan Bautista (Burford and Harsh, 1980). The 1989 Loma Prieta mainshock and aftershocks, occupying the southeastern end of the locked segment, reveal details of rupture geometry and processes there. By examining the relationship of these two sets of data to each other and to the fault zone lithology as inferred from the velocity model, we see evidence for a complex process in which major changes in lithology along the fault zone control its slip behavior. I discuss first the background seismicity and closely associated (presumed triggered) activity during the aftershock sequence, and then consider the central aftershock sequence associated with the primary mainshock rupture. The purpose of this section is to demonstrate the connection between earthquake occurrence and structural features of the three-dimensional model.

4.3.1 Background and Aftershock Seismicity

San Juan Bautista to Pajaro Gap. Background seismicity falls off along with surface creep NW of San Juan Bautista. Seismicity associated with the SAF proper stops abruptly at Pajaro Gap (y= -30 km) (fig. 4.2). Hypocenters SE of Pajaro Gap define a single plane striking NW and dipping 70°-75° SW from the SAF trace to about 8 km depth (fig. 4.5). Most of this seismicity is confined to the depth range 3-7 km, which corresponds in the velocity model to the contact at the SAF between Great Valley sequence and Gabilan granite. Earthquakes occur where the sedimentary section NE of the SAF is thick, and activity essentially ceases as the section begins to pinch out at Pajaro Gap. The shallow bound on seismicity corresponds apparently to the contact of Watsonville Valley Tertiary sediments with Great Valley and overlying sediments. NW of y= -38 km, the granite on the SW side of the SAF is replaced by the Logan gabbro at shallow depths, and perhaps throughout the depth range of the shallow seismicity.

Aftershocks that occurred on this section of the fault are within the same depth range as the background activity and are apparently triggered events that are not directly associated with the primary mainshock rupture plane. Fault plane solutions for the background earthquakes and aftershocks are similar, indicating predominantly right-lateral displacement on planes that strike NW-NNW and dip steeply SW (Solution 1, fig. 4.2). An interesting feature of these solutions is a consistent normal dip-slip component of displacement which increases as the strike of the slip plane becomes more northerly.

Pajaro Gap to Hecker Pass. Background microseismicity beneath the Sargent-Berrocal fault zone begins at about y= -31 km, where SAF creep-related seismicity begins to shut down, and forms a linear trend that strikes N60°W to y= -20 km. The plane defined by this trend is near-vertical to a depth of 7 km and dips approximately 70° NE between 7 and 8.5 km. Surface creep observed on this section (y= -30 to -19 km) of the Sargent Fault is about 3 mm/yr (Prescott and Burford, 1976). Although the surface projection of the plane of seismicity falls within about 0.5 km of the Sargent fault trace, the overall trend defined by the earthquakes is about 20° oblique (towards the W-NW) to the local strike of the trace. The fault plane solutions (e.g., Solution 2, fig. 4.2) for these events also indicate predominantly right-lateral displacement on WNW-striking planes. A very minor reverse dip-slip component of displacement, presumed to be on the steep NE-dipping plane, is seen for some of these events. This activity is confined largely to the 4-8 km depth range and occurs within Franciscan rocks between the Great Valley sequence contact above and a rather ill-defined high-velocity body below (fig. 4.5). This shallow seismicity cuts off at Hecker Pass as abruptly as that on the SAF does at Pajaro Gap.

The abrupt cutoff in San Andreas seismicity and surface creep at Pajaro Gap occur exactly where the fault encounters the southeasterly nose of the high-velocity body at a depth of 7-8 km. The cutoff in shallow seismicity under the Sargent-Berrocal system occurs similarly where the trend meets the high-velocity body at about y= -20 km.

Cross-trend Seismicity. Apart from the shallow earthquakes associated with the Sargent-Berrocal system, the only background seismicity that occurs between y= -30 and -15 km is within the depth range 9-13 km between the San Andreas and Sargent fault traces. These events define short, linear cross-trends which closely align with the eastern boundary of the high-velocity body (see figs. 4.4 and 4.5). These deeper earthquakes occur on the contact between the high-velocity rock mass and the Franciscan rocks NE of the SAF. Fault-plane solutions for most of the background events (e.g., Solution 3, fig. 4.2) in the cross-trends are similar to those of the SAF microearthquakes to the SE. Nodal planes do not appear to be rotated systematically northward to line up with the cross-trend hypocenter alignments.

Lake Elsman Seismicity. Background activity has been extremely low in the 20 km stretch of the fault zone north of Hecker Pass that contains the Loma Prieta mainshock and central rupture zone. Background seismicity resumes with the tight cluster of earthquakes near Lake Elsman NW of the high-velocity body. Low-level activity persists on a long-term basis in this vicinity, but the cluster of earthquakes here also includes the M5.0 earthquake of June 27, 1988 and the M5.2 earthquake of August 8, 1989, along with their aftershocks. These sequences define a plane that strikes about N60°W and is near-vertical or steeply NNE dipping between 10 and 14 km depth. This plane lies beneath that defined by Loma Prieta aftershocks in the northwestern section of the rupture zone. The relationship of this plane to the trace of the Sargent fault is not clear. If the Sargent fault is near-vertical to depths as great as 15 km, then the Lake Elsman activity could lie on it. But if the plane of seismicity dips NNE, it may intersect the mainshock plane at about 5 km depth. The depth range of the Lake Elsman background seismicity is the same as that of the cross-trend background activity that occurs to the SE on the contact between the eastern edge of the high-velocity body and Franciscan rocks. The Lake Elsman earthquakes occur within a steep lateral velocity gradient similar to that associated with the cross-trends. This gradient occurs on the southwestern side of a small high-velocity body. Therefore, the Lake Elsman events may be analogous to the cross-trends in that they occur at the contact between Franciscan rocks and high velocity material, although the Lake Elsman events are located 1-2 km SW of the 6.5 km/s boundary contour, so the relationship is tenuous. Fault-plane solutions for the majority of the Lake Elsman earthquakes, including the M5.0 and M5.2 events, are right-lateral and aligned with the seismicity trend, and are similar to the solutions for the shallow events under the Sargent-Berrocal system to the SE.

4.3.2 Primary Aftershock Zone

I distinguish the (primary) aftershock activity on the mainshock fault plane from those (triggered) aftershocks which apparently occurred on other fault surfaces.

Pajaro Gap. Coincident with the abrupt cessation of SAF creep-related seismicity where the fault encounters the high-velocity body at Pajaro Gap there is an equally abrupt increase in aftershock activity upon entering the primary aftershock zone. At this southeastern end of the primary aftershock zone, the aftershocks define a plane (fig. 4.5) within the high-velocity body that is a continuation to the NW and to depths greater than 8 km of the plane defined by the creep-related seismicity and triggered (or secondary) aftershocks to the southeast. This implies that the main active SAF plane begins to cut the high-velocity body at Pajaro Gap. Aftershocks in this region have fault plane solutions (e.g. Solution 5, fig. 4.2) similar to the events to the southeast. At this location the plane of aftershocks is sharply defined and dips 75° to 80° SW, slightly steeper than its dip farther to the SE. For this deep fault plane to be continuous with the SAF trace at the surface it must become near-vertical at about 5-6 km depth. This depth corresponds roughly to the basement/sediment contact, so the fault plane would become vertical after it emerges from the basement into shallow low-velocity sections on both sides of the fault.

Hecker Pass. From y= -23 km northwestward, the sharply defined plane of aftershocks is lost, and the main concentration of aftershocks forms a belt that plunges NW to a maximum depth near 19 km at about y= -13 km, SE of the mainshock hypocenter (fig. 4.6). This belt of aftershocks lies within the high-velocity body, and there are very few aftershocks within the high-velocity body above this plunging belt NW of y= -23. Following Mendoza and Hartzell (1988) and Beroza and Spudich (1988), this gap in the aftershock zone, within the high-velocity body above and SE of the mainshock hypocenter, is presumed to be part of the mainshock rupture plane. Assuming that the high-velocity body extends to the depth of the mainshock focus, the mainshock itself is located close to the body's northwestern end. Note that the mainshock hypocenter shown in Figures 4.1-4.6, computed from first P-arrivals on local and regional seismograms, actually belongs to a small [M=5 (Ellsworth, 1992)] event that preceded the main moment release by about 1.5 seconds (see also Choy and Boatwright, 1990). W. Ellsworth (personal communication, 1992) finds that the hypocenter computed from the main P-arrivals is located close to that of the small event. In longitudinal section (fig. 4.6), the gap in the aftershock zone is seen to continue beyond the top of the high-velocity body between y= -23 and y= -5, indicating that the mainshock rupture extended upwards into the Salinian/Franciscan contact at the SAF. The basement/sediment contact appears to have been the upper boundary of the rupture plane, since the shallow aftershocks tend to concentrate there.

Mainshock Vicinity to Lake Elsman. The full extent of the mainshock rupture plane can be seen in Figures 4.4 and 4.6. The main concentration of aftershocks NW of the mainshock hypocenter occurs between y=0 and 15 km, well to the NW of the end of the high-velocity body and on the Salinian/Franciscan contact at the SAF. The mainshock rupture plane, therefore, extends to the NW beyond the high-velocity body along the Salinian/Franciscan contact. Mirroring the southeastern boundary of the rupture plane, the northwestern aftershocks define a boundary that slopes upward from the edge of the high-velocity body to the basement/sediment contact at 4-5 km depth. In longitudinal section, therefore, the presumed mainshock rupture plane is a rough triangle having its apex close to the mainshock hypocenter. In plan view (fig. 4.4) the rupture plane is confined to the high-velocity body below 10 km but extends progressively NW along the Salinian/Franciscan contact with increasingly shallower depths.

Definition of the precise strike and dip of the mainshock rupture plane itself is uncertain. Based upon the small concentrations of aftershocks that appear to mark its upper and lower boundaries and the few aftershocks that are taken to define the rupture plane itself, the strike of the plane is N50°W-N60°W between y= -15 and 7 km. Its dip SE of y= -8 km is 70°-75° SW. In the immediate vicinity of the mainshock the dip appears to be 65°-70° SW. The aftershock zone between y=0 and Lake Elsman (y=6) defines a relatively steeply dipping (75° SW) zone. NW of Lake Elsman the plane defined by the aftershocks assumes a strike of N35°W-N40°W and the dip shallows to about 60° SW.

4.3.3 Aftershock Mechanisms

Oppenheimer (1990), among others, reported on the wide variety of focal mechanisms observed in the Loma Prieta aftershock sequence. Close study, however, reveals systematic patterns in the different parts of the mainshock rupture surface and on its boundary. In the following discussion, the numbers refer to specific mechanisms shown in Figure 4.2.

Southeastern Zone. Aftershocks below 12 km along the sloping southeastern boundary of the rupture have focal mechanisms (6) that are almost purely right-lateral on WNW-NW–striking planes that dip steeply SW. Nodal planes of the deepest events tend to rotate to the west with an increased reverse dip-slip component (7). At more shallow depths within the high-velocity body the mechanisms are more variable. There dips tend to be steeper, and both some NE-dipping (8) and some nearly north-striking planes are seen. Above the high velocity body mechanisms are largely right-lateral on north-striking planes (9), but there is greater variability than within the deep zone.

Hypocentral Zone. The few aftershocks along the presumed mainshock rupture plane updip from the hypocenter have mechanisms that are distinctly different from those at the rupture boundary. Here, the predominant sense of slip is reverse on steep SW-dipping, NW–striking planes, typified by the immediate M=5 foreshock at the mainshock hypocenter (11). The mechanism for this event is pure thrust, if we use only the up-going raypaths within the model volume to constrain the fault-plane solution (see also Romanowicz and Lyon-Caen, 1990). The minor strike-slip component for most of the aftershocks in this region is right-lateral.

Northwestern Rupture Boundary. A variety of mechanisms is seen on the northwestern boundary of the rupture (y=0 to 7 km). For example, aftershocks in the cluster at (x, y, z) = (-2.5, 2, -12) apparently occurred at the upper surface of the high-velocity body (figs. 4.5d and 4.7d) and involved left-lateral displacement on NW-striking planes (12).

NW of Lake Elsman. The SAF trace bends towards the north near Lake Elsman. In general, aftershock focal mechanisms appear to reflect this change in strike. Mechanisms at all depths are predominantly right-lateral on steep planes that strike within 10° of north. Most of these mechanisms have a significant reverse component (17), and deeper than 6 km there are several pure reverse mechanisms that have nodal planes that strike more northwesterly (16). In contrast to the geometry suggested by these mechanisms, the plane best defined by the aftershock hypocenters strikes N35°W to N40°W and dips 60° SW.

Triggered Background Seismicity. Two main groups of aftershocks apparently are not directly associated with the mainshock rupture plane. The aftershocks in the imbricate zone between the San Andreas and Sargent faults NW of y= -4 km and above 5 km depth seem to be triggered activity. The tight aftershock cluster centered at (x,y) = (3,-6) is similar to activity at the contact between the sloping northwestern end of the high-velocity body and Franciscan rocks.

4.3.4 Seismicity - Lithology Summary

The seismicity provides strong evidence for the prominent role played by the high-velocity body in the transition from stable to unstable fault slip under the Santa Cruz Mountains. The Loma Prieta mainshock clearly broke through the high-velocity body, and the rupture plane defined by the primary aftershocks appears to be continuous at Pajaro Gap with the creeping SAF plane to the southeast. Between Pajaro Gap and Hecker Pass background seismicity closely conforms to the eastern boundary of the body. SE of the hypocenter vicinity the dip of the aftershock plane is about the same as that of the creeping plane and right-lateral focal mechanisms predominate. Four km either side of the mainshock hypocenter the dip shallows by 5°-10°, with reverse-slip mechanisms on SW-dipping planes (including that of the mainshock) predominating. The shallowest dip (60°SW) is seen northwest of Lake Elsman, where there was also significant dip-slip displacement.

4.4 Lithology-Based Fault Slip Model for Loma Prieta

The probable relationship between the high-velocity body beneath the southern Santa Cruz Mountains and the mode of slip along this section of the SAF zone was recognized by Aki (1979) and Zandt (1981). Zandt pointed out that the major faults form the boundaries of his regional-scale crustal velocity anomalies, the single exception being the high-velocity body near San Juan Bautista, which is cut by the fault. I extend this concept by applying the unified model of heterogeneous fault strength and slip stability presented in Chapter 2 to the more detailed three-dimensional structure for Loma Prieta discussed above. This enables me to develop a model for the transition from stable slip to unstable earthquake rupture on the SAFZ under the southern Santa Cruz Mountains, which forms the framework within which I construct a rupture model for the 1989 Loma Prieta earthquake based upon lithological considerations.

4.4.1 SE of Pajaro Gap

Episodic shallow creep and intense microseismicty in the depth range 3 to 8 km on the SAF SE of Pajaro Gap is attributed to the contact between the hard granitic and metamorphic rocks of the Gabilan Range and the abnormally thick section of soft sediments which include the Great Valley sequence. In terms of the unified fault model of Section 2.3, this is a Type 1 fault contact, having low σ_y and always slipping stably. The large contrast in velocity across this contact probably implies a high contrast in hardness and porosity, although, to my knowledge, the relationship of bulk rock hardness to seismic velocity has not been systematically investigated. This apparently high-contrast hard/soft contact certainly appears to fulfill the conditions required for efficient production of fault gouge discussed in Section 2.2.1.1 and so favors stable sliding. Thus, although the resolution of the model is insufficient to image a gouge zone directly, we are able to infer the presence of such a gouge zone from a high contrast in velocity across the fault contact.

This implies that the correlation discussed in Section 1.2.1 between the presence of the Great Valley sequence as one wall of the fault and creep behavior need not rely specifically on the occurrence of serpentinite from the Coast Range ophiolite, but can in part be explained by the hardness contrast between the soft Great Valley rocks and those of the opposite wall of the fault. Obviously this is true only for the upper part of the seismogenic depth range above the Coast Range thrust contact. SE of Pajaro Gap aseismic stable sliding presumably is occurring below 8 km, at the underlying Salinian/Franciscan contact. Since the Salinian/Franciscan contact NW of Lake Elsman is a Type 2 (locked) contact at all depths, additional factors are required to explain the apparent Type 1 behavior of the contact SE of Pajaro Gap. The presence of serpentinite could be a factor in this relatively shallow transition to entirely aseismic slip, in addition to the possible high fluid pore pressures within the Franciscan discussed in Section 1.2.1. Meaningful investigation of the role of porosity and fluids requires both V_p and V_s models and is considered in the discussion of the Parkfield models in Section 5.3.3 below.

4.4.2 Pajaro Gap Barrier

The transition here is from the apparently stable Franciscan/Salinian contact below a depth of 7-8 km to a strong, unstable hard/hard contact as the SAF begins to cut the high-velocity body. In terms of the unified fault model, I hypothesize that the hard/hard contact within the high-velocity body is a Type 3 contact, having high strength, σ_y, and failing only unstably Therefore, this contact can act both as a barrier (high S) and as an asperity (S=0), evolving from barrier to asperity as the tectonic loading, σ_1, builds up. Acting as a barrier, the fault contact within the high-velocity body is locked below depths of 7-8 km. As indicated by the background seismicity and the surface creep data, this locks the fault at shallower depths also. Cessation of surface slip may also be attributable in part to the Great Valley sequence/Gabilan (or gabbro) contact thinning as the Great Valley sequence pinches out, merging into the imbricate zone between the San Andreas and Sargent faults. There are two main responses to this barrier. The first is to load the high-velocity body so that it evolves from barrier to asperity, as predicted by the theoretical model. Failure of this asperity, which occupies the fault zone from Pajaro Gap to Lake Elsman, produced the Loma Prieta earthquake. I defer discussion of the Loma Prieta asperity model to Section 4.5.

4.4.3 Transfer of Slip to Secondary Faults

The second response of the system to the suddenly increased slip resistance on the fault is to attempt to slide around the high-velocity body by transferring slip off the main SAF plane on to secondary structures, apparently by the formation of new faults at contacts having relatively low strength and high frictional stability. Evidence for this behavior can be found in the cross-trends of background earthquakes at the contact between the high-velocity body and Franciscan rocks, where the hard/soft contact permits stable sliding at relatively great depths (9-13 km). In fracture-mechanical terms the high-velocity body represents a hard obstacle encountered by a quasi-statically propagating crack, and the driving force required for crack propagation along the boundary of the obstacle is less than that required to rupture the strong plane within the obstacle. This is a good example of the control of fault zone geometry by lithological heterogeneity, which is further discussed in Chapter 6. Fault plane solutions suggest that this new faulting takes place as a series of *en echelon* fractures that are themselves aligned with the SAF.

The geometry of the main SAF trace is also closely related to the high-velocity body, the presence of the body being expressed by the prominent northeastward bow of the trace between Hecker Pass and Lake Elsman. The right bend at Hecker Pass is adjacent to where shallow stable slip within the fault zone is finally arrested, and the sharp left kink at y= -1 occurs near the point where the fault leaves the northwestern end of the high-velocity body.

Slip is also transferred to the Sargent-Berrocal system adjacent to Pajaro Gap. Although the relationship of the Sargent fault to the present position of the high-velocity body is not as clear as that of the cross trends, there is a spatial correlation, and I propose a similar mechanism for the evolution of this fault. In this model, the splaying of the Sargent fault NW of the high-velocity body and the occurrence of the Lake Elsman earthquakes represent a more mature stage of the "obstacle-avoiding" faulting process suggested by the cross-trends. Why the splaying of the Sargent fault occurs 10 km NW of the high-velocity body rather than along its northwestern boundary is not clear. One possibility is that the position of the splay relates to a previous location of the high-velocity body. Also, the possible association of the Lake Elsman earthquakes with the southwestern boundary of the small high-velocity body mentioned previously may suggest that splay faulting here is occurring, like the cross-trends, along the hard/soft contact between high-velocity material and Franciscan rocks. Following the Sargent fault southeastward from its intersection with the SAF, the fault strikes sub-parallel to the small high-velocity body to just beyond the southeastern end of this body at y= -5, where the fault bends to the right to follow closely the northeastern boundary of the main high-velocity body. In my model, the splay-fault system is growing along favorably situated hard/soft contacts to circumvent the high-strength obstacle.

My model for this large-scale process is based upon the apparent relation of the Sargent fault trace and the Lake Elsman earthquakes to the deep high-velocity body. Southeast of the high-velocity body, where Sargent-Berrocal seismicity defines a plane at shallow depths, that plane apparently is located within Franciscan rocks on the trend of a sharp lateral gradient in the velocity model, but not at a lithologic interface. Between y= -16 and -10 km the Sargent fault is mapped slightly NE of the high-velocity body, but, as it is mapped as SW-dipping, it may cut the body at depth, consistent with the cessation of shallow activity at Hecker Pass.

4.5 Loma Prieta Asperity Model

The 1906 earthquake rupture extended SE about to San Juan Bautista. Aki (1979) pointed out, based upon evidence presented by Thatcher (1979), that the rupture does not appear to have extended appreciably into the creeping section, and was not, therefore, arrested by sudden reduction of the tectonic loading (σ_1) available to drive the rupture. Rather, Aki suggests that the 1906 rupture was arrested by Zandt's (1981) high-velocity body, which acted as a fracture energy barrier with sufficiently high strength (σ_y) to resist the dynamic loading of the propagating rupture (i.e. S in Equation [2.14] remains above zero). If this is correct, then the high-strength fault contact within the high-velocity body not only concentrates stress from steady-state tectonic loading but also was dynamically loaded by the 1906 rupture. Furthermore, the high stress across this contact will not be uniformly distributed, but the NW end of the contact will be more highly loaded than the SE. Having acted as a barrier to the 1906 rupture, the highly stressed contact within the high-velocity body evolved to an asperity as σ_1 continued to increase under steady-state tectonic loading, and S became zero in 1989. While the 1906 rupture was largely arrested by the barrier below 7-8 km depth, a much depleted residual rupture continued along the "normal" SAF Salinian/Franciscan contact above the barrier as far as San Juan Bautista. This explains the interpretation of Segall and Lisowski (1990) that the rupture there was confined to shallow depths. It also provides a reason for the abrupt decrease in coseismic fault slip in the 1906 earthquake along the stretch of the SAF located at y=20 to 40 km in the model coordinates (Thatcher, 1975; Boore, 1977).

The resulting asperity model for the Loma Prieta segment of the SAF is shown in Figure 4.9. The elliptical asperity is an idealization of the shape of the high-velocity body in Figure 4.6. The SE creeping section of the SAF approximates the low stress (σ_1), low strength (σ_y), freely slipping fault plane surrounding the classical asperity of Rudnicki and Kanamori (1981). The Salinian/Franciscan contact at the SAF above and NW of the asperity in the Peninsular and Santa Cruz Mountains section of the 1906 rupture plane is a Type 2, conditionally stable contact that has a strength much higher than that of the creeping segment but significantly lower than that of the Type 3 contact within the high-velocity body. The microseismicity of the Peninsular section is appreciably higher than that along the 1906 break to the NW of the Golden Gate, which suggests that the Peninsular section may be sliding at a very low rate. Dynamic loading of the Peninsular section can come from either a SE- (1906) or, as we suggest next, a NW-propagating rupture.

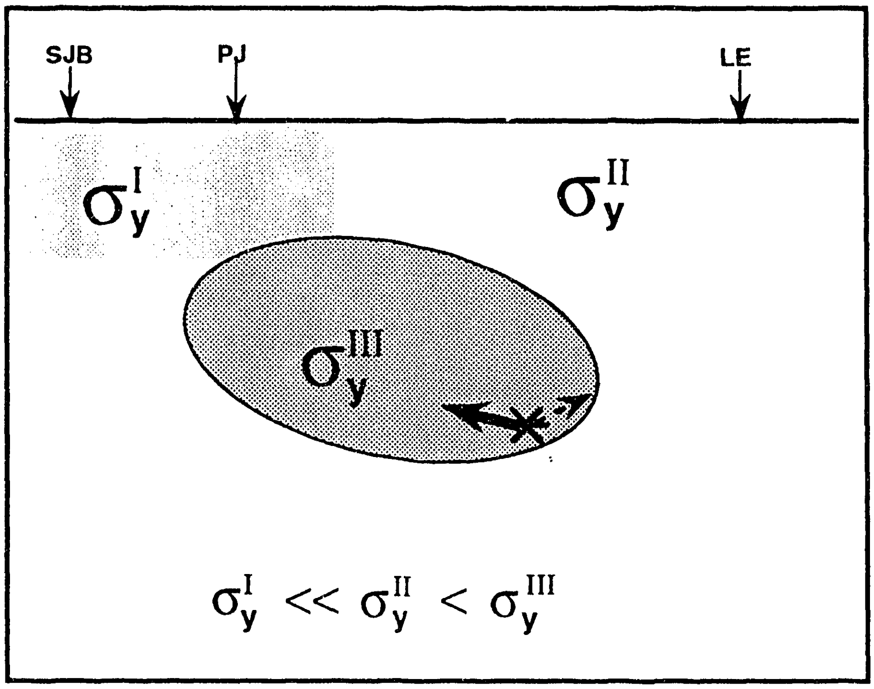

Figure 4.9: Cartoon of Loma Prieta asperity model. Regions I, II and III represent Central Creeping Section of SAF, 1906 rupture surface and Loma Prieta asperity, respectively. 1989 hypocenter shown by cross and directions of rupture propagation by arrows. **SJB**, **PJ** and **LE** are positions of San Juan Bautista, Pajaro Gap and Lake Elsman, respectively.

Dynamic rupture of an elliptical asperity on an infinite fault plane has been studied theoretically by Das and Kostrov (1985). In their model, the locked asperity is loaded quasi-statically by allowing the surrounding low-strength fault plane to slip stably in response to a fixed displacement applied at "infinity". The resulting stress field within the asperity has maximum stress concentrations at the ends of the major axis of the ellipse. Since the fracture criterion at any point is that the loading stress (σ_l) equal the (uniform) fracture strength (σ_y) of the asperity, the asperity will always fail (S=0) first at one or both of the ends of the major axis. Furthermore, dynamic rupture of the asperity would nucleate *only* by fracture in the vicinity of one of the ends of the major axis. The asymmetric loading of the Loma Prieta asperity and the point of rupture initiation certainly satisfy this requirement. The M=5 foreshock and, apparently, the mainshock hypocenter are located within the dynamically-stressed northwestern end of the asperity (fig. 4.6). The aftershock distribution shows that the mainshock nucleated at the down-dip end of the rupture plane, which extended along the entire length of the high-velocity body except at its southeastern edge, where the plunging belt of aftershocks indicates the rupture boundary. Das and Kostrov's result for an elliptical asperity oriented with respect to the fault displacement as at Loma Prieta has the rupture propagating linearly from one end to the other, the displacement being in-plane, or strike-slip. Given that the mainshock nucleated at the northwestern end of the Loma Prieta asperity (i.e. the high-velocity body), the asperity itself ruptured primarily from northwest to southeast, and the predominance of right-lateral displacement in focal mechanisms southeast of the mainshock hypocenter is consistent with the asperity model.

In this model the NW-SE asymmetry in the stress field across the asperity resulting from dynamic loading in 1906 left the southeastern end of the Loma Prieta asperity well below its fracture strength. This end of the asperity acted as a low-driving-stress barrier which arrested the 1989 rupture. The resulting stress concentration was responsible for the dense clustering of aftershocks there. The lack of aftershocks within the mainshock rupture indicates that few barriers on the fault plane remained unbroken, consistent with a high pre-stress across the asperity.

The other main departure from the simple asperity model is replacement of the stable fault plane around the northwestern end of the asperity with a Type 2 conditionally stable plane. Dynamic rupture behavior across a Type 1-Type 2 transition has not been studied. Okubo (1989) studied the rupture of a simple one-dimensional asperity model with a rate- and state-dependent friction law, showing that asperity rupture can overshoot onto the stably-sliding plane and produce a transient high peak σ_1 there. I suggest that normal tectonic loading on the relatively strong fault plane NW of the 1989 Loma Prieta asperity had reached a significant level since 1906, and that failure of this part of the fault during the mainshock was unstable rupture triggered by dynamic loading from overshoot of the asperity rupture.

In my model the Loma Prieta rupture consists of two parts, rupture of the Type 1 asperity and of the Type 2 plane to the NW. Kinematic models of the rupture history, such as that of Beroza (1991), show that this is indeed the case. These models have three distinct sub-events - a small nucleation event at the mainshock hypocenter, then moment release on two patches, SE and NW of the hypocenter. Beroza's (1991) model is parameterized in terms of the strike-slip and dip-slip components of displacement. The largest sub-event in his model is centered (after correcting for small differences in hypocenter location) at about (x,y,z) = (-2, -10, 12.5) in our model, at the "core" of the high-velocity body. Displacement (5.9m maximum) of this sub-event is predominantly strike-slip, consistent with rupture of the asperity. The smaller northwestern sub-event is centered at about (x,y,z) = (-1.5, 3.5, 10.5), just above the northwestern end of the high-velocity body, and is predominantly dip-slip (maximum slip 4.5m). It is not clear why dip-slip displacement should predominate NW of the hypocenter, although this may be related to possible warping of the fault plane in and near the northwestern end of the high-velocity body. Viewed as a fracture system the broad fault zone (ZF, BuF, SAF, SF in fig. 4.3) NW of the mainshock becomes a restraining bend, and, as such, the locus for the N-S compressional accommodation represented in the predominant reverse faulting seen there. Furthermore, estimated locations for aftershocks during the first 10 minutes of the sequence (Simila et al., 1990) in this NW region (y=10 to 20 km) suggest a distinct, SW-dipping fault surface offset a few km to the SW from the plane of the later aftershocks, perhaps indicative of a different mode of deformation in the NW part of the failure zone. The actual localization of high slip at this sub-event is probably controlled by interaction of the dynamic stress peak as the rupture emerges from the end of the asperity with the quasi-static stress field, which, judging by the great variety in focal mechanisms there, is complex. Beroza's kinematic model is generally consistent with my asperity model.

4.5.1 Implication of the Asperity Model for Earthquake Recurrence

If the asperity model is correct, then the Loma Prieta earthquake is a distinctly different type of event from the 1906 earthquake. The only parts of the SAF that were ruptured by both events are the Salinian/Franciscan contact NW of the 1989 hypocenter (see fig. 4.6) and the narrow continuation of this contact at shallow depths above the high-velocity body. Even though my model requires that the 1906 and 1989 earthquakes both ruptured the SAF in the southern Santa Cruz Mountains, I concur with Beroza (1991) that the 1989 Loma Prieta earthquake did not involve a repeat of 1906 slip. The potential for future earthquakes in this region remains unclear. The potential of the 20-25 km-long segment of the Sargent fault between Hecker Pass and Lake Elsman for producing earthquakes in the range M6-6.5 has not been addressed. This fault segment may show evidence for recent displacement (McLaughlin, 1974) but it remained aseismic during the Loma Prieta aftershock sequence. Like the Loma Prieta mainshock rupture plane, the Sargent fault plane may cut the high-velocity body at depth immediately NW of Hecker Pass.

CHAPTER 5

PARKFIELD

5.1 Joint Inversion

The joint inversion for the Parkfield V_p and V_s models is described by Michelini (1991), and used three data sets. The first data set consists of 396 P travel times from 36 earthquakes recorded at 10 or more USGS CALNET stations in the Parkfield area. These data have an estimated timing precision of ±20 ms , and were included to constrain the gross features of the V_p model. The second set consists of 1380 P and 435 S travel times from 133 selected earthquakes recorded by the ten-station three-component, downhole High Resolution Seismic Network (HRSN) deployed in the Parkfield area, which is described in Karageorgi et al. (1992). The selected earthquakes each have at least 8 clearly recorded P or S phase readings. Timing precision of the P times recorded by the HRSN is ±2 ms. Only reliably identifiable S arrivals were used, which have an estimated reading precision of about ±4-8 ms. Finally 35 P and 25 S travel times recorded by the HRSN as part of the routine travel-time monitoring experiment at Parkfield (Karageorgi et al., 1991) were used to provide near-surface velocity control. The starting one-dimensional model was computed using a linear inversion, and yielded a weighted RMS residual of 0.141 s.

The velocity model is parameterized on a the 9x6x5 (X,Y,Z), 270-node grid shown in Figure 5.1. Node spacings are 1.2, 5, and 2.5 km in X, Y, Z, respectively. As at Loma Prieta, the XY coordinate system is rotated 45° counterclockwise to align with the surface trace of the SAF. The origin of this coordinate system is at the reported epicenter of the 1966 Parkfield earthquake, 53° 57.3' N, 120° 29.9' W (McEvilly et al., 1967). Figure 5.1 also shows the earthquakes and stations used in the inversion. The final velocity models yield a weighted RMS residual of 0.025 s after 9 iterations.

The model volume extends from 15 km SE of the 1966 epicenter to 10 km NW, and includes the nucleation zone of the Parkfield earthquakes and the rupture zone to the SE as far as 4 km NW of Gold Hill. 1279

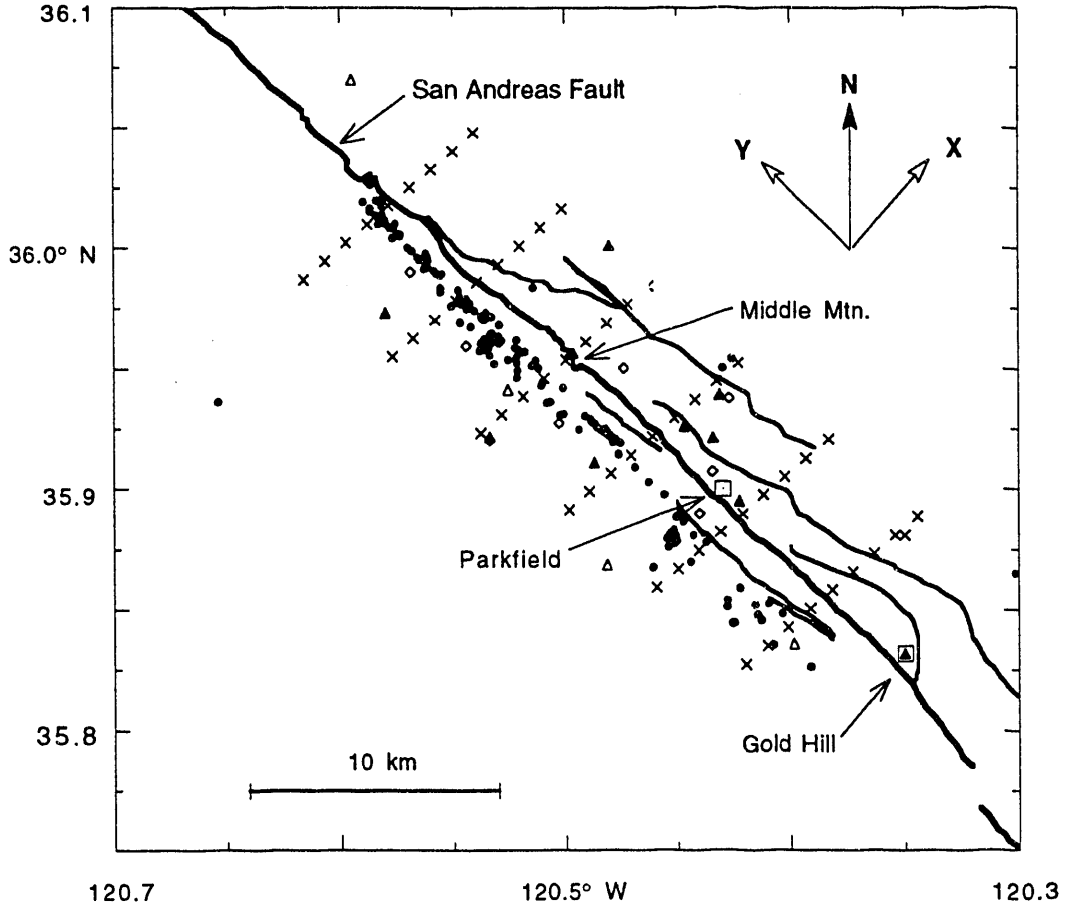

Figure 5.1: Map of Parkfield area showing horizontal distribution of node points (crosses), earthquakes (dots), HRSN stations (filled triangles), CALNET stations (open triangles), and vibrator points (diamonds) used in the Parkfield simultaneous inversion. Major faults shown as bold lines, see fig. 5.2 for fault identification. Inversion grid extends from (x,y) = (-5, -15 km) at lower left corner to (4.6, 10 km) at upper right. Based upon Michelini, 1991, fig. 4.1.

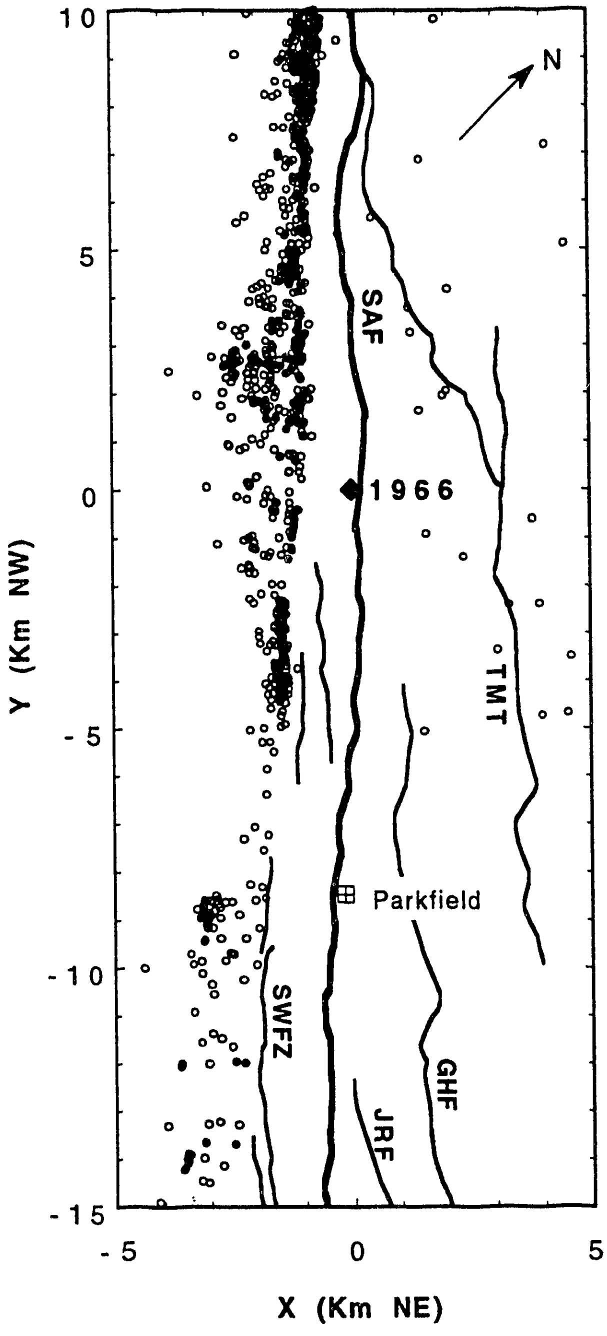

Figure 5.2: Map of Parkfield study are showing 1966 mainshock epicenter (diamond) and clustered (filled circles) and other (open circles) background seismicity. Major faults: **GHF**, Gold Hill; **JRF**, Jack Ranch; **SAF**, San Andreas; **SWFZ**, Southwest Fracture Zone; **TMT**, Table Mountain thrust.

earthquakes that occurred within the model volume between February, 1987 and December, 1991 recorded by the HRSN were located with the three-dimensional V_p and V_s models The smallest events have an estimated M_L of about -0.5. These earthquakes are plotted on Figure 5.2, which also shows the surface traces of the major faults in the Parkfield area. The rotated X-Y (NE-NW) coordinate system of Figure 5.2 will be used in all subsequent figures.

5.2 The Parkfield V_p Model

I begin by interpreting the better-resolved V_p model and then refine and add to the interpretation using the V_p/V_s model. The map view of the V_p model at a depth of 1.8 km (z=-0.8 km) is shown In Figure 5.3 for comparison with the geology, isostatic gravity and aeromagnetic maps that are also shown in this figure. Map views at deeper horizons are shown in Figure 5.4. Figures 5.5 and 5.6 are across-strike (SW-NE) and along-strike (SE-NW) depth sections through the model at specified values of Y and X, respectively. Display of the velocity and spread function is the same as described in Section 4.2. Background seismicity (circles) and aftershocks of the 1966 earthquake (crosses) are projected on to the planes of section as described in the individual figure captions. The subset of aftershocks plotted in these figures are discussed in Section 5.5.1. The creep rate plot shown on Figure 5.6b is based upon data from Burford and Harsh (1980) and Lienkaemper and Prescott (1989).

I begin by summarizing the geology of the SAFZ in the Parkfield area.

5.2.1 Summary of Geology

The descriptions of the Salinian and Franciscan basement rocks on either side of the SAFZ at Loma Prieta (Section 4.2.1) apply equally well to the Parkfield area. The only basement outcrops within the Parkfield model area are Franciscan rocks and serpentinite along its NE margin from y=-7 northwestwards (fig. 5.3). Dickinson (1966) describes the fault zone within 5 km of the SAF in this area as a complex domain of

Figure 5.3: (**a**) Surface geology within the Parkfield study area; (**b**) Map view of Parkfield V_P model at 0.8 km depth (below msl); (**c**) isostatic gravity map, contour interval 2 mGal; and (**d**) aeromagnetic map, contour interval 20 nT. Main geologic units are **blue** (f), Franciscan complex, **purple**, serpentinite. See fig. 5.2 for fault identification. Geology, gravity and aeromagnetic maps from Wentworth et al. (1992), courtesy of Carl Wentworth, U.S. Geological Survey.

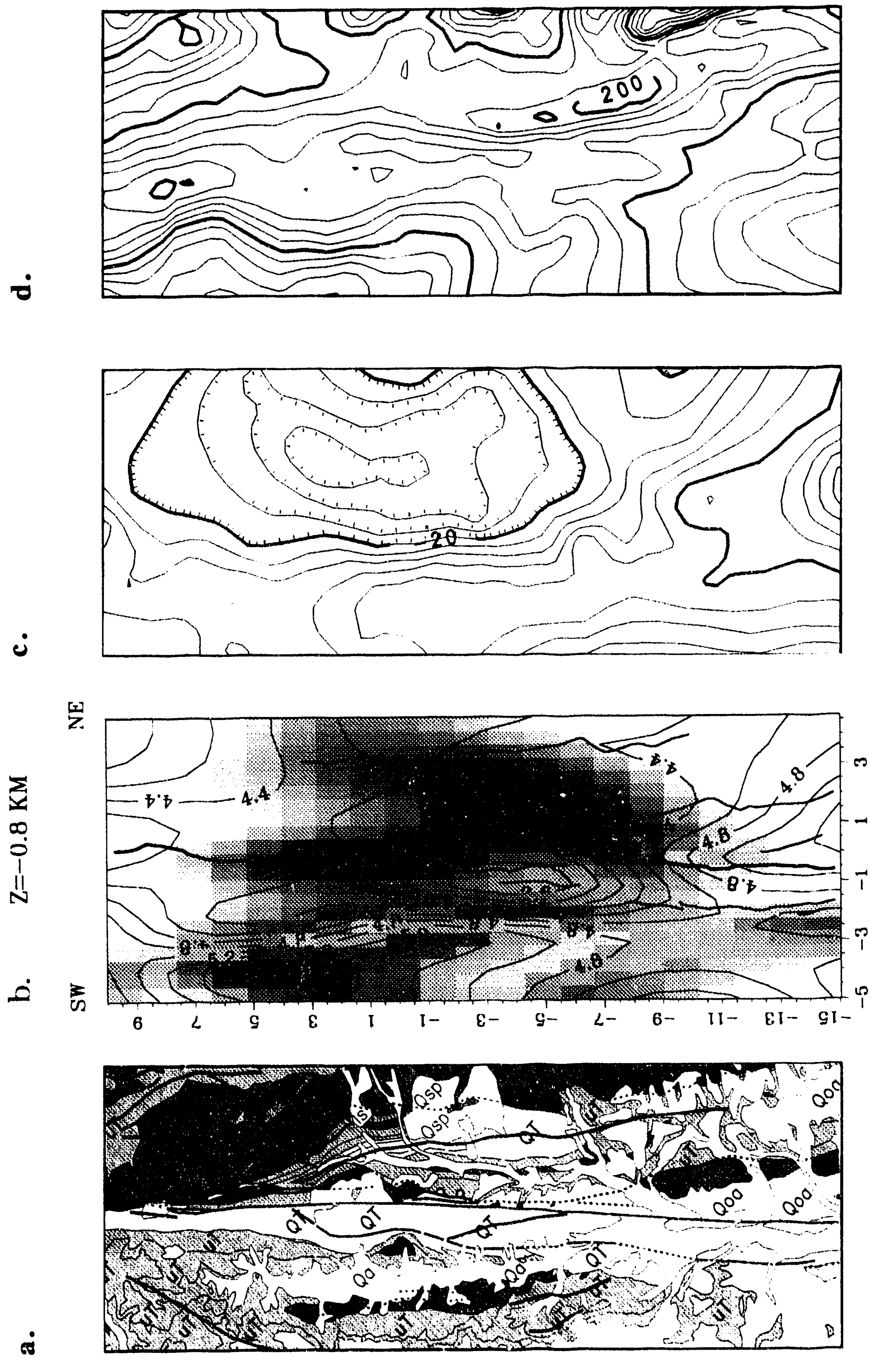
a.
b.
Z=-0.8 KM
c.
d.
SW
NE
9
7
5
3
1
-1
-3
-5
-7
-9
-11
-13
-15
-5
-3
-1
1
3
4.4
4.8
20
200
QT
Qsp
Qoa
Qa
uT

Figure 5.3

Figure 5.4: Map views of Parkfield 3-D V_p model at depths (below msl) of: (**a**) 3.2 km; (**b**) 4.4 km; (**c**) 5.6 km; (**d**) 6.8 km; (**e**) 8.6 km. Contour interval 0.2 km/s. Interpretative panel in **d.** outlines deep anomalous high-velocity body and positive V_p/V_s anomaly from fig 5.11d (shown in red). See fig 5.2 for fault identification and seismicity symbols. Filled red circle is 1966 mainshock epicenter. Hypocenters projected from depth intervals 1.2 km on either side of section plane.

AIIM

Association for Information and Image Management

1100 Wayne Avenue, Suite 1100
Silver Spring, Maryland 20910

301/587-8202

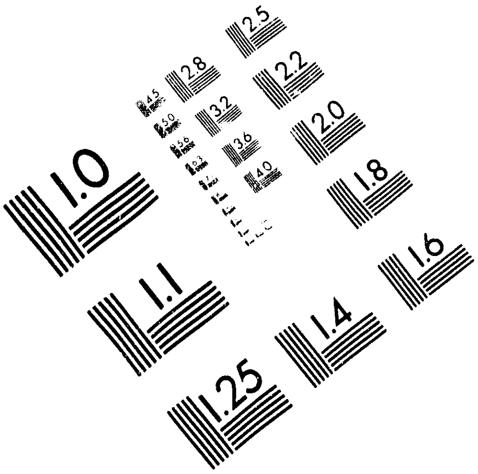

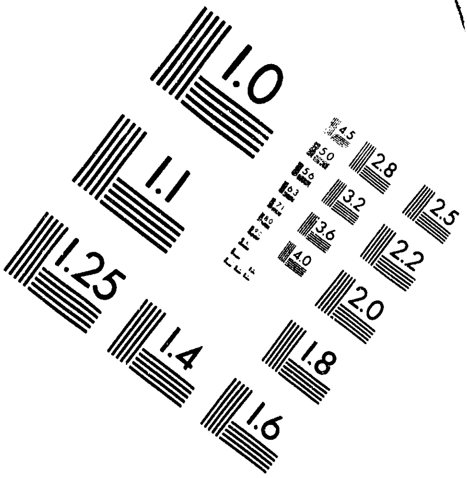

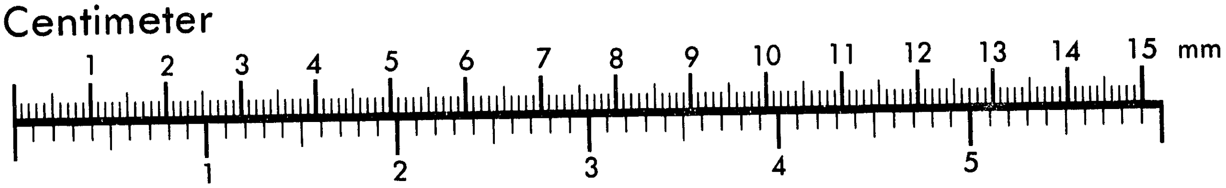

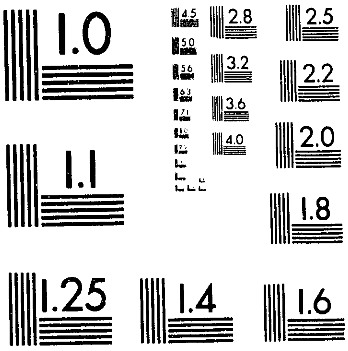

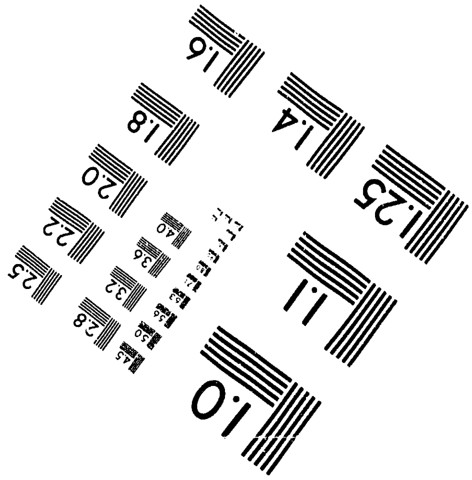

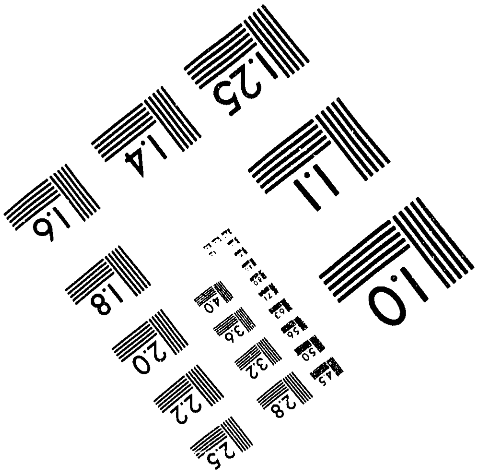

MANUFACTURED TO AIIM STANDARDS
BY APPLIED IMAGE, INC.

2 of 2

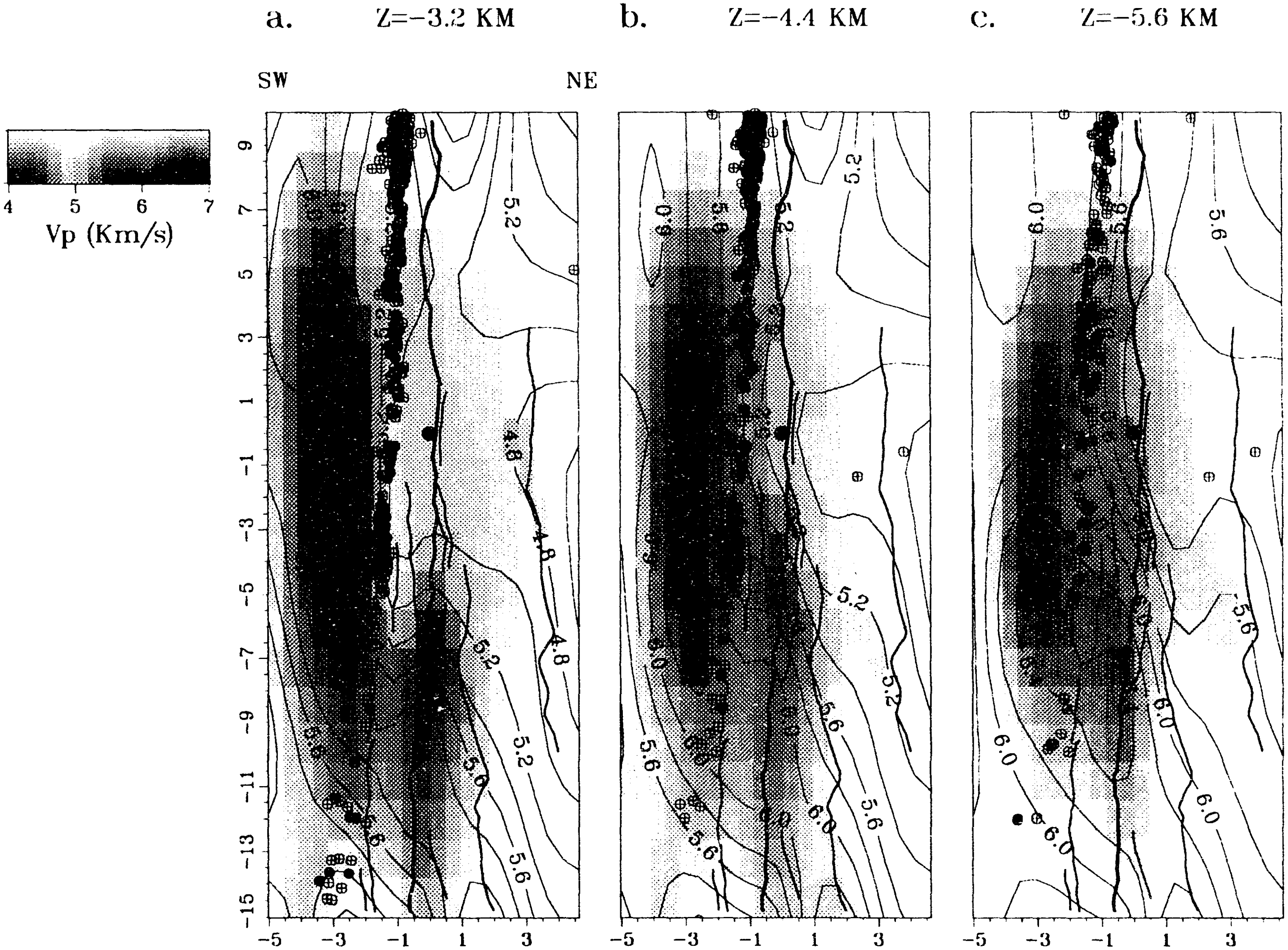

Figure 5.4a,b,c

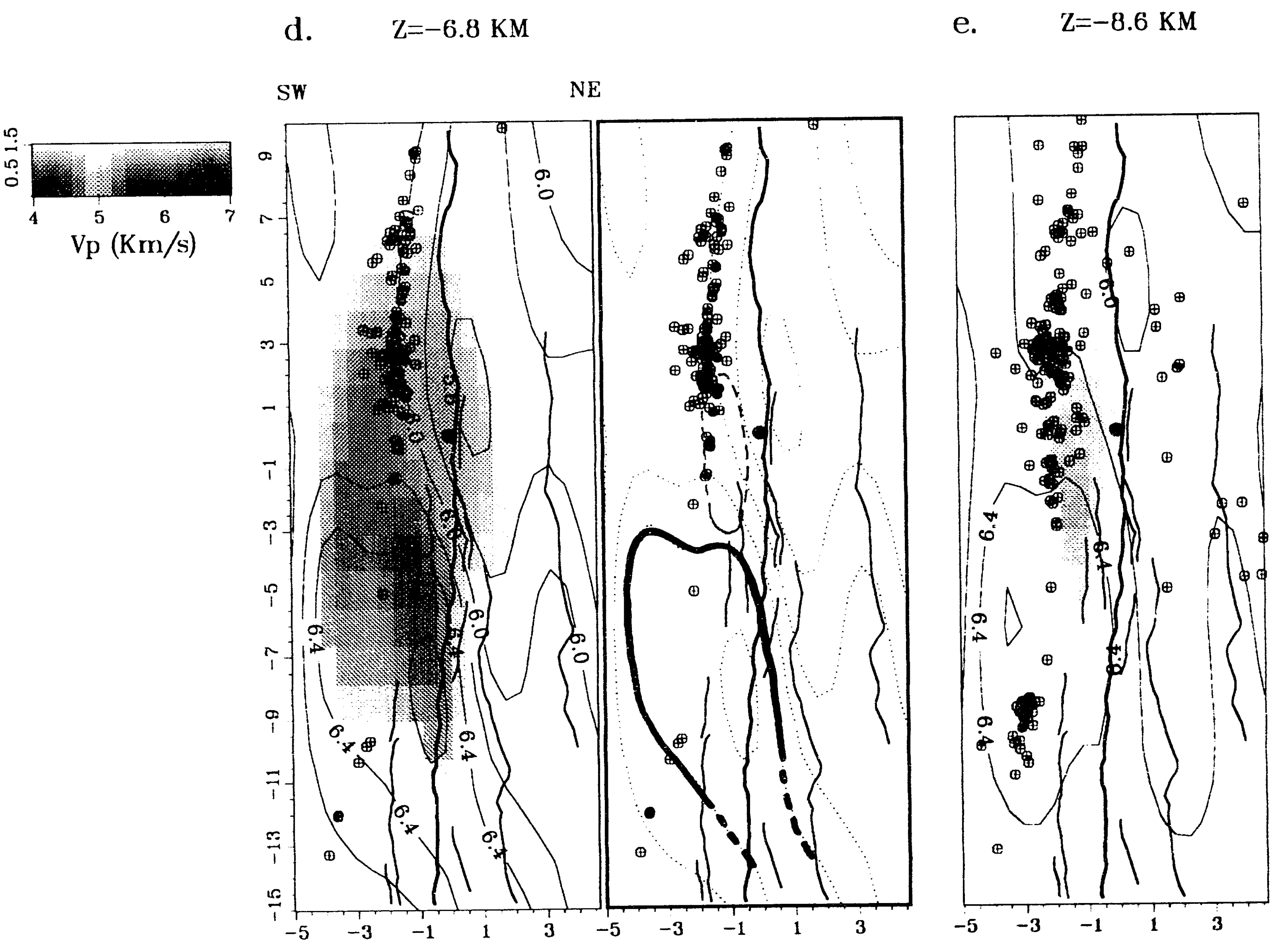d.
Z=−6.8 KM
e.
Z=−8.6 KM
SW
NE
0.5 1.5
4
5
6
7
Vp (Km/s)
6.0
6.4
9
7
5
3
1
−1
−3
−5
−7
−9
−11
−13
−15
−5
−3
−1
1
3

Figure 5.4d,e

Figure 5.5: Across-strike (SW-NE) sections through Parkfield 3-D V_p model. Contour interval 0.2 km/s. Bottom panel of each figure shows lithological interpretation. Lithological units: **gm**, Salinian block; **KJf**, Franciscan formation; **Ts**, Tertiary marine and non-marine sediments; **Mv**, Miocene volcanic rocks; **gb**, gabbro. Arrows indicate major faults (see fig 5.2) and locations of velocity profiles A-E shown in fig 5.7. Filled circles are clustered earthquakes, open circles other background seismicity and crosses 1966 aftershocks. Hypocenters projected from 1.25 km on either side of section plane.

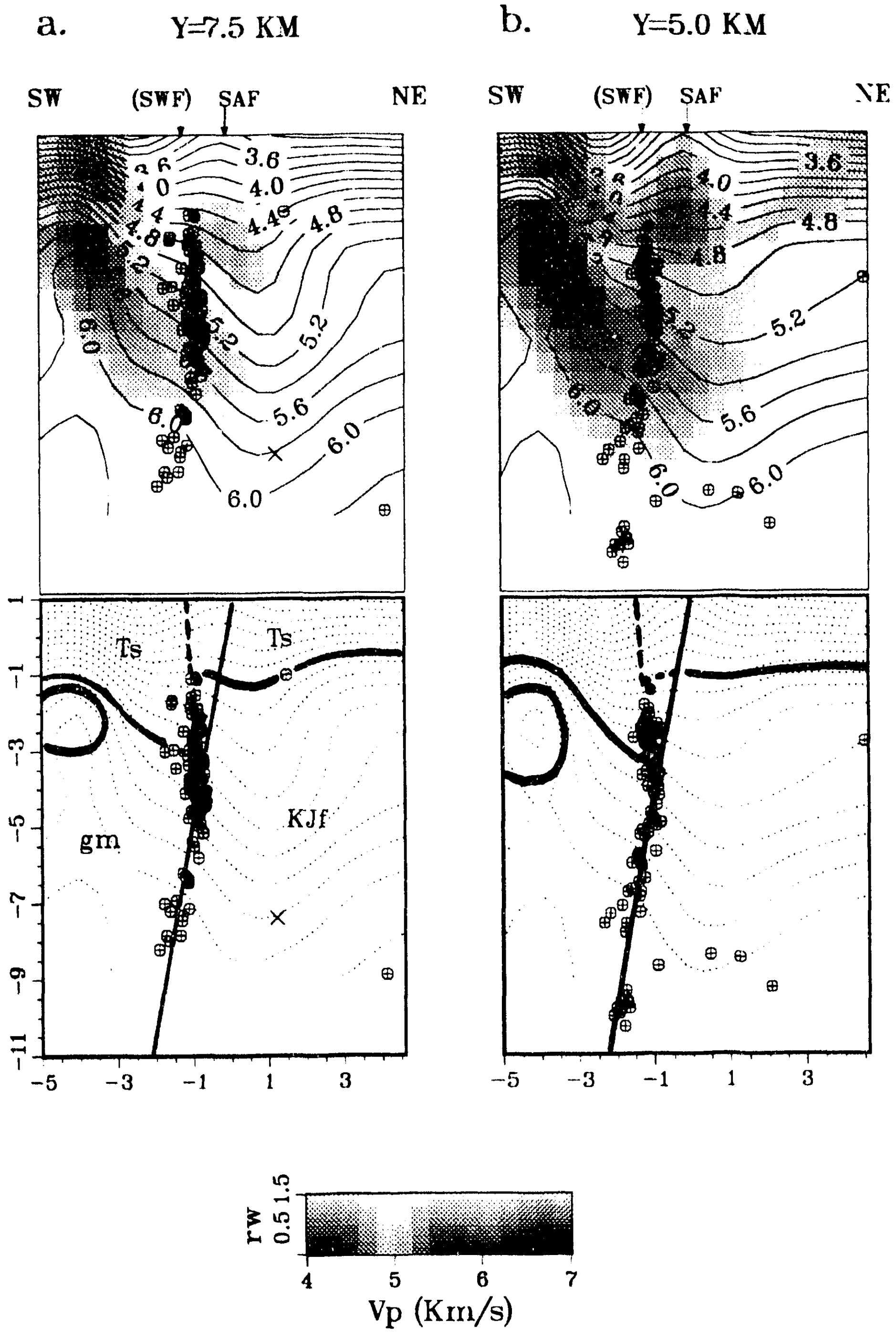
a.
Y=7.5 KM
b.
Y=5.0 KM
SW
(SWF)
SAF
NE
3.6
4.0
4.4
4.8
5.2
5.6
6.0
Ts
gm
KJf
1
-1
-3
-5
-7
-9
-11
-5
-3
-1
1
3
rw
0.5 1.5
4
5
6
7
Vp (Km/s)

Figure 5.5a,b

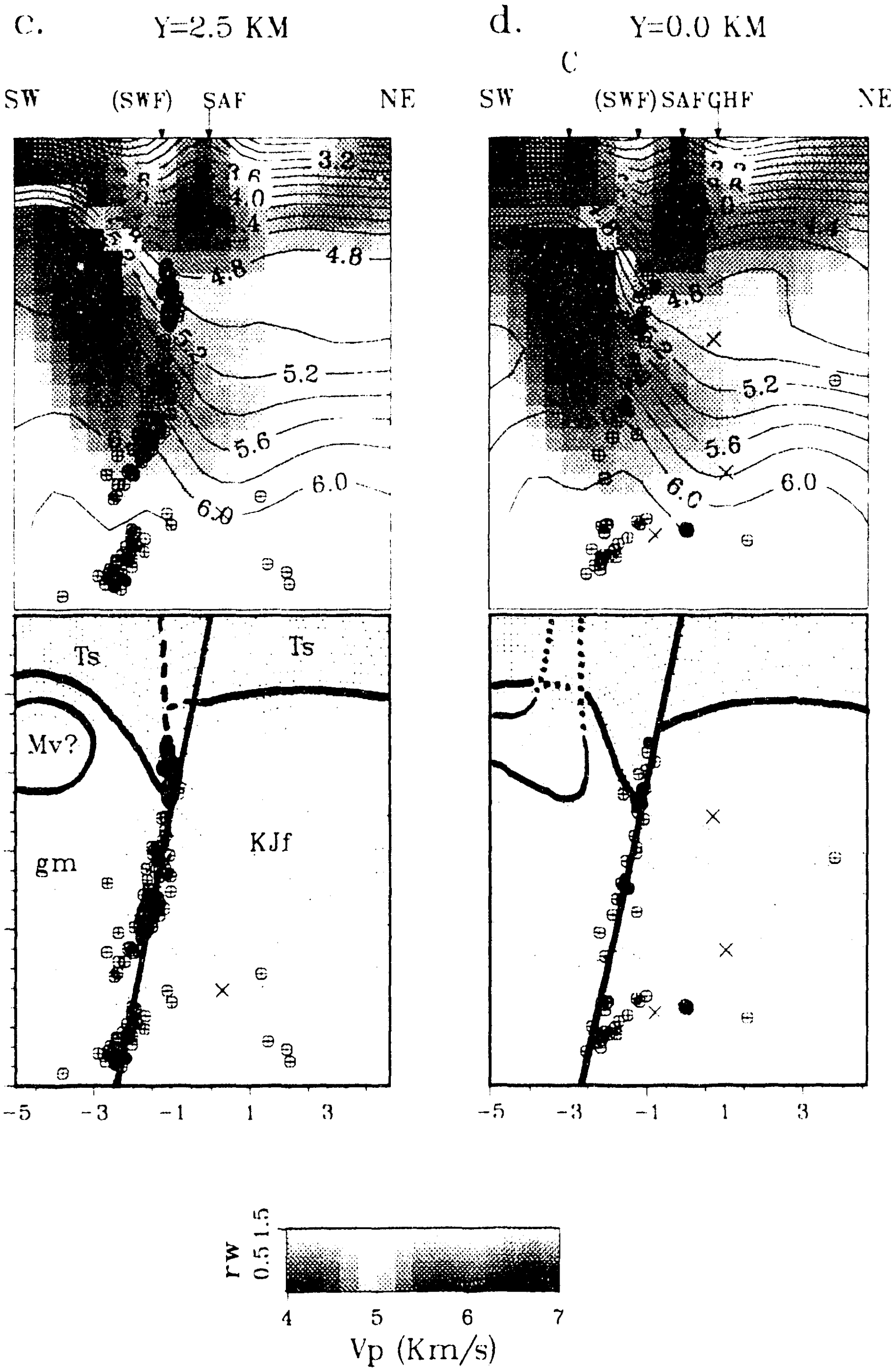
c.
Y=2.5 KM
SW
(SWF)
SAF
NE
3.2
3.6
4.0
4.4
4.8
5.2
5.6
6.0
Ts
Ts
Mv?
gm
KJf
d.
Y=0.0 KM
C
SW
(SWF)
SAF
CHF
NE
4.8
5.2
5.6
6.0
1
−1
−3
−5
−7
−9
−11
−5
−3
−1
1
3
rw
0.5
1.5
4
5
6
7
Vp (Km/s)

Figure 5.5c,d

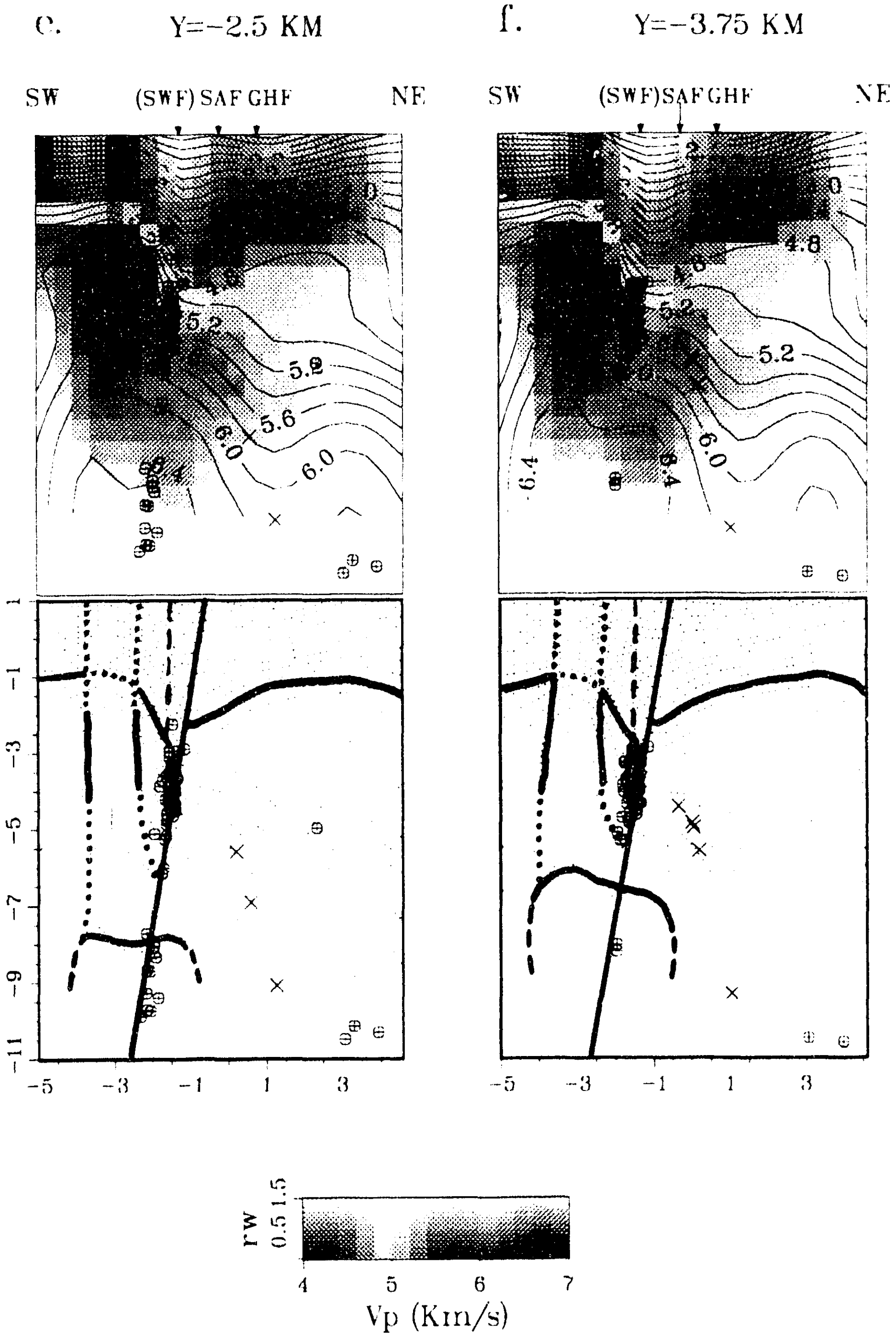
e.
Y=-2.5 KM
f.
Y=-3.75 KM
SW
(SWF) SAF GHF
NE
SW
(SWF)SAF GHF
NE
4.8
5.2
5.2
5.6
6.0
6.0
6.4
6.4
6.4
4.8
5.2
6.0
1
-1
-3
-5
-7
-9
-11
-5
-3
-1
1
3
-5
-3
-1
1
3
rw
0.5 1.5
4
5
6
7
Vp (Km/s)

Figure 5.5e,f

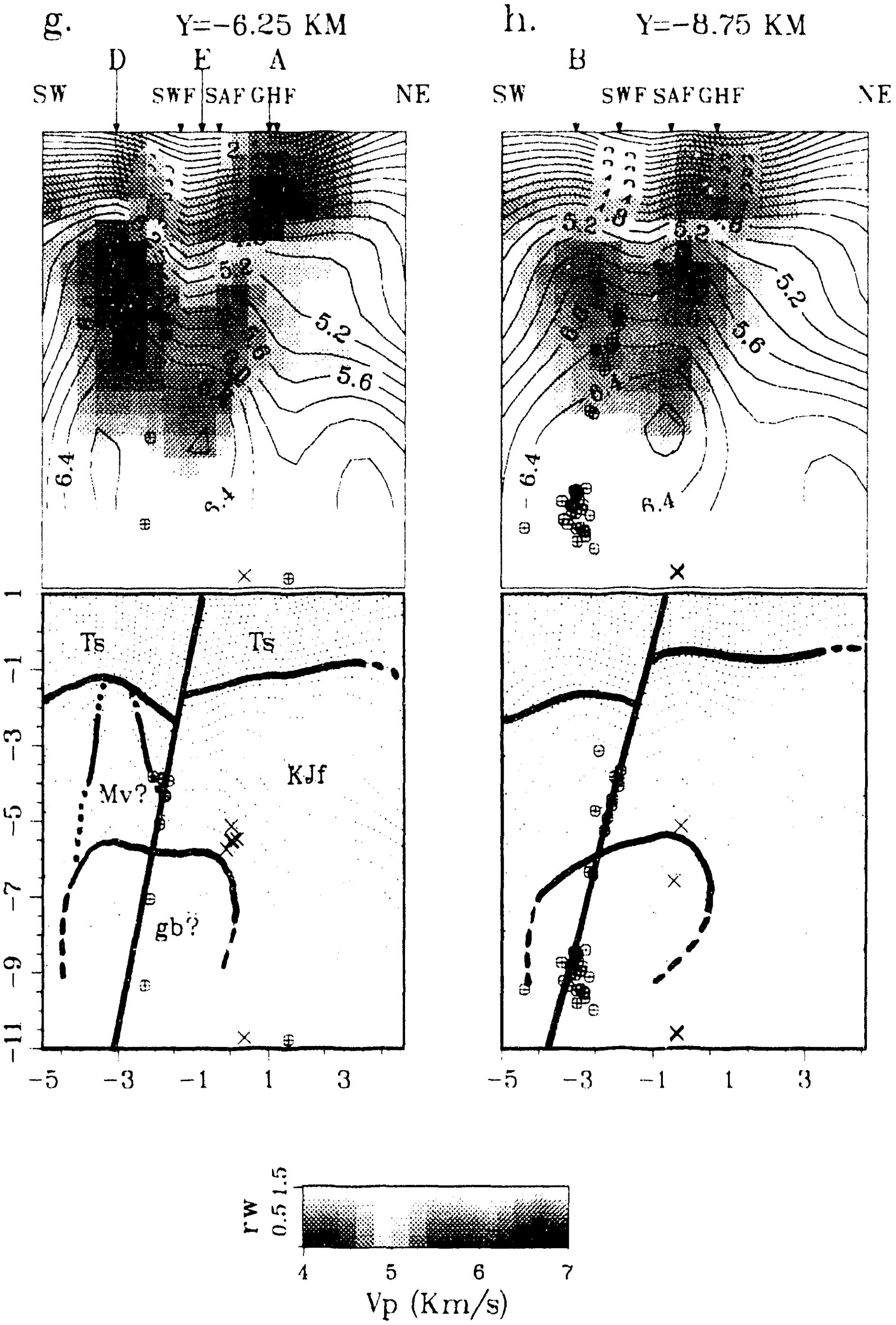
g.
Y=-6.25 KM
D
E
A
SW
SWF SAF GHF
NE
h.
Y=-8.75 KM
B
SW
SWF SAF GHF
NE
5.2
5.6
6.4
Ts
Ts
KJf
Mv?
gb?
1
-1
-3
-5
-7
-9
-11
-5
-3
-1
1
3
rw
0.5 1.5
4
5
6
7
Vp (Km/s)

Figure 5.5g,h

Figure 5.6: Along-strike (SE-NW) sections through Parkfield 3-D V_p model. Contour interval 0.2 km/s. Bottom panel of **b**. shows lithological interpretation at x=-0.68 km (see fig 5.5 for explanation), positive V_p/V_s anomaly from fig 5.13b shown in red. Mainshock hypocenter shown as red circle. See fig 5.5 for seismicity symbols. Hypocenters projected from 1 km on either side of section plane. Surface creep rate profile in **b**. based upon data from Burford and Harsh (1980) (circles) and Lienkaemper and Prescott (1982) (triangles).

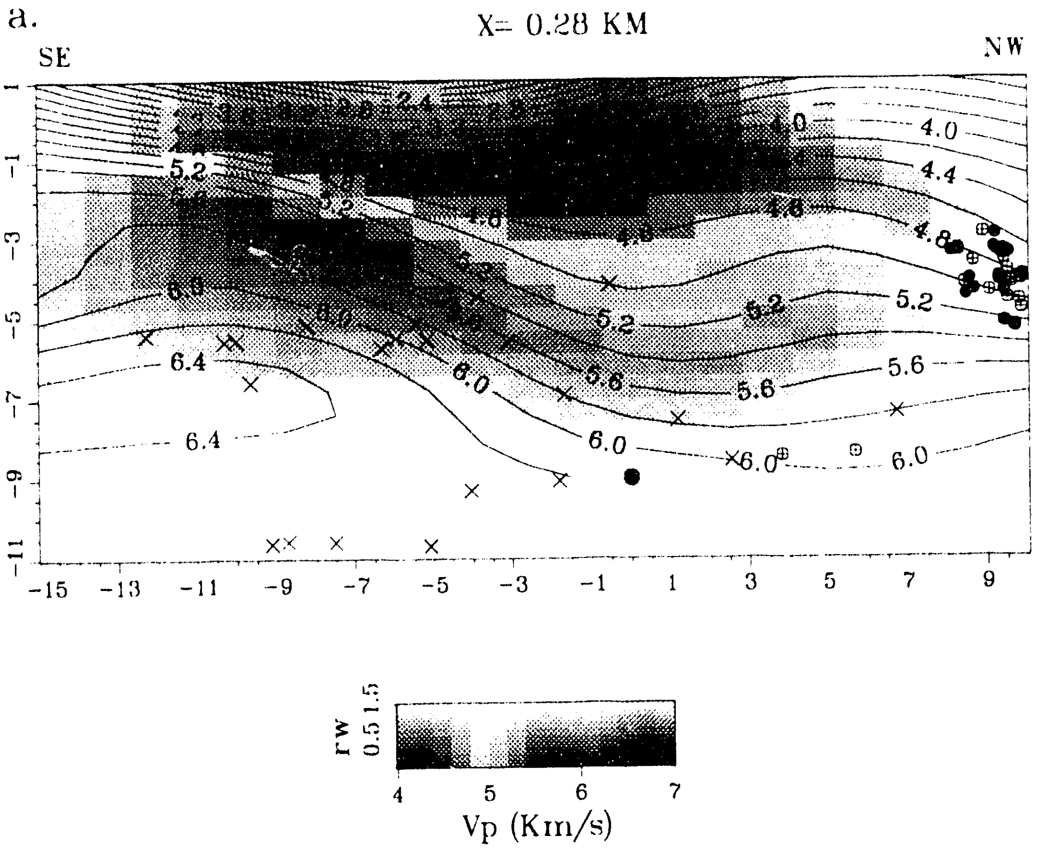
a.
X= 0.28 KM
SE
NW
1
-1
-3
-5
-7
-9
-11
-15
-13
-11
-9
-7
-5
-3
-1
1
3
5
7
9
2.4
4.0
4.0
4.4
4.8
4.8
4.8
4.8
5.2
5.2
5.2
5.2
5.2
5.6
5.6
5.6
5.6
6.0
6.0
6.0
6.0
6.0
6.0
6.0
6.4
6.4
rw
0.5 1.5
4
5
6
7
Vp (Km/s)

Figure 5.6a

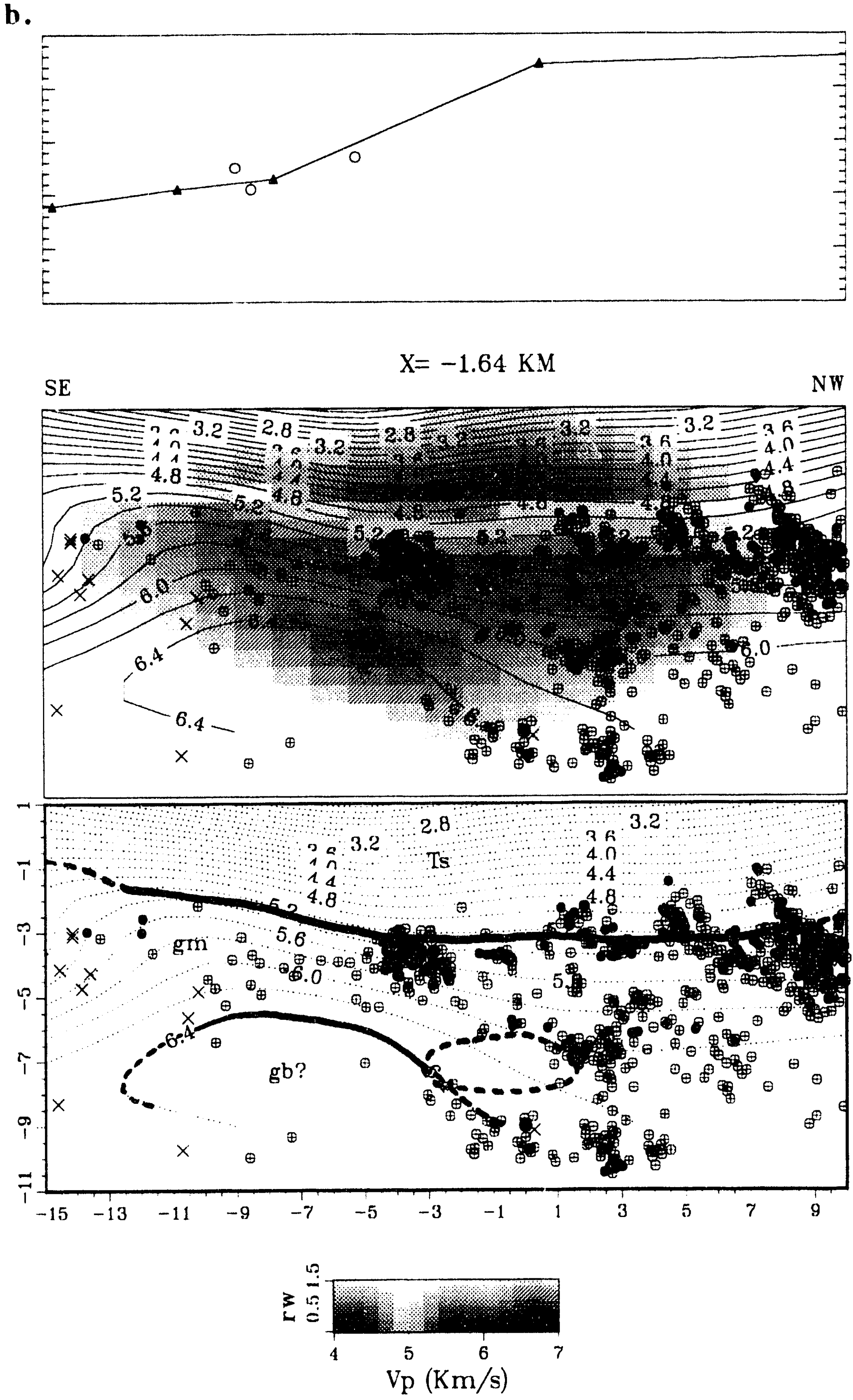
b.
25
20
15
10
5
0
slip rate (mm/yr)
X= −1.64 KM
SE
NW
3.2
2.8
3.6
4.0
4.4
4.8
5.2
5.6
6.0
6.4
Ts
gm
gb?
1
−1
−3
−5
−7
−9
−11
−15
−13
−11
−9
−7
−5
−3
−1
1
3
5
7
9
rw
0.5 1 1.5
4
5
6
7
Vp (Km/s)

Figure 5.6b

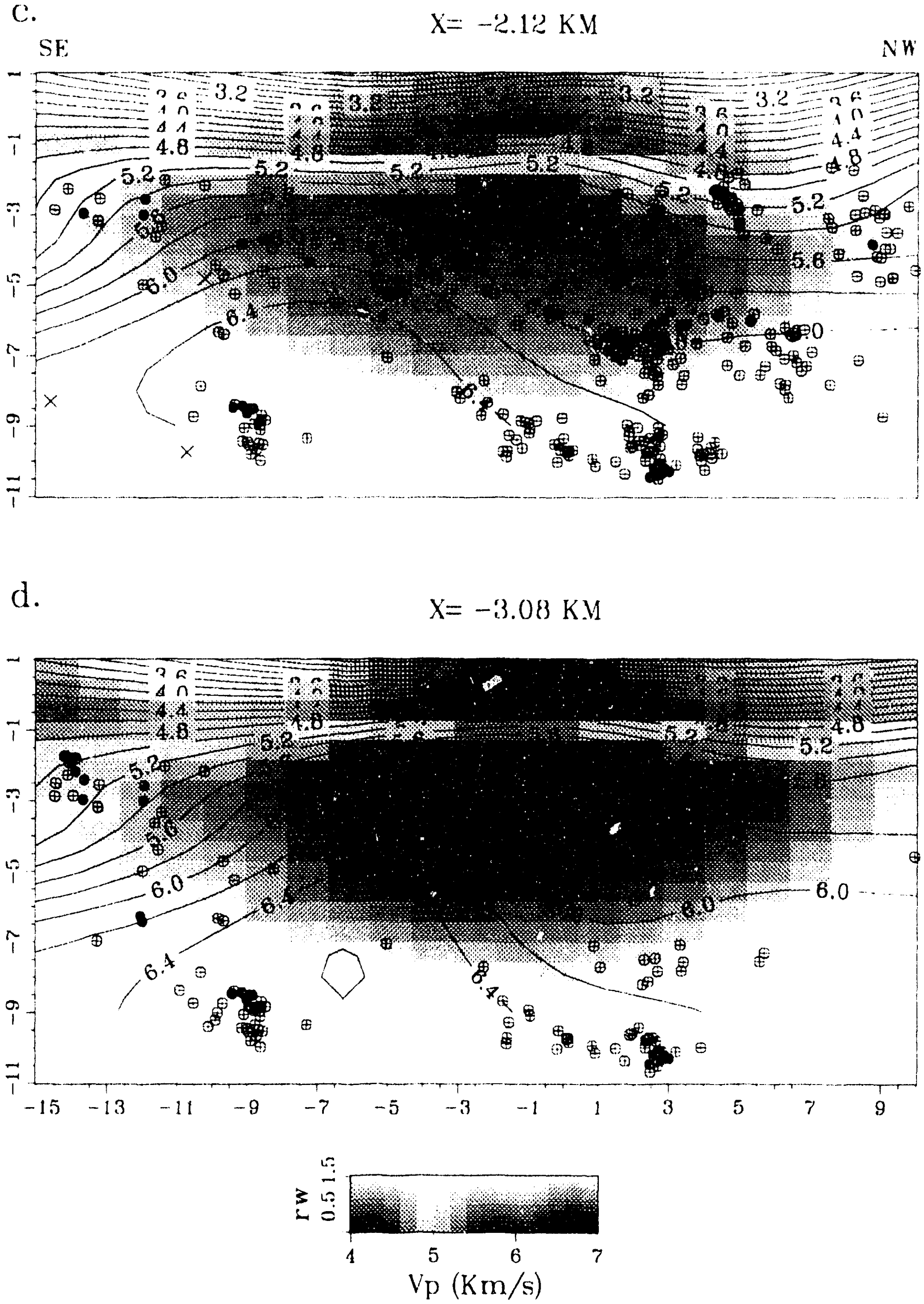
c.
X= -2.12 KM
SE
NW
1
-1
-3
-5
-7
-9
-11
3.2
3.6
4.0
4.4
4.8
5.2
5.6
6.0
6.4
d.
X= -3.08 KM
-15
-13
-11
-9
-7
-5
-3
-1
1
3
5
7
9
rw
0.5 1.5
4
5
6
7
Vp (Km/s)

Figure 5.6c,d

sliced and shattered rock. The main outcrop of Franciscan rocks and Coast Range ophiolite is bounded by the NE-dipping Table Mountain thrust fault SE of y=7, and by the SAF itself to the NW. The Great Valley sequence is absent, apart from local occurrences of limited extent (Dickinson, 1966; Sims, 1990). Within the wedge of deformed upper crust between the SAF and the Table Mountain fault, the two main structures are the SW-dipping Gold Hill and Jack Ranch faults (fig. 5.2). The Gold Hill and Table Mountain faults bound the Parkfield Syncline, within which the Franciscan formation is overlain by Miocene to Pliocene marine and non-marine sedimentary rocks (Sims, 1988, 1990). The arcuate Jack Ranch fault bounds the Gold Hill block immediately to the SE of the study area(fig. 5.1). The Gold Hill block is a hornblende-quartz and anorthositic gabbro body that is closely similar in composition to the Logan gabbro described in Section 4.2.4 (Ross, 1972; Simms, 1989). This gabbro body outcrops at Gold Hill, 4 km SE of the model area.

Southwest of the SAF the Salinian basement is overlain by a thick section of Miocene to Pliestocene sediments. Volcanic rocks consisting mainly of flow-banded rhyolite, obsidian, rhyolite breccia and some dacite outcrop along a 1 km-wide, fault-bounded band about 2 km SW of the SAF trace between y=-6 and y=3 km (Sims, 1989). These rocks are poorly exposed, the best exposure being at Lang Canyon.

The main structural feature SW of the SAF is the Southwest Fracture Zone (SWFZ), which is an *en-echelon* right-lateral strike-slip fault sub-parallel to the main SAF trace (fig. 5.2). Ten km SE of the model area the main SAF trace is offset 1.5-2 km to the right across the Cholame Valley (fig. 5.1). Sims (1988,1989) suggests that the SWFZ is a continuation of the SW *en echelon* segment of the SAF on the SW side of Cholame Valley, based upon a set of short fault scarps that extends between ends of the mapped exposures of the two faults. Sims (1989) also suggests that the SAFZ merges with the SAF at Middle Mountain. Brown et al. (1967) measured 2.6 cm of right-lateral displacement across this fault after the 1966 Parkfield earthquake.

5.2.2 Relation Between the V_p Model and Surface Geology

The lack of basement outcrops within the Parkfield model area make correlations of the shallow velocity model with surface geology less definitive than at Loma Prieta. Near-surface velocities on the NE side of the SAF in the area where the Franciscan basement outcrops are poorly resolved, and do not appear to correlate with the outcrop. Elsewhere on the NE side of the SAF the generally low velocities correlate with the thick sediments of the Parkfield Syncline. There is no evidence for the outcropping Franciscan rocks on the gravity map either, but the intense aeromagnetic anomalies reflect the outcrops of serpentinite. The ridge of high velocity centered on x=0 that extends from the SE edge of the model to about y=-9 km may correspond to a shallow sub-surface extension of the Gold Hill gabbro body. The Gold Hill block is bounded by the Jack Ranch fault to the NE, E and SE, but its northwestern extent is concealed beneath Pleistocene deposits and probably extends at least as far as y=-10 km (J. Sims, personal communication, 1992). Michael and Eberhart-Phillips (1991) show a positive V_p anomaly centered on Gold Hill. The velocity ridge corresponds to similar features on the gravity and aeromagnetic maps.

There is much more character in the shallow velocity model on the SW of the SAF. Adjacent to the fault, an elongated velocity low extends from y=-11 to y=7 km. This low is most intense between y=-7 and y=1 km, where it indicates pooling of sediments in the Middle Mountain Syncline between the SWFZ and the SAF. The SW boundary of this velocity feature at x=-2 to -2.5 km is a steep and remarkably linear velocity gradient. Southeast of y=-9 this gradient is coincident with the mapped trace of the southwesterly *en echelon* segment of the SWFZ. Sims (1989, 1990) suggests that this segment of the SWFZ continues to the NW under the surficial sediments and is the northeastern boundary fault of the Lang Canyon volcanic body, the outcrops of which correlate exactly with the high velocity ridge that extends between y=-6 and y=8 km SW of x=-2. The most intense part of this velocity high is located between y=1 and y=7 km, extending NW of the volcanic outcrops. There are moderately steep gradients on the aeromagnetic and gravity maps roughly coincident with the linear velocity gradient, the former extending between y=-7 and 10 km and the latter between y=-7 and y=3 km.

In summary, absence of outcrops of basement rocks within well-resolved parts of the near surface velocity model makes the correlation with surface geology less satisfactory than at Loma Prieta. However, the apparent correlation of velocity anomalies with the small outcrops of exotic rocks on both sides of the SAF and with structural features to the SW is encouraging.

5.2.3 Interpreting Deeper Features of the V_p Model

Figures 5.7a and 5.7b show the $V_p(z)$ model profiles for the Franciscan formation and the Salinian block at Parkfield, respectively. The laboratory data shown in these figures are the same as those for Loma Prieta shown in Figure 4.7. No seismic refraction data are available for the immediate Parkfield area. Stewart and O'Neill (1972) carried out refraction surveys along NW-SE profiles located 3-5 km on either side of the SAF (see also Eaton et al., 1970). Both profiles extend 20 km to the SE from about 1 km off the SE end of the Parkfield model area. The maximum depth of penetration along both profiles was 3.5-4 km. The southeastern-most shot point of the Gabilan profile of Walter and Mooney (1982) described in Section 4.2.2 is at (x,y) = (-11, 4) in model coordinates. The SE end of Walter and Mooney's Diablo profile NE of the SAF is about 70 km NNW of Parkfield, but $V_p(z)$ data from this profile are included in Figure 5.7a to provide constraint on Franciscan velocities below 5 km depth. The locations of the model profiles (A-E) shown in Figure 5.7 are given in Figure 5.5.

Profile A. Profile A (y=-6.25 km), through the Parkfield Syncline, reaches the lower bound of Franciscan velocities at 2-2.5 km depth (z=-1 to -1.5). This profile is 0.75 km SE and 0.3 km NE of the Varian well, within which the depth to Franciscan basement is 1.7 km. Sims (1990) shows the sediment/Franciscan contact NE of the Gold Hill fault dipping approximately 50° NE. Therefore, the depth to Franciscan basement estimated from Profile A is in close agreement with the well data. The velocity of the uppermost Franciscan rocks estimated from Profile A is about 4.5 km/s, which is close to the uppermost Franciscan velocity of 4.3 km/s in the refraction model of Stewart and O'Neill (1972). Therefore, the 4.4 km/s contour

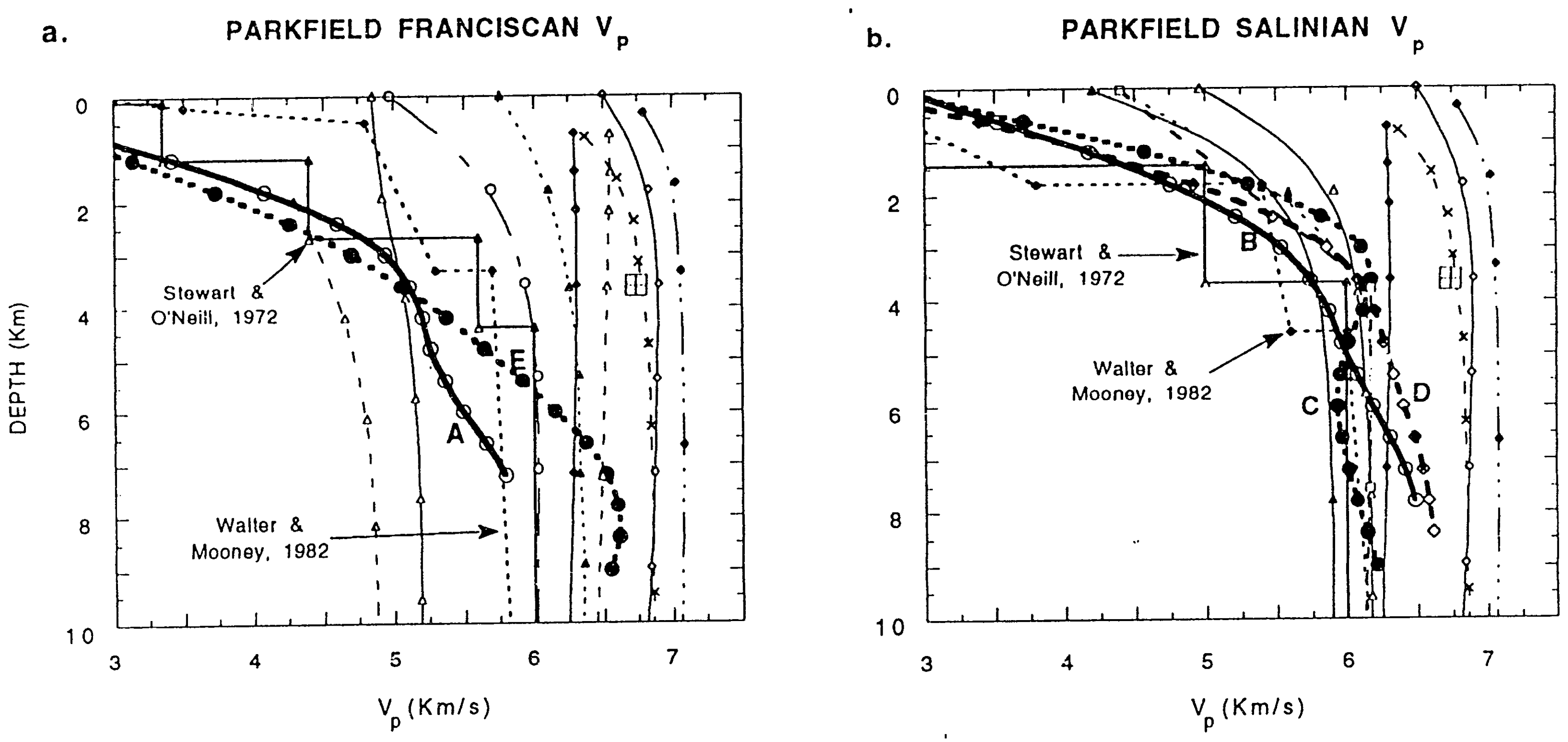

Figure 5.7: Parkfield model (bold curves) and experimental $V_p(z)$ profiles for (**a**) Franciscan formation and (**b**) Salinian block. Locations of model profiles A-E shown on Figure 5.5. Ordinate is depth below surface. See fig 4.7 for explanation.

in the three-dimensional model is adopted as the sediment/Franciscan contact. This estimate is close to the lower bound of Franciscan velocities, and is considerably lower than the 4.9 km/s velocity estimated for the contact at Loma Prieta. Profile A remains within the Franciscan range of velocities to the limits of model resolution at about 7.5 km depth (z=-6.5) at this location. The overlying sediments appear undeformed and deepen gradually from SE to NW.

Profile B. Profile B (y=-8.75) is through the Salinian block and overlying sediments to the SW of the SWFZ and SE of the outcropping volcanic rocks of Lang Canyon. The slope of Profile B begins to steepen at 2.3 to 2.5 km depth (z=-1.3 to -1.5), which is assumed to indicate approximately the top of the granitic basement. The model velocity at this depth is 5.3 km/s. The lower range of granite laboratory velocities is not reached until 3.5 km depth. However, both Salinian refraction models have velocities that also fall below the laboratory range of values above a depth of 3.5-4.5 km (fig. 5.7). The refraction model of Walter and Mooney (1982) has an uppermost granite velocity of 5.4 km/s at 2.0 km depth about 10 km WNW of the location of Profile B. This velocity is in good agreement with my estimate of 5.3 km/s from Profile B The 5.3 km/s model contour is therefore adopted as the sediment/Salinian contact, which is the same as that for the Loma Prieta model. The refraction model of Stewart and O'Neill (1972), 16 km to the SE of Profile B, has an uppermost basement velocity of 5.0 km/s at 1.5 km depth. Well data 20-30 km SE indicate basement depths ranging from 1.2 to 2.0 km (Shedlock et al., 1990), and geological estimates in the Parkfield area range from 1.5 to 2.5 km (Page et al., 1979; Dibblee, 1980). Below 6 km Profile B exceeds the upper bound on the range of Salinian velocities as it enters a zone of high velocity deeper in the section.

Profile C. Profile C (y=0.0) is located SW of the SWFZ at the NW end of the surface exposures of the Lang Canyon volcanic rocks, and at about the center of the elongated high velocity ridge seen in the near-surface model (fig. 5.3). At depths between 2 km (z=-1) and 4 km (z=-3) the velocities along this profile are significantly higher (up to 0.6 km/s) than those along Profile B and the uppermost granite velocity of Walter and Mooney's refraction model. Between 2.5 and 4 km the Profile C velocities exceed the upper bound of laboratory estimates for Salinian granite Below 4 km depth Profile C is confined within the narrow range of granite velocities and agrees closely with the Walter and Mooney model.

Profile C, therefore, indicates that the anomalously high velocities that appear at depths as shallow as 2 km below the surface in the model cross-sections between y=-6 and y=8 km are a real feature. Northwest of y=0 the shallow high velocities define a lenticular body between depths of 2 and 4.5 km (z=-1 and -3.5) (figs. 5.3, 5.4). To the SE, between y=-1 and y=-6 km, the body becomes elongated in depth and merges with deeper high velocities. The apparently near-vertical NE boundary of the body SE of y=0 is difficult to define within the resolution of the model, but detailed examination suggests the general shape shown in the interpretive panels of Figure 5.5. The near-vertical SW boundary could be an artifact of the poor resolution of the southwestern edge of the model below z=-4 km; Michelini's (1991) synthetic fault model tests showed a tendency for velocity contours to be pulled too deep near the edge of the high-velocity side of the model (see Section 3.2). The boundary between the bottom of the body and the deeper high-velocity body is also difficult to define. Therefore, the shallow high velocity body could be limited to the 2-4.5 km depth range and could be continue to the SW beyond the edge of the model.

The almost perfect coincidence of the SE-NW axis of this velocity anomaly between y=-6 and y=0 km with the narrow (1 km) band of volcanic outcrops strongly suggests a causal relationship. The Lang Canyon volcanic rocks are correlative with the Neenach Volcanics to the SE in the San Emigdio Mountains and with the Pinnacles Volcanics at the SE end of the Gabilan Range (Ross, 1972; Sims, 1989). The much larger exposures at the Pinnacles consist of dacite, andesite and rhyolite. John Sims (personal communication, 1992) estimates the unit thickness at the Pinnacles as 2.2 km, and interprets the Lang Canyon outcrops as the upper edge of an up-tilted, near-vertical slab of volcanic rocks having this thickness and unknown depth extent. This suggests that the interpretation shown in Figure 5.5 might be correct. However, the standard reference (Carmichael, 1982) lists no velocity data for volcanic rocks apart from basalts, so this hypothesis cannot be tested at present. The high-velocity rock mass does not disrupt the overlying, apparently flat-lying Tertiary sediments even where the volcanic rocks outcrop, but this may be a result of weathering of the uppermost edge of the slab. The relatively steep, linear aeromagnetic gradient that coincides with the NE boundary of the high-velocity body (fig. 5.3) is actually the NE side of a 10 km-wide (in x) rectangular magnetic high (Wentworth et al., 1992). R. Jachens (personal communication, 1992) considers this to be related to a topographic feature on the granitic basement surface, but there is no corresponding expression in the gravity data (Wentworth et al., 1992).

The Lang Canyon volcanics play an important role in arguments concerning the evolution and displacement history of the SAF system. Sims (1989, 1990) suggests that the southwestern boundary fault of the Lang Canyon volcanic body is the extension of the Chimineas-San Juan-Red Hills-White Canyon fault system, along which he finds evidence for Holocene displacement and which he identifies as an ancestral active trace of the SAF.

Profiles D and E. Between y=-2 and y=-11 km the southwestern half of the model below a depth of 6 km (z=-5) is occupied by a high-velocity body. This feature is very similar to the high-velocity body identified at Loma Prieta, and I will base my discussion upon a comparison between the two bodies. In comparison with Profile C in Figure 5.7b, the velocity along Profile D, which also penetrates the shallow high-velocity body, continues to increase beyond the range of granite velocities at depths below 4 km (z < -3) to a maximum resolved velocity of 6.6 km/s at 8-8.5 km depth (z=-7 to -7.5). Profile B similarly reaches a velocity well beyond the granite range. A much higher velocity (7.2 km/s) is reached within the high-velocity body at Loma Prieta, but at a depth of about 10 km. At 8 km depth (z=-7) on Loma Prieta Profile D (fig. 4.7b) the velocity is 6.7 km/s, comparable with that in the Parkfield model. Therefore, it is possible that if the Parkfield model were resolved at greater depths a higher maximum velocity might be observed. More importantly, however, the velocity maximum on Parkfield Profile D is significantly higher (0.4 km/s) than the Walter and Mooney refraction model and the QM1 granite velocity. Profile E, NE of the SAF, similarly reaches a velocity of 6.6 km/s at about 8 km depth (z=-7), which is 0.8 km/s higher than the Walter and Mooney model for Franciscan crust at this depth, and 0.3 km/s higher than sample P5, the highest grade (jadeite facies) Franciscan metagraywacke studied by Stewart and Peselnick (1977).

As at Loma Prieta, I chose the 6.4 km/s contour as the boundary of the high-velocity body. So defined, the high-velocity body shown in Figures 5.4-5.6 is similar in form to that at Loma Prieta; a domed rock mass, roughly elliptical in map view and longitudinal section with the major axes oriented along the strike of the SAF. Like the Loma Prieta body, the Parkfield anomaly crosses beneath the trace of the SAF. The Parkfield body is smaller in scale, measuring about 4.5 km in width (x) by 9 km in length (y), compared with the 10 km width and 30 km length of the Loma Prieta body. The Parkfield body extends to within 5-6 km from the surface, while that at Loma Prieta reaches a minimum depth of 7-8 km. The Parkfield body is not resolved at depths greater than 9 km.

The high-velocity ridge on the NE side of the SAF identified in the near-surface model as a possible subsurface extension of the Gold Hill gabbro body (Section 5.2.2) can be followed to a depth of about 6.5 km (z=-5.5) from the SE edge of the model to y=-7 km. However, resolution of this part of the model SE of y=-11 is marginal so the definition of this feature is tenuous. In map view the high-velocity ridge is seen to converge with the SAF, and it merges with the deep high-velocity body between y=-11 and y=-7 km (fig. 5.4c). Therefore, it appears that the part of the high-velocity body NE of about x=-1.5 could be the end of the subsurface extension of the Gold Hill gabbro body. Alternatively, the ridge of high velocity is the continuation of the high-velocity body to the NE of the fault, and is unrelated the Gold Hill gabbro. The latter alternative would be favored by other workers who, based upon aeromagnetic data (R. Jachens, personal communication, 1992) and the regional V_p model (Michael and Eberhart-Phillips, 1991), argue that the Gold Hill body is only 1-2 km thick. The gravity contours in this part of the model (fig. 5.3) mimic the velocity model. The possible relationship of the high-velocity body to the Gold Hill gabbro is further explored in Section 5.3.1 below.

5.2.4 Other Evidence for the Deep High Velocity Body

There is no evidence for the deep high velocity body in the aeromagnetic data (fig. 5.3 and Wentworth et al., 1992). Michael and Eberhart-Phillips (1991) present a regional-scale three-dimensional V_p model for Parkfield. The shape of the contour bounding the high velocities on the SW side of the SAF in this low-resolution model is similar to the outline of the shallow and deep high-velocity bodies merged together. McBride and Brown (1986) re-analyzed a COCORP seismic reflection line that crosses the fault zone through Parkfield. The crooked geometry of this line is centered approximately on y=-7.5. One of the main features of their section is a set of short horizontal reflectors SW of the SAF at about 3.4 s two-way travel time. Converting the travel time to depth using a model Salinian $V_p(z)$ profile at y=-7.5 km puts this horizon at about 7 km, approximately the same depth as the top of the deep high-velocity body. However, the set of reflectors extends to the SW beyond the edge of the Parkfield model.

Based upon the V_p model, the same range of candidate lithologies is possible for the Parkfield high-velocity body as for the Loma Prieta body (Sections 4.2.3 and 4.2.4). In the next section I examine the V_p/V_s model for possible further constraint.

5.3 The Parkfield V_p/V_s and V_s Models

Figures 5.8, 5.9 and 5.10 show the Parkfield V_s model in map view, across-strike section (SW-NE), and along-strike section (SE-NW), respectively. The V_p/V_s model is likewise shown in Figures 5.11-5.13. No spread function is calculated for the V_p/V_s model, but a rough idea of the resolution is provided by scaling color saturation by the spread function calculated for the V_s model.

This section is largely devoted to interpretation of the V_p/V_s model but I will first give a brief description of the V_s model. The general features of the V_s field are similar to the V_p model but, as anticipated from the discussion in Section 3.2, it is well-resolved over a smaller proportion of the model volume. Definition

Figure 5.8: Map views of Parkfield 3-D V_S model. Contour interval 0.1 km/s. See fig 5.4 for explanation of seismicity.

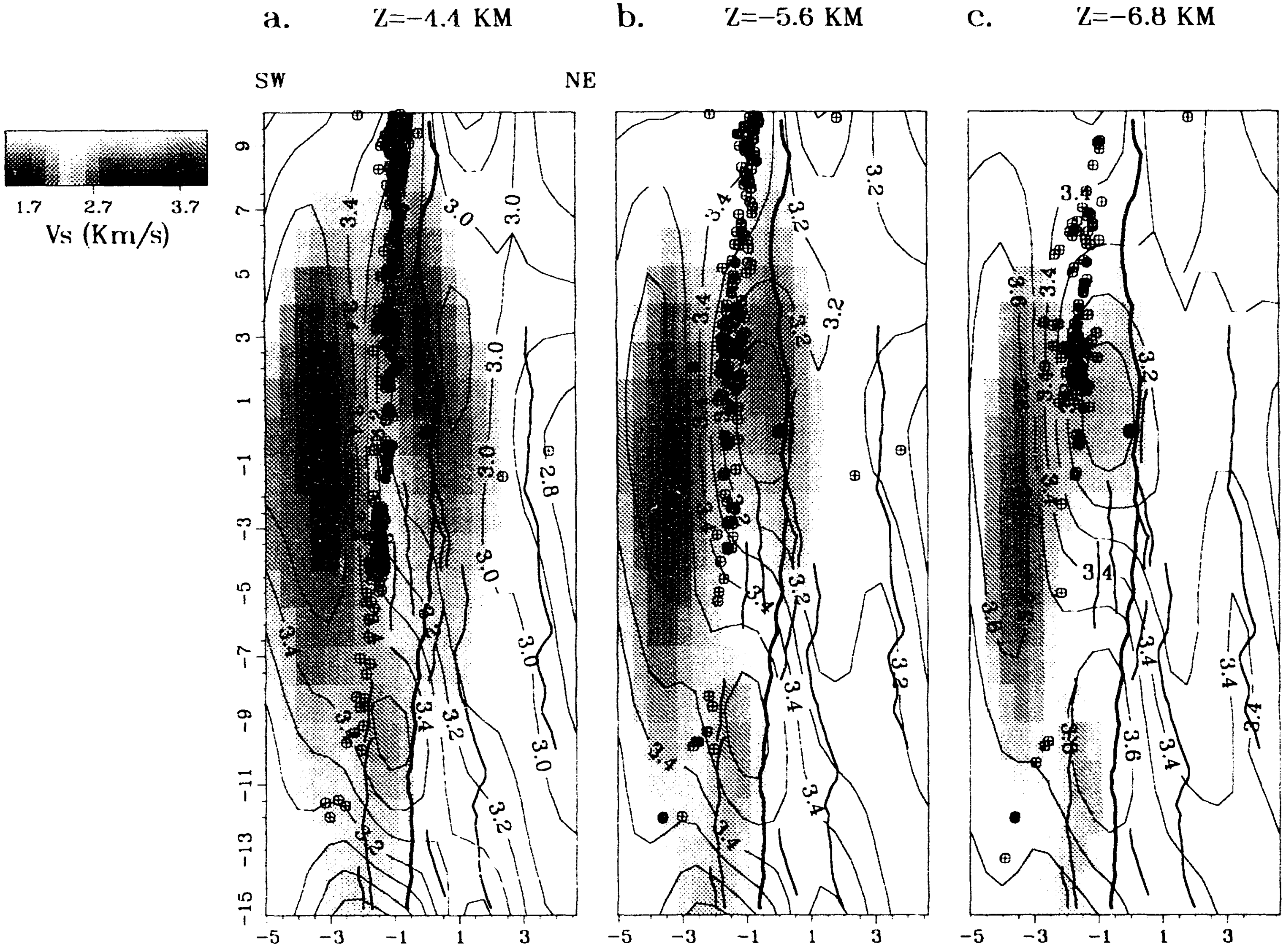

Figure 5.8a,b,c

Figure 5.9: Across-strike (SW-NE) sections through Parkfield 3-D V_S model. Contour interval 0.1 km/s. See fig. 5.5 for explanation of seismicity.

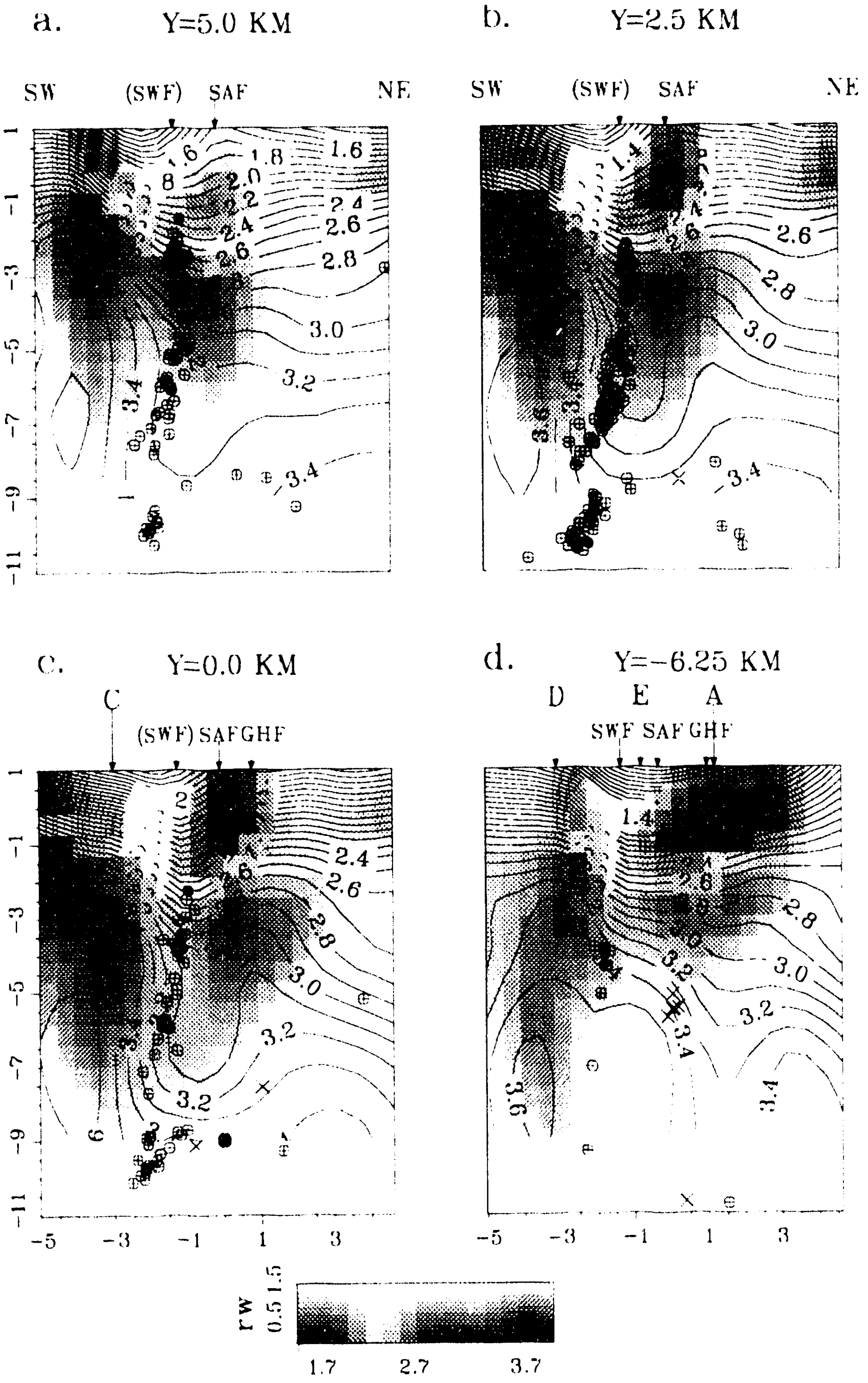
a.
Y=5.0 KM
b.
Y=2.5 KM
SW
(SWF)
SAF
NE
c.
Y=0.0 KM
C
(SWF) SAF GHF
d.
Y=-6.25 KM
D
E
A
SWF SAF GHF
1
-1
-3
-5
-7
-9
-11
-5
-3
-1
1
3
rw
0.5 1.5
1.7
2.7
3.7
Vs (Km/s)

Figure 5.9

Figure 5.10: Along-strike (SE-NW) sections through Parkfield 3-D V_S model. Contour interval 0.1 km/s. See fig. 5.5 for explanation of seismicity.

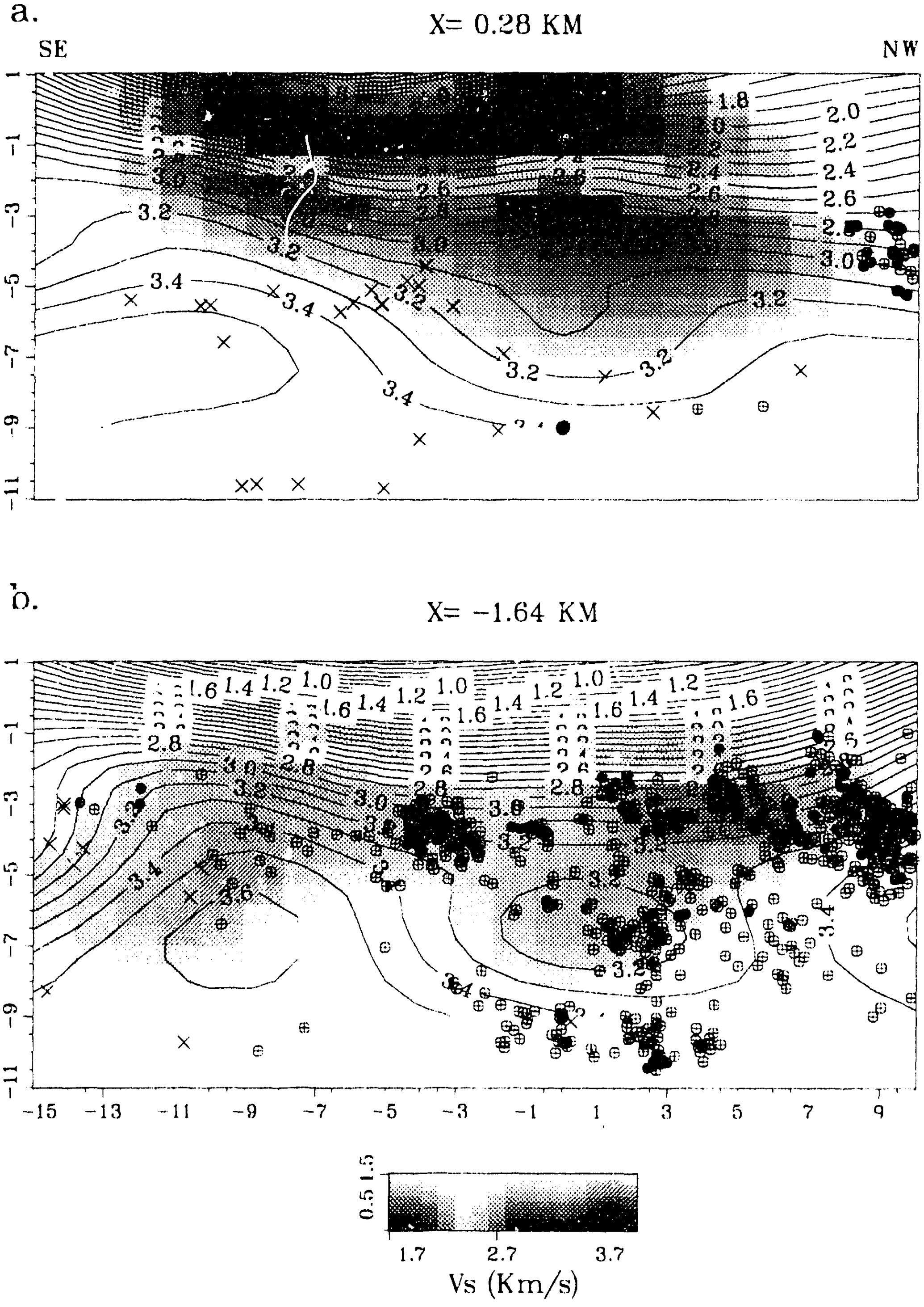

Figure 5.10a,b

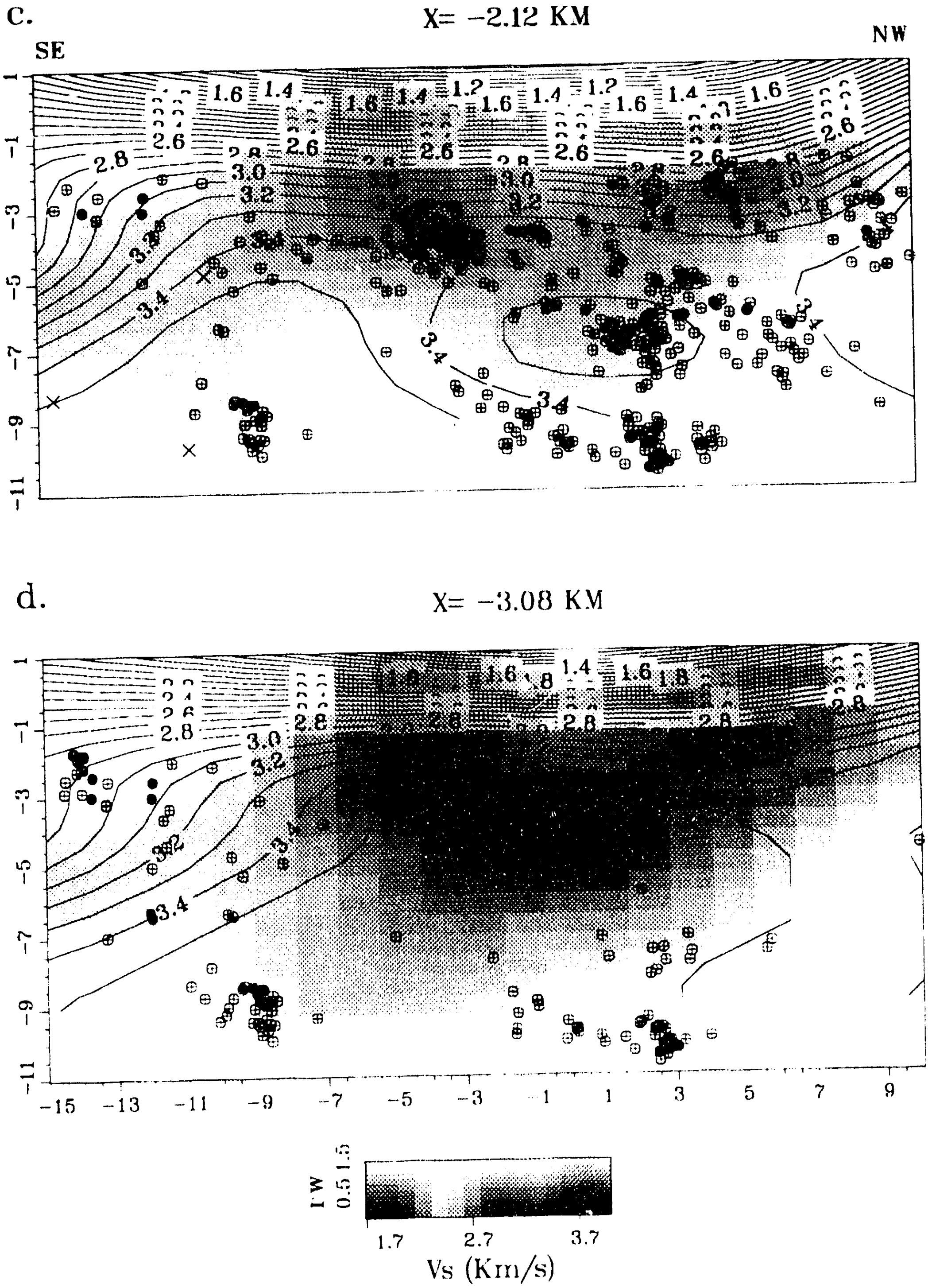

Figure 5.10c,d

Figure 5.11: Map views of Parkfield 3-D V_p/V_s model. Contour interval 0.05. See fig 5.4 for explanation of seismicity.

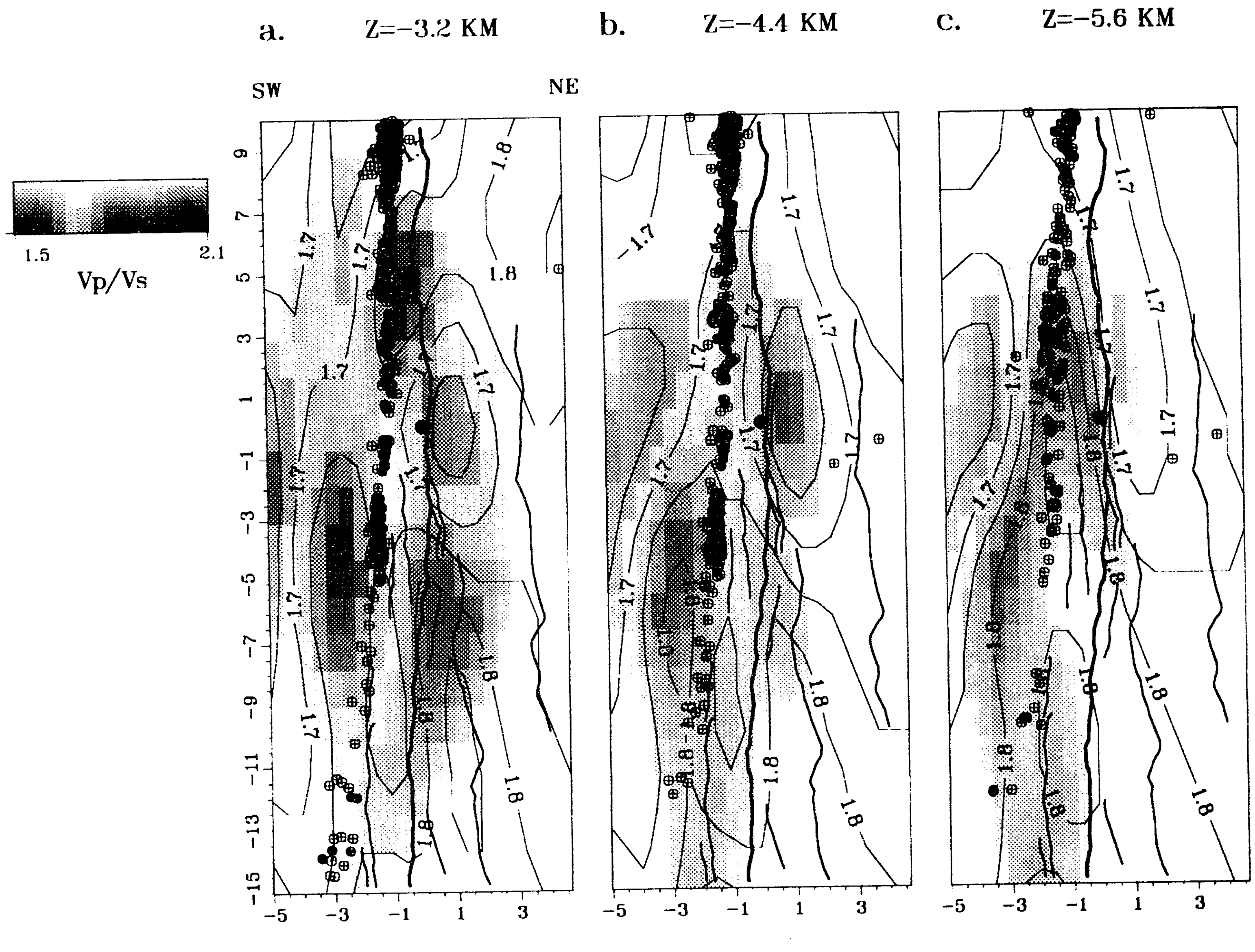

Figure 5.11a,b,c

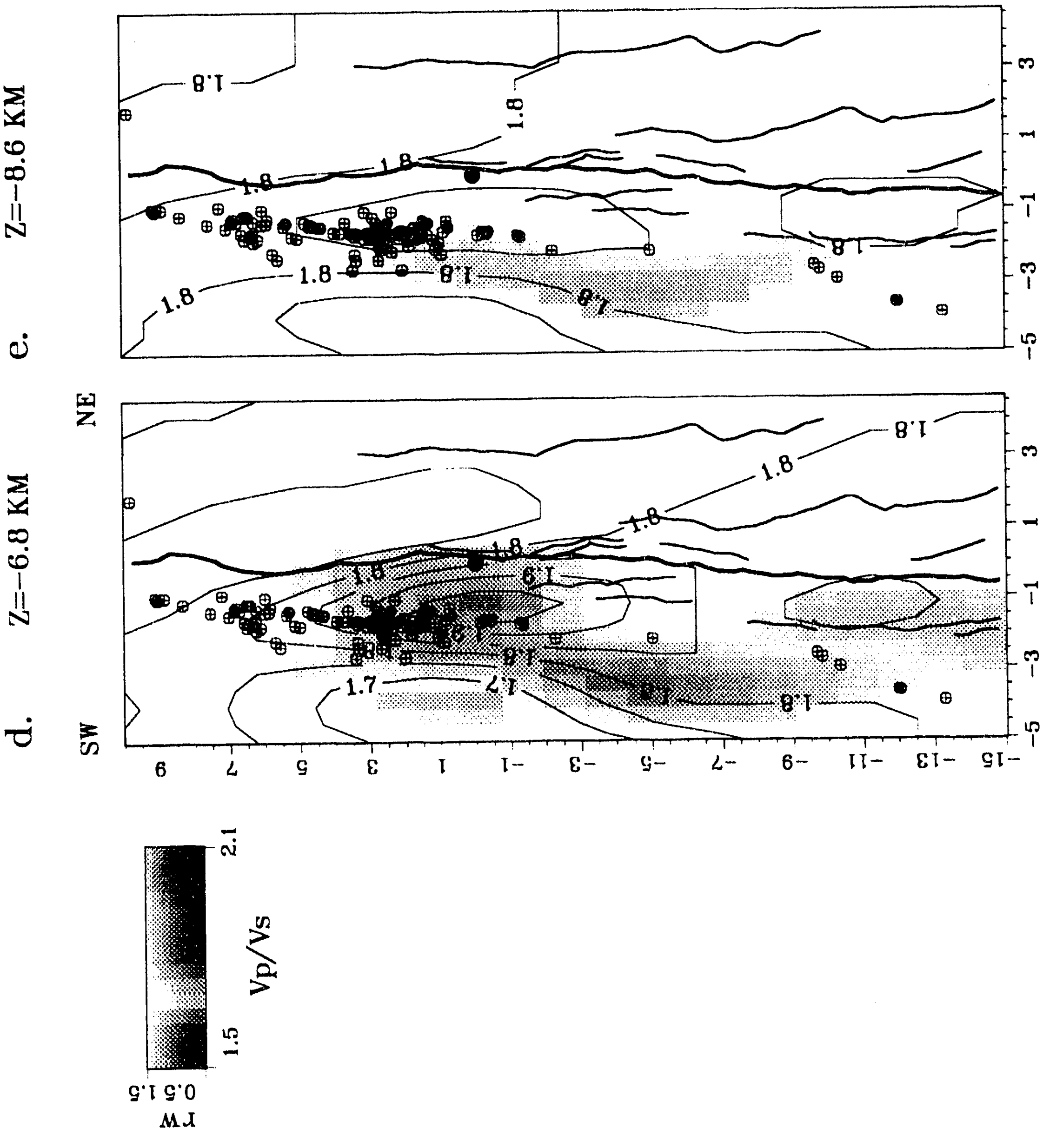

Figure 5.11d,e

Figure 5.12: Across-strike (SW-NE) sections through Parkfield 3-D V_p/V_smodel. Contour interval 0.05. See fig. 5.5 for explanation of seismicity..

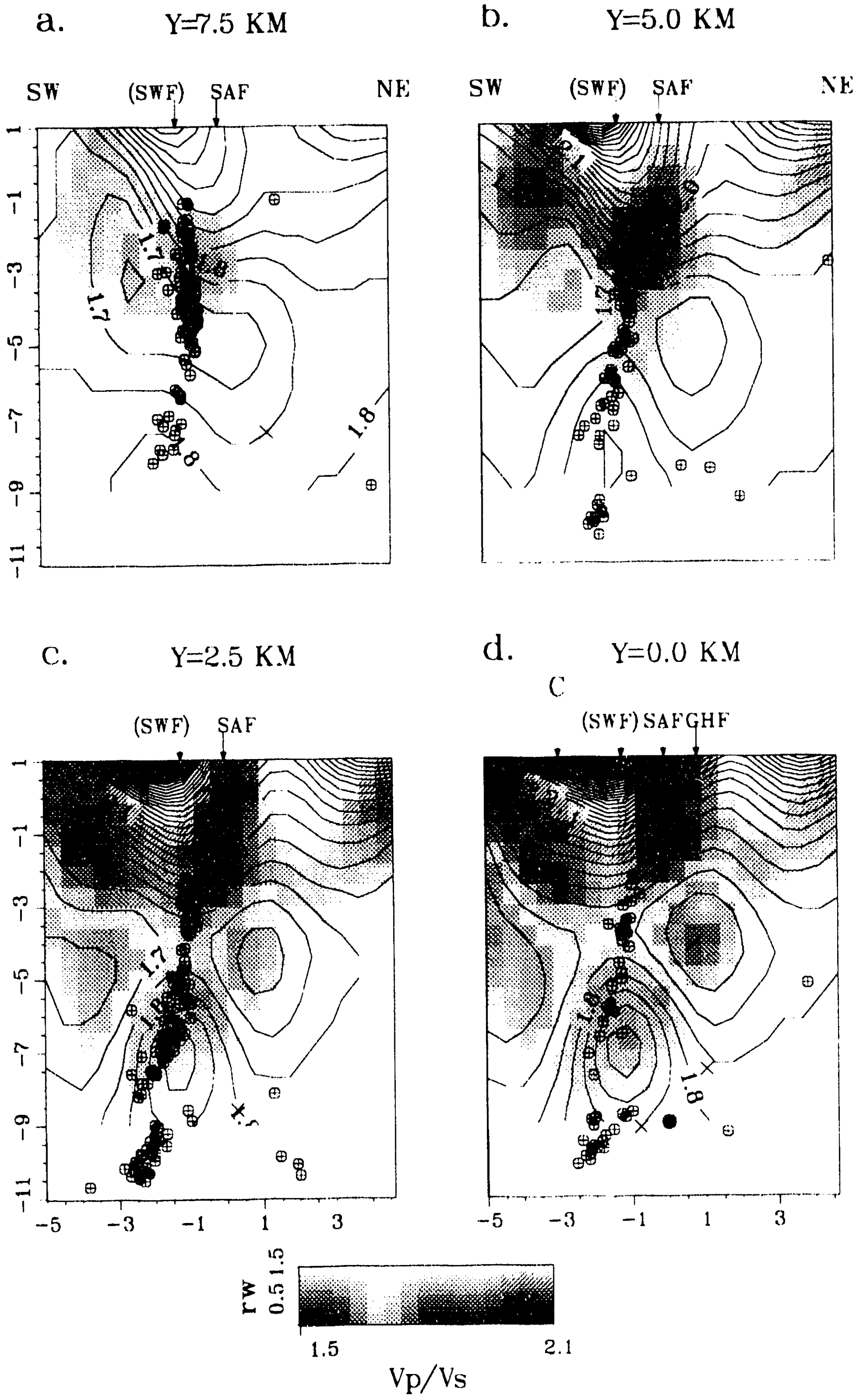

Figure 5.12a,b,c,d

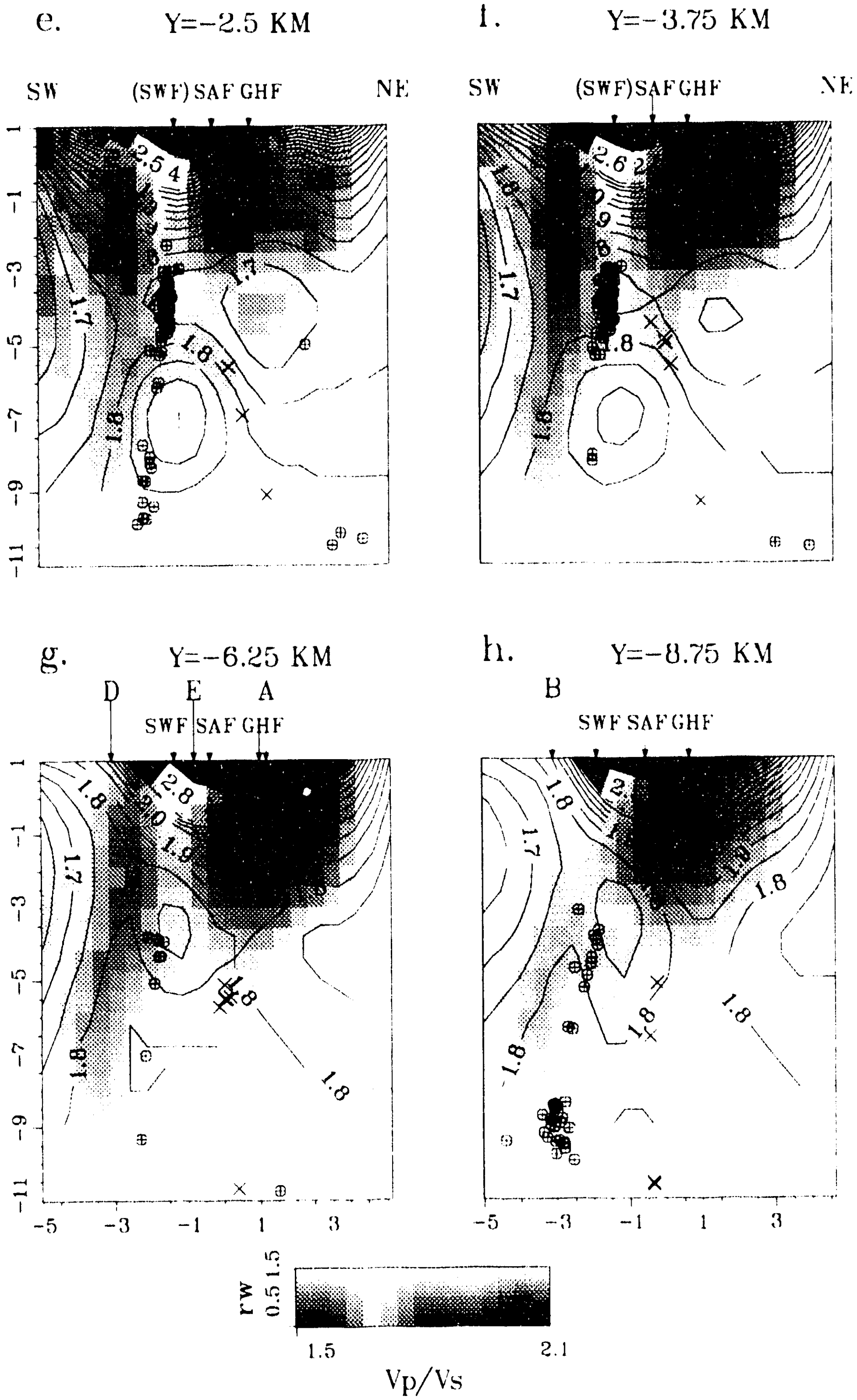

Figure 5.12e,f,g,h

Figure 5.13: Along-strike (SE-NW) sections through Parkfield 3-D V_p/V_s model. Contour interval 0.05. See fig. 5.5 for explanation of seismicity.

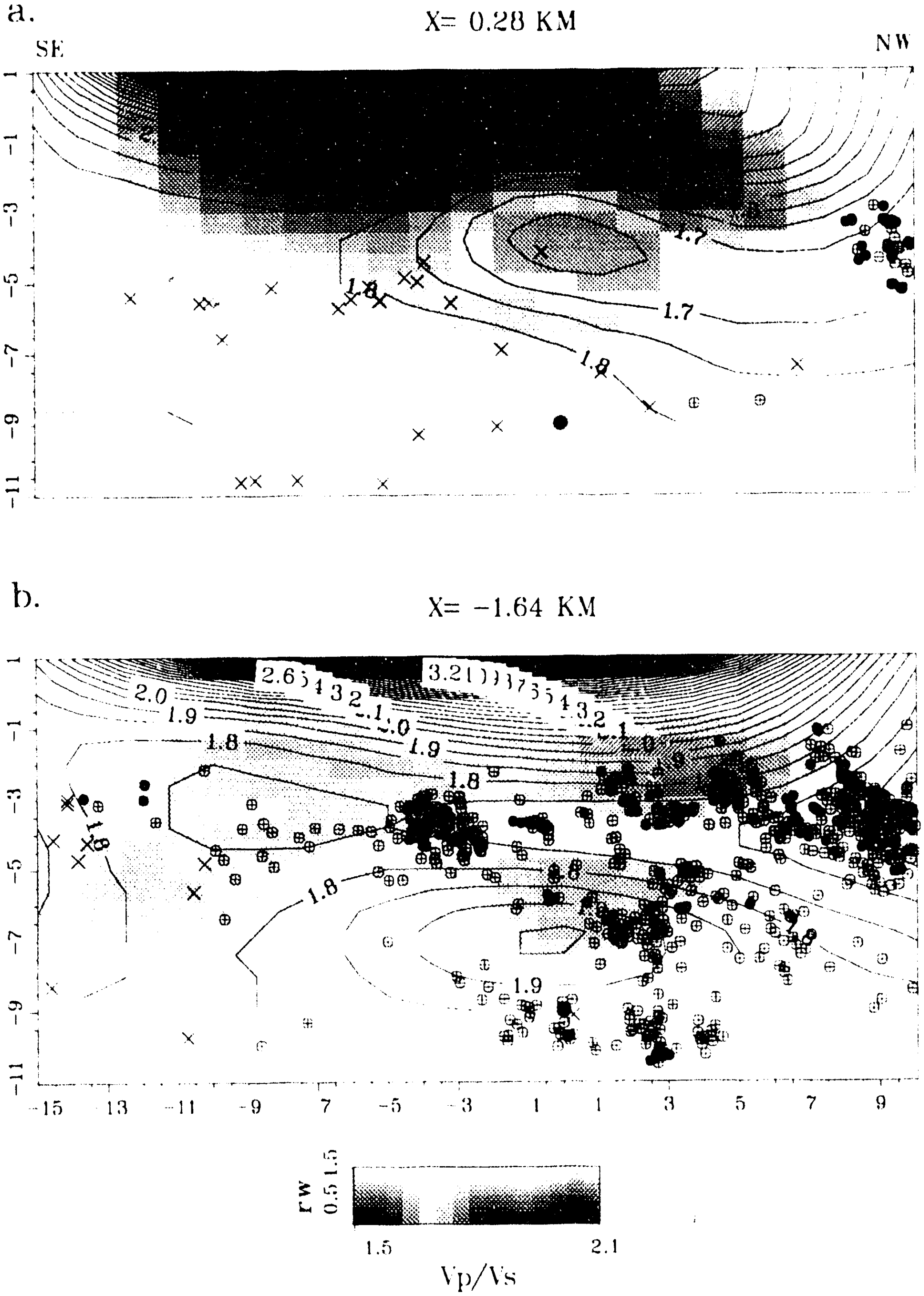

Figure 5.13a,b

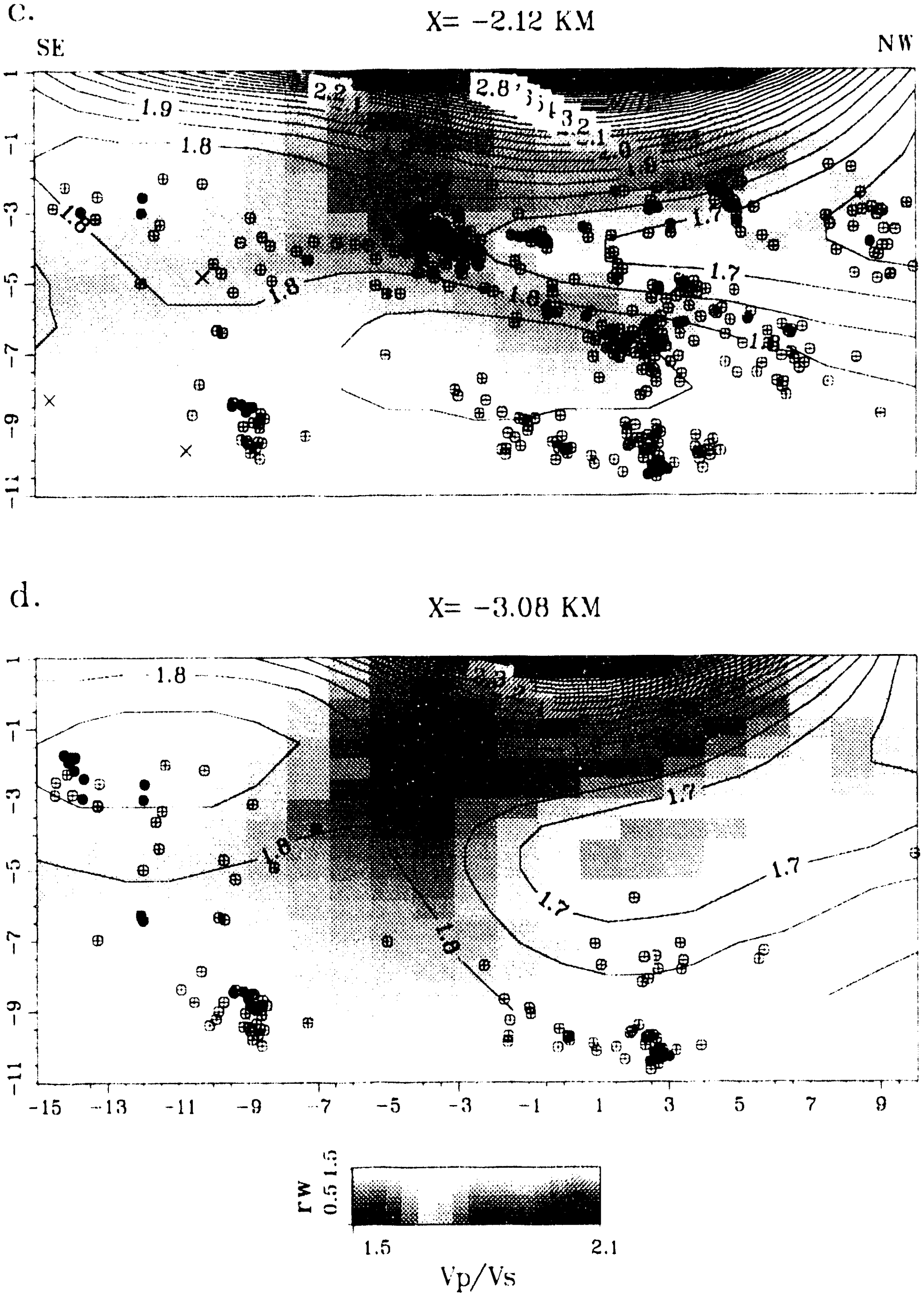

Figure 5.13c,d

of the shallow high-velocity body is similar to that provided by V_p, but the gradient bounding the NE side of this anomaly is considerably steeper. This is a result of the S velocities within the adjacent Franciscan formation being relatively lower than the P velocities. The deep high-velocity body is defined by velocities that reach 3.6 km/s, but the definition is poor because of the limited resolution of the model.

The most prominent feature of the V_p/V_s model is the thick layer of very high V_p/V_s in the shallow subsurface. Towards the center of the model, these high V_p/V_s values are well resolved, and have been confirmed by a high-resolution tomographic inversion at the Varian well (Daley and McEvilly, 1992. Deeper in the section, a localized V_p/V_s low (1.65-1.7) is resolved in the depth range 3.5-7 km (z=-2.5 to -6) within the Franciscan formation between y=9 and y=-2.5 (figs. 5.11a-e, 5.13a). A similar anomaly, although less intense, is resolved on the SW side of the SAF between y=9 and y=0 (figs. 5.13c,d). At the NW end of the model volume this anomaly is centered between the SAF and the shallow high-velocity body at a depth of 4.5 km (z=-3.5). Towards the SE it moves deeper and towards the SW, under the lenticular section of the shallow high-velocity body defined in the V_p model. The V_p/V_s low on both sides of the SAF result from relatively high S velocities (fig. 5.8a).

A very intense, narrow V_p/V_s high (2.0) is resolved centered at y=0 and a depth of 8 km (z=-7). The anomaly results from low S velocities that extend from well into the Franciscan formation to the fault plane defined by the seismicity. This lobe of low V_s develops suddenly at about y=4 and disappears equally abruptly at y=-3 (figs. 5.9e and f). The P velocity field remains virtually unperturbed within the volume occupied by this lobe of low V_s. The V_p/V_s high is well-resolved above z=-8.5 between y=3 and -3 but resolution is lost below z=-7 at each end. The positive V_p/V_s anomaly is drawn on the interpretive panel of Figure 3.16b, which shows that it is truncated by the deep high -velocity body defined in the V_p model. Outside the V_p/V_s high the immediate fault zone below 6 km depth has normal values for quartzo-feldspathic crust (see below), in the range 1.7-1.75.

The symmetry apparent in Figures 5.11c and 5.12c and d in the pattern of alternating negative and positive V_p/V_s anomalies raises the possibility of long-wavelength oscillation in the V_p/V_s model. Long wavelength oscillations were observed in some of the fault model tests of Michelini (1991), but V_p/V_s conditioning (Section 3.2) was shown to be effective in minimizing these. Since the synthetic tests were based upon the actual Parkfield source-receiver geometry, it seems unlikely that the true inversion would be so unstable as to produce long-wavelength artifacts in the well-resolved central part of the model volume having amplitudes as large as the observed V_p/V_s anomalies. However, the possibility of oscillations in the V_p/V_s model cannot be discounted, and increases the uncertainty of the interpretation of the prominent V_p/V_s anomalies.

There is no anomaly in the V_p/V_s model corresponding to the shallow high P-velocity body, V_p/V_s values in this part of the model being in the range 1.750-1.8. No prominent V_p/V_s anomaly is associated with the deep high P-velocity body. On Figure 5.12g a relatively high V_p/V_s, in the range 1.8-1.85 is resolved in a small area located at the center of the deep high-velocity body, and the shape of the $V_p/V_s = 1.8$ contour here mimics the domed top of the high-velocity body. Outside of the intense anomalies described above, well-resolved V_p/V_s values are generally about 1.75. Therefore the values associated with the high-velocity body are significantly higher than the surrounding Franciscan and granitic crust.

5.3.1 Lithological Constraints from the V_p/V_s Model

Major changes in lithological composition can be accompanied by variations in V_p/V_s ratio but are generally observed not to occur without significant changes in both the P and S velocities themselves. Therefore, it is assumed that only the anomalies in the Parkfield V_p/V_s model that are associated with the features identified in the V_p model relate to lithological composition, while the remaining V_p/V_s anomalies are caused by other factors. Specifically, the intense V_p/V_s high centered within the fault zone and the two shallow V_p/V_s lows on either side of the SAF are assumed not to be related to lithological composition, and are dealt with in the Section 5.5.5 below. In this section I discuss the relatively high V_p/V_s values that apparently characterize the deep high P-velocity body, although the evidence for these values discussed above is weak.

The constraints on the composition of the deep high-velocity body are a P-velocity of 6.6 km/s at 7-8 km depth (pressure 0.1-0.2 GPa) and a V_p/V_s ratio in the range 1.8-1.85. One candidate lithology for this body is the quartz-hornblende gabbro of Logan/Gold Hill, as discussed in Section 4.2.4. The theoretical P- and S- velocities for the composition of these gabbro bodies at 0.1 GPa estimated from Figure 4.8 (as described in Section 4.2.4) are 6.74 km/s and 3.69 km/s, respectively, which give a V_p/V_s ratio of 1.83. Therefore, the observed V_p and V_p/V_s values at Parkfield are consistent with the composition of the Gold Hill gabbro, although the P-velocity is a little low.

In general, the systematics of velocity variations in basic rocks are controlled by the proportions of hornblende (V_p=7.0, V_p/V_s=1.74) and plagioclase (V_p=6.7, V_p/V_s=2.02) (see Christensen and Salisbury, 1975, fig. 15). Therefore, relatively high V_p/V_s ratios are expected to accompany relatively low P-velocities towards the anorthosite end of the series, and *vica versa* moving towards the hornblende end. Christensen (1978) remarks that the relatively low V_p *and* V_p/V_s values that characterize metagabbros from the Point Sal ophiolite (e.g. sample MG2, fig. 5.7), compared with unaltered gabbros (e.g. sample GB5), are due to the significant (8%) quartz content of these rocks. Therefore, the particular relationship between V_p and V_p/V_s endowed by the unusual quartz content of the Gold Hill gabbro, and the fact that this unusual rock type outcrops close by, tends to favor the same quartz-hornblende composition for the deep rock mass. However, it is conceivable that the velocities of the deep anomaly at Parkfield could be accounted for by metamorphosed basic rocks of a range of compositions. These might include andesite and dacite, which raises the possibility that the deep and shallow high-velocity bodies SE of y=0 are expressions of the same volcanic rock mass, which outcrops as the Lang Canyon volcanics. As noted above, no data on the velocities of andesites and dacites appear to exist at present.

Ultramafic rocks of the types belonging to the Coast Range ophiolite are also possible lithologies for the deep high velocity bodies at Parkfield and Loma Prieta. The velocity systematics of ultramafic rocks depend on the proportions of pyroxene (V_p=7.9, V_p/V_s=1.7-1.73), olivine (V=8.5, V_p/V_s=1.8) and serpentine (V_p=5.1, V_p/V_{ss}=2.2 for chrysotile) (all velocity values are at 0.1 GPa and are taken from Christensen and Salisbury [1975]). In particular, V_p/V_s for ultramafic rocks is controlled almost exclusively by the degree of serpentinization. A $V_p$value of 6.6 km/s such as that of the deep high-velocity body at Parkfield indicates a relatively high degree of serpentinization (greater than 30%), based both upon compositional analysis (Christensen and Salisbury, 1975, fig. 15) and on laboratory measurements of partially-serpentinized peridotite samples from the California Coast Ranges (Christensen, 1966a, 1978). For this amount of serpentine a relatively high value of V_p/V_s, in the range 1.87-1.9, is expected, which is substantially above the apparent value for the Parkfield deep high-velocity body. However, individual laboratory samples deviate significantly from the average values, and an ultramafic composition for the deep high velocity bodies cannot be ruled out. Granitic gneisses of the type that outcrop within the Salinian block SW of the SAF generally have V_p/V_s ratios in the granite range (1.7-1.8) (Christensen, 1965, 1966b). Other types can have higher values depending on their protoliths and metamorphic grades (Kern and Richter, 1981).

5.3.2 Summary of Lithological Interpretation

The Parkfield three-dimensional P-velocity model images an anomalous high-velocity body at depths as shallow as 5-6 km below the surface on both sides of the SAF trace that is similar in form to the high-velocity body seen in the Loma Prieta model. As at Loma Prieta, the full depth extent of the body is not resolved by the Parkfield model. Therefore, the possible interpretations (Section 4.2.3) of the high-velocity body as either an up-thrust block of sub-basement, as two rootless rock masses that have been brought into juxtaposition by lateral displacement along the San Andreas system, or as a rootless rock mass brought into juxtaposition against an up-thrust block apply equally to Parkfield. While the additional constraint on candidate lithologies supplied by the Parkfield V_p/V_s model is scant, it does indicate that the Parkfield high velocity body has neither extremely high nor extremely low V_p/V_s, but a value that is moderately higher than that expected for granitic or Franciscan crust. The observed value of 1.8-1.85 is consistent with the unusual hornblende-quartz composition of the Gold Hill gabbro body. This strengthens the possible interpretation that Gold Hill is a small outcrop of a relatively large buried gabbro body, which is suggested by the tenuous connection of the high-velocity body at shallow depths to the poorly resolved ridge of high velocity on the NE side of the SAF that appears to be a subsurface extension of the Gold Hill outcrop. The Parkfield velocity models, however, are not adequate to rule out the other possible ultramafic or metamorphic compositions discussed in Section 4.2.3. A shallower high velocity body is also imaged on the SW side of the SAF that is coincident with outcrops of the Lang Canyon volcanic rocks.

The Parkfield high-velocity body appears have the same kind of influence in determining the transition from stable slip to unstable rupture as that at Loma Prieta, although at the lesser scale concomitant with its smaller size.

5.4 Relationship of Seismicity to Lithology and V_p/V_s Anomalies

The interpretive panels on Figures 5.4-5.6 show the major lithological contacts interpreted from the V_p model. Fault contacts are inferred from hypocentral alignments.. Figures 5.4 and 5.6 also show the positive V_p/V_s anomaly. Focal mechanism solutions are not computed for the earthquakes recorded by the HRSN, owing to the limited azimuthal coverage of the network. I rely instead on the high-quality representative solutions presented by Nishioka and Michael (1990) as part of their detailed study of Parkfield seismicity as recorded by the USGS CALNET.

5.4.1 Earthquakes Northwest of Middle Mountain

From y=10 to y=0 two distinct seismicity trends are defined. The first consists of intense seismicity above a depth of 6.5 km (z=-5.5), which defines a near-vertical or steep NE-dipping plane. The second consists of events below 6.5 km depth, which define a plane that dips approximately 80° SW and that projects to the surface at the SAF trace. This second plane, which conforms to a break in slope of the velocity contours, is identified as the active SAF plane. Therefore, the intense shallow microseismicity is occurring on a secondary fault which intersects the main SAF plane at a depth of 6.5 km (z=-5.5), the point of intersection moving progressively upwards to 4.5 km (z=-3.5) at y=1 km. The plane defined by the shallow seismicity intersects the surface at a location that coincides with the projected trend of the SW *en echelon* segment of the SWFZ (fig. 5.2). As discussed in Section 5.2.2, Sims (1989, 1990) suggests that this fault segment continues to the NW beneath the surficial sediments. Further to the SE, between y=-3.5 and y=-5 km, the intense microseismicity above a depth of 5.5 km (z> -4.5) also appears to define a near-vertical plane oblique to the SW-dipping SAF plane. At y=-5 km the shallow seismicity trend again intersects the surface along the projected strike of the SW *en echelon* segment of the SWFZ, rather than at the trace of its NE *en echelon* segment that is mapped in this vicinity. The upper limit of the seismicity conforms closely to the 4.6 km/s contour, in approximate agreement with the sediment/Franciscan contact. The shallow seismicity is also confined below the near-surface band of very high V_p/V_s ratios (fig. 5.13).

Between the NW edge of the model volume and y=7.5 most of the shallow seismicity is confined below the sediment/Salinian contact. Southeast of y=7.5, however, the 5.3 km/s contour defining the top of the Salinian basement becomes depressed towards the fault so that the granitic SW wall rock at the fault is replaced by the rocks at the base of the overlying sediments (or perhaps by highly fractured granite). By y=5 km, the shallow activity is entirely confined above the sediment/Salinian contact. The nature of the material in the wedge between the SAF and the secondary fault cannot be resolved by the model. Franciscan rocks are at the SAF at the surface NW of y=7 km (fig. 5.3). Dibblee (1980) maps an outcrop of Franciscan rocks SW of the main SAF trace between y=6 and 9 km. This block is mapped as being fault-bounded on its SW side, but the map scale is too small to assess the possible relationship of the mapped fault to the NE-dipping plane of seismicity.

The two regions of relatively low V_p/V_s flank the zone of intense shallow microseismicity on either side between y=10 and y=1 km. The two low V_p/V_s regions are at their closest approach to each other where the NE-dipping plane intersects the SAF, forming a band of slightly lower than average V_p/V_s there. In longitudinal section (fig. 5.13b), the shallow seismicity appears as a funnel-shaped band which mimics the broadening of the zone of low to normal V_p/V_s towards the NW. The most intense concentration of shallow seismicity occurs at the narrow end of this funnel at y=-4. Therefore, it appears that the shallow creep-related seismicity occurs where the V_p/V_s ratio is low to normal within the fault zone. Fault-plane solutions for all of these events indicate right-lateral strike-slip on a plane striking parallel to the SAF (Nishioka and Michael, 1990).

Seismicity on the main SAF plane below its intersection with the shallow secondary plane is sparse at the NW end of the model volume but suddenly intensifies at y=3, appearing as a sharply defined "tube" of earthquakes between y=3 and y=2 km (figs 5.4e, 5.6b and c). Between y=5 and y=1 km sub-trends of events that dip relatively gently SW from the steeply-dipping SAF plane are clearly defined (fig. 5.5), and are particularly evident in the detached groups of earthquakes below 10 km depth (z=-9). Nishioka and Michael (1990) also comment of the broadening of the zone of seismicity here. These trends indicate small-scale faulting auxiliary to the SAF. The complexity in the seismicity disappears abruptly at y=0, where the SAF plane becomes sharply defined. At this point activity on the shallow secondary fault ceases and the surface creep rate begins its steep descent.

5.4.2 Earthquakes Southeast of Middle Mountain

On the V_p/V_s model sections shown in Figures 5.11d and 5.13b, the seismicity is seen to be cut off at y=0.5 km in the depth range 7.5-9.5 km (z=-6.5 to 8.5) where the fault plane enters the core of the zone of high V_p/V_s . Relatively intense seismicity continues to the SE both above and below the V_p/V_s high. Returning now to the V_p model in Figures 5.4e and 5.6b and c, the isolated seismicity below 10 km (z=-9) is abruptly terminated at y=-2 by the NW end of the deep high-velocity body. At depths shallower than 6 km (z> -5) the situation is not so clear, but the few shallow events that occur SE of y=-5 are located only above the top of the high-velocity body. The main belt of shallow seismicity ends with the intense concentration of events centered at y=-3.5 If the shallow high-velocity body extends to depth as suggested in Figure 5.5f, then it is at the fault at about 6 km depth and may be related to the termination of the shallow seismicity. However, this relationship is not clear because of the uncertain depth extent of the shallow high-velocity body. Southeast of this point the seismicity is sparse at all depths, but until y=-9 km it continues to conform to the steep SW-dipping plane defined to the NW. At y=-9, the creep rate levels off again and the shallow seismicity becomes more diffuse. The cluster of events within the deep high-velocity body mostly consist of the M_L3.7 earthquake of May, 1989 and its aftershocks.

5.4.3 Microearthquake Clusters

About 50% of the earthquakes recorded by the HRSN during the period 1987-1991 define tight spatial clusters containing (to date) from two to as many as 16 events (Foxall and McEvilly, 1987, 1988; Antolik et al., 1991). The clusters are defined based upon the close similarity of the seismograms recorded from their member earthquakes on the broad-bandwidth (2-125 Hz) HRSN. P-wave trains commonly have coherency's greater than 0.98 to 75 Hz and S-waves to 50 Hz. This requires that the earthquakes within a cluster occur within a few tens of meters of each other and have essentially identical mechanisms.

Very high resolution locations of the cluster members relative to each other are determined by using a cross-correlation/cross-spectrum technique to compute the time delays of P and S arrivals of the events relative to a chosen reference event in each cluster (Foxall and McEvilly, 1988). This permits sub-sample (i.e. less than 2 ms) timing of the relative arrivals and relative hypocenter locations accurate to within a few tens of meters to be computed. The characteristic dimension of the fault patch occupied by a cluster is 100-200 m. Therefore, each cluster represents the repeated rupture of a precisely-defined patch of the fault - a fine-scale characteristic earthquake. The repeat times of the earthquakes in each cluster can range from seconds to (to date) several years.

The locations of clustered earthquakes are shown as filled circles on the velocity model sections. They comprise a large proportion of shallow creep-related events above 6.5 km depth, including the dense concentration centered on (y,z)=(-3.5, -4). The group of earthquakes that mark the termination of seismicity at the NW end of the high V_p/V_s zone are clustered but events to the NW within the same depth range are not. Two clusters are defined in the seismicity deeper than 11 km at y=3, and the aftershock sequence within the high-velocity body at y=-9 is composed of similar events.

5.4.4 Long-Term Seismicity Patterns

The seismicity described above closely conforms to the long-term pattern of seismicity at Parkfield since 1970 described by Bakun and Lindh (1985) and Poley et al. (1987). Salient features of the long term seismicity are shown in Figure 5.14. The higher resolution of the HRSN data located using the three-dimensional model compared with the CALNET locations is reflected in tighter spatial clustering of the seismicity. Most of the larger earthquakes ($M \geq 3$) that have occurred within the model volume since 1970 are located NW of Middle Mountain on the main SAF plane below 6.5 km depth. The largest earthquake (M4.8 in 1975) on the Parkfield section of the fault since 1966 was located at y=6 km at 11 km depth, and an M4.4 event occurred under the 1966 mainshock hypocenter at a depth of 11 km in 1981. Several events located within the "tube" of seismicity between y=2 and y=3 km had magnitudes greater than 3, including an M4 event in 1982.

The group of earthquakes that mark the termination of deep seismicity at the NW end of the deep high-velocity body (y,z=-1.5, -9.5) includes a sequence of $M > 3$ events that recur every 39-40 months (Poley et al., 1987). The stress drops of these earthquakes reported by O'Neill (1984) are relatively high (> 20 bar) compared with the other larger events located NW of Middle Mountain. Between Middle Mountain and Gold Hill, the few larger events have generally occurred near the upper and lower peripheries of the deep high-velocity body.

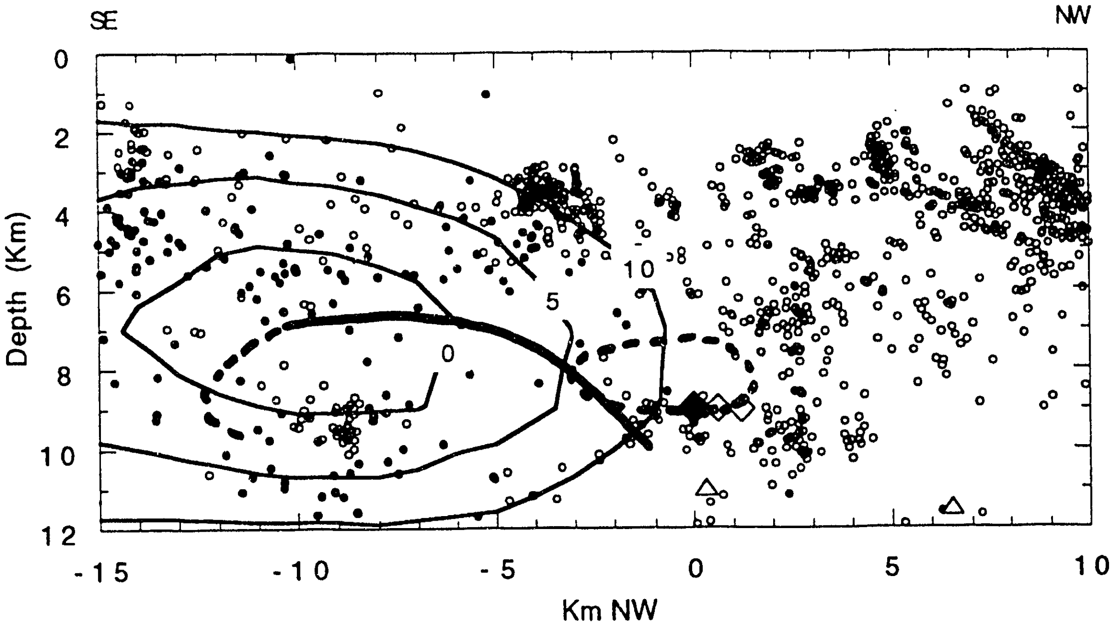

Figure 5.14: Summary along-strike (SE-NW) section through 1966 Parkfield earthquake rupture zone showing: Slip contours in mm/yr from Harris and Segall (1987); 1966 mainshock (solid diamond), aftershocks from Eaton et al. (1970) (filled circles), and foreshocks (open diamonds); M≥4 earthquakes since 1966 (triangles) and background seismicity (open circles). Boundaries of high-velocity body (thick solid and dashed curve) and positive V_p/V_S anomaly (dashed ellipse) are from figs. 5.6 and 5.13, respectively.

5.5 Lithology-Based Model for Parkfield

I begin this section with a brief review of some of the data and models that are available for the 1966 Parkfield earthquake. Salient features of the 1966 earthquake are plotted on Figure 5.14 so that they can be integrated with the lithological and seismicity data to develop a slip stability and earthquake nucleation model for Parkfield. Development of the model in terms of the concepts of fault strength and stability discussed in Chapter 2 parallels that for Loma Prieta presented in Section 4.5.

5.5.1 The 1966 Parkfield Earthquake

The June 28, 1966 M_L5.5 Parkfield earthquake nucleated under Middle Mountain and ruptured unilaterally towards the SE (McEvilly et al., 1967; Filson and McEvilly, 1967). The dense aftershock zone extended from Middle Mountain a distance of about 30 km to Highway 46 near Cholame (McEvilly et al., 1967; Eaton et al., 1970), indicating that the SAF plane between Middle Mountain and Highway 46 ruptured during the earthquake. Surface fracturing extended over about the same distance (Brown et al., 1967; Brown, 1970). However, aftershocks that occurred within the first 13 minutes after the mainshock extended only 20 km to the 1-2 km offset in the SAF trace SE of Gold Hill (fig. 5.1) (McEvilly et al., 1967), which suggests that the primary mainshock rupture was arrested at the offset and subsequently broke through this barrier to continue to rupture the plane between Gold Hill and Highway 46.

The mainshock was preceded by two strong foreshocks, the largest of which was an M5.1 event that occurred 17 minutes before the mainshock (McEvilly et al., 1967). Based upon the differences between arrival times at seismographs at Gold Hill and Priest (25 km NW of Middle Mountain), the mainshock and foreshocks occurred within 1.5 km of each other along strike, and the mainshock is within 2 km of y=0 in our model coordinates (McEvilly and others, 1967; Lindh and Boore, 1981). The mainshock focal depth was estimated as approximately 9 km (A. Lindh, unpublished) but is not well constrained. The foreshocks locate immediately to the NW of the mainshock (fig. 5.14) and apparently ruptured unilaterally to the NW (Filson and McEvilly, 1967; Bakun and McEvilly, 1979). Bakun and McEvilly (1981) estimated that the stress drops of the M5.1 foreshock and a similar foreshock that immediately preceded the 1934 Parkfield earthquake were higher than those of foreshocks and "background" earthquakes located further to the NW, in agreement with the results of O'Neill (1984). Bakun and McEvilly (1979) pointed out the similarity between the ground motion recorded from the 1966 earthquake to that from the 1934 earthquake that occurred in the same vicinity, and the similarities in the foreshocks and surface rupture of the two earthquakes. They later found that the 1922 Parkfield earthquake was also similar (Bakun and McEvilly, 1984), which led to their proposal that the 1966 earthquake was the latest in a quasi-periodic series of characteristic M5.5-6 earthquakes which rupture the Parkfield segment of the SAF.

The aftershocks shown in Figure 5.14 are the subset of the hypocenter locations of Eaton et al. (1970) that have depths constrained by arrival time data. Seismograph coverage of the aftershock zone NW of Gold Hill was sparse (Eaton et al., 1970) so relatively few aftershocks were recorded by a sufficient number of stations to compute a reliable hypocenter location, and the locations in this area are of a generally lower quality than those further SE. The aftershock locations shown in the velocity model sections are a subset of the events shown in Figure 5.14 that were recorded by temporary stations deployed NE of Gold Hill for short periods during July and September, 1966 (Eaton et al., 1970). I attempted to relocate the aftershocks that occurred within the velocity model volume using the USGS arrival times and the three-dimensional V_p model. However, the data are inadequate to locate reliably all but a few of the aftershocks that occurred there. I located a set of the best-recorded events for comparison with the original locations of Eaton et al. (1970). The three-dimensional locations are systematically located on average about 1-2 km SW and 2-5 km shallower than the USGS locations.

Several models of the 1966 rupture (e.g. Aki, 1968; Anderson, 1974; Levy and Mal, 1976; Archuleta and Day, 1980) have been presented. Most of the models assume that the primary rupture extended from Middle Mountain to Highway 46 and adopt a single, 30 km-long dislocation plane based upon the aftershock distribution of Eaton et al. (1970). Trifunac and Udwadia (1974) accounted for the offset in the SAF trace SE of Gold Hill by modeling the fault plane as two segments with a change in strike at Gold Hill. The results of this more realistic model indicate a peak displacement of approximately 2 m at about $y=-11$ km in the velocity model coordinate system, and imply that the primary mainshock rupture extended as far as the Gold Hill offset. Their results also suggest that the fault did not rupture to the NW of the mainshock hypocenter.

The case for primary rupture being arrested at the Gold Hill offset was argued persuasively by Lindh and Boore (1981). They propose that the Parkfield earthquakes nucleate at an asperity which they identify as a 5° bend in the fault trace at Middle Mountain and primary rupture is arrested at the barrier formed by the Gold Hill offset. The bend at Middle Mountain is very subtle, and, based upon detailed mapping of the SAF trace by Brown (1970), could be as small as 2°. Although Lindh and Boore state only that the bend might correspond to a discontinuity at depth, subsequent studies have adopted it as a type example of geometrical control of rupture nucleation. The scale of this proposed geometrical asperity is certainly nowhere near that of the Gold Hill offset or of the fault bends near Lake Elsman and Hecker Pass along the Loma Prieta section of the fault.

Harris and Segall (1987) computed the slip distribution along the Parkfield segment by inverting trilateration and surface creep data. Their dislocation model assumes only a planar vertical fault from the surface to a specified transition depth beneath which the fault slips freely, bounded laterally by a locked (1857) segment beginning at Cholame and a freely-slipping segment to the NW. The model is constrained *a priori* to be smooth. The inversion resolves a zone of low to zero slip that extends from about 2 km depth to the transition depth and from Middle Mountain to Cholame. The core of the locked segment is confined to the fault plane NW of Gold Hill. Long wavelength (6-10 km) characteristics of the horizontal distribution of slip are resolved but the depth extent of the locked plane is poorly constrained by the data. The locked zone agrees closely with the 1966 aftershock zone, and is reproduced in Figure 5.14.

5.5.2 Fault Slip Northwest of Middle Mountain

The thick section of the Great Valley sequence sediments does not overlie the Franciscan formation at Parkfield as it does SE of Loma Prieta. The creep-related microseismicity at shallow depths on the Great Valley/Salinian contact SE of Pajaro Gap is replaced by intense seismicity on the shallow secondary fault NW of Middle Mountain. This takes place first at the Salinian/Franciscan contact above 6.5 km, and then at a contact between the Tertiary sediments overlying the Salinian and, possibly, the Franciscan. The Parkfield model does not extend far enough to the NW to ascertain what the shallow slip behavior is where the secondary fault is not present, but the northwestern-most cross-sections through the model suggest that intense microseismicity continues at depths above 6.5-7 km on the main Salinian/Franciscan contact.

The coincidence of the shallow secondary fault with the projected trace of the SW *en echelon* segment of the SWFZ 9 km to the SE may be fortuitous, but the apparent alignment of the near-vertical trend in the shallow seismicity with the projected strike of the SWFZ at y=-5 km, closer to the NW end of the mapped trace, lends some credence to this hypothesis. Surface displacement was observed on this fault after the 1966 earthquake (Brown et al., 1967), although no aftershocks were located on it (Eaton et al., 1970). As discussed in Section 5.2.2, Sims suggests that the SE segment of the SWFZ continues to the NW. Sims (1989) also proposes that the SWFZ was the active trace of the SAF system NW of the Gold Hill offset until 6 Ma. Therefore, it is possible that shallow slip NW of Middle Mountain and above the high-velocity body is transferred from the main SAF plane in response to the locking of the main plane (discussed below), in a similar way that slip is transferred to the Sargent fault adjacent to Pajaro Gap (see Section 4.4.3).

The low rate of seismicity on the Salinian/Franciscan SAF contact below a depth of 6.5 km at the northwestern end of the Parkfield model appears similar to that SE of Pajaro Gap on the Loma Prieta cross-sections. However, seismicity on the Parkfield section extends as far as 11 km depth, and the long-term data discussed above indicate that earthquakes as large as M5 occur on this deep fault contact at least as far as 7 km NW of Middle Mountain. Seismicity between San Juan Bautista and Pajaro Gap is strictly confined above 9 km depth until it abruptly deepens at the SE end of the high velocity body, and slip below that depth appears to be entirely aseismic (although the earthquakes between depths of 7 and 9 km there may be occurring on the Salinian/Franciscan contact). If it is assumed that the intrinsic strength and stability properties of the Salinian/Franciscan contact remain the same, the difference in behavior is attributed to differences in the detailed response of the otherwise stable contact to arrest of slip at the two locations. The Parkfield V_p/V_s model is not resolved at depths below 7 km at the NW end of the model so the possible role of pore fluids in the slip behavior of the deeper fault plane cannot be assessed. The Franciscan formation outcrops at the fault NW of y=7 km. Therefore, the Coast Range ophiolite with its serpentinite is not present at seismogenic depths as it is SE of Pajaro gap.

5.5.3 The Middle Mountain Barrier

I propose that the fundamental barrier to stable sliding at Parkfield is the deep high-velocity body. This is based on the abrupt termination of deep microearthquakes where the fault plane enters the high-velocity body at y=-2 km, and, with the notable exception of the clustered events near y=-9 km, the absence of earthquakes within the body itself. Therefore, the high-velocity body arrests stable sliding at depths below 6.5 km and, as indicated by the surface creep data, inhibits stable sliding at shallower depths. The zone of high V_p/V_s also may play a significant role but, as I explain in the Section 5.5.5, it formed as a response to the lithological barrier.

5.5.4 The Parkfield Asperity Model

As at Loma Prieta, the asperity imaged as the high velocity body at Parkfield is a part of the fault zone of fixed dimensions that has permanently high fracture strength (σ_y) and unstable slip properties (a Type 3 fault contact). The high-velocity body encompasses the lower, northwestern part of the region of low to zero slip of the Harris and Segall (1987) model (fig. 5.14). I will discuss the dynamic rupture of this asperity during the Parkfield earthquakes in terms of the elliptical asperity model of Das and Kostrov (1985) (Section 4.5).

The nucleation zone of the Parkfield asperity is identified as the point of termination of the deep seismicity at y=1.5-2 km at about 10 km depth. The high stress drops of the events in this small region and of the immediate foreshock of the 1966 earthquake suggest that the nucleation zone is just within the high-strength asperity close to its deep northwestern edge. The position of this zone is well within the error bounds of the hypocentral location estimates of the 1966 earthquake and its foreshocks. Therefore, I propose that the 1966 rupture nucleated at the highly stressed northwestern end of the major axis of the roughly elliptical asperity, in accordance with the theoretical asperity model.

The aftershocks distribution shown in Figure 5.14 suggest that the mainshock rupture propagated through the entire width of the high-velocity body to the SE of the nucleation point, because, in contrast to the background seismicity, they extend through the high-velocity body. Note, however, that the best-constrained aftershocks, which are shown in Figures 5.5 and 5.6, are mostly located outside of the high-velocity body. This may indicate that the fault plane within the asperity ruptured essentially completely during the mainshock (see Section 4.3.2). The zone of maximum displacement in the rupture model of Trifunac and Udwadia (1974) appears to be close to the SE end of the high-velocity body where, according to the theoretical asperity model, there should be a concentration of stress. This is also the location of the 1989 M3.7 earthquake sequence.

The velocity model does not resolve the southeastern extent of the high-velocity body, so I cannot address the nature of the fault plane to the SE. Assuming that the high-velocity body ends near y=-13 as suggested in Figure 5.6, then dynamic rupture was triggered on the (presumably) Type 2 (conditionally unstable) plane to the SE. The aftershocks also indicate that the rupture overshot on to the partially-locked plane between the high-velocity body and the overlying sediments. There was negligible aftershock activity NW of Middle Mountain, which shows that SAF plane there acted as a relaxation barrier. The driving stress, σ_1, had been reduced to a low level NW of Middle Mountain by the damage process near the barrier (see below), by the larger events that occurred during the inter-seismic period, and finally by the apparently NW-propagating immediate foreshocks.

5.5.5 The Middle Mountain Damage Zone

The effect of the Middle Mountain barrier is first seen as the abrupt increase in the intensity of seismicity on the SAF plane below 6.5 km depth . These microearthquakes are the manifestation of the build up of stress on the deep part of the fault plane immediately in front of the barrier as stable slip is arrested, which results in the formation of a damage zone of intense fracturing. The damage process appears to be fairly well ordered, as indicated by the systematic alignment of the microearthquakes into short yet clearly-defined sub-trends that dip at relatively shallow angles to the SW. The significance of the orientation of these trends is difficult to evaluate without numerical modeling because the local stress field in front of the barrier is highly perturbed. The fault plane solutions of events within this zone computed by Nishioka and Michael (1990) all show a significant normal component of displacement on NW- to NNW-oriented planes, and one solution is pure normal.

The core of the zone of intense damage under Middle Mountain, where the damage process has advanced the furthest, is imaged directly as the high V_p/V_s anomaly there. I propose that this anomaly, and the negative V_p/V_s anomalies on either side of the SAF can be explained in terms of the same mechanisms of rock dilatancy and pore fluid diffusion that form the basis of dilatancy/diffusion models of earthquake nucleation (Nur, 1972; Aggerwal et al., 1973, Whitcomb et al., 1973).

The formation of new fractures in the deep zone of seismicity under Middle Mountain in addition to repeated slip on pre-existing planes is suggested by the relatively few microearthquake clusters there. Macroscopic shear fractures in rock under a compressive stress regime are oriented at an acute angle to the direction of maximum compressive stress, σ_I, according to the Coulomb criterion, but form by the coalescence of extensional (Mode I) microcracks that are themselves oriented parallel to σ_I (Brace et al., 1965). This process is accompanied by volume dilatancy, which increases the pore volume of the rock.

The effect of dilatancy on V_p/V_s ratio depends on whether the rock is dry or wet. Increasing the pore volume of a dry rock decreases the bulk rock values of both V_p and V_s. The effect on V_s is less than on V_p so V_p/V_s decreases. Introducing fluid into the void space strongly increases the effective bulk modulus of the rock and hence V_p, which approaches its intact rock value as fluid saturation increases, but has no effect on the shear modulus, so V_s is unchanged. Therefore, V_p/V_s in a partially saturated dilatant rock can significantly exceed its value in the intact rock. Fluid pore pressure is an additional variable in the problem, but its effect can be expressed in terms of changes in pore volume. Increasing pore pressure lowers the effective pressure on the pore space according to Equation (2.2), thus allowing the pores to expand and increasing the pore volume. In a partially saturated crack this will have only a small effect on V_p but will significantly decrease V_s, resulting in an increase in V_p/V_s.

The above arguments mean that a positive V_p/V_s anomaly, such as that under Middle Mountain, must involve either a decrease in pore volume if the cracks are dry or the effects of fluid saturation. In the general case of partially saturated cracks a positive V_p/V_s anomaly could be related to an increase in V_p due to saturation of previously dry cracks. However, the positive V_p/V_s anomaly under Middle Mountain appears to be caused by low V_s, which requires an increase in pore volume of partially saturated cracks. This is consistent with the existence of the dilatant damage zone suggested by the concentration of seismicity.

The effects of crack density and fluid saturation were quantified according to a non-interacting crack model by O'Connell and Budiansky (1974). Figure 5.15 shows the relationship between the fractional changes in V_s and V_p/V_s for different values of crack density, ε, and saturation, ξ. The ratios of the values of V_s and V_p/V_s within the positive V_p/V_s anomaly under Middle Mountain to average values at the same depth as

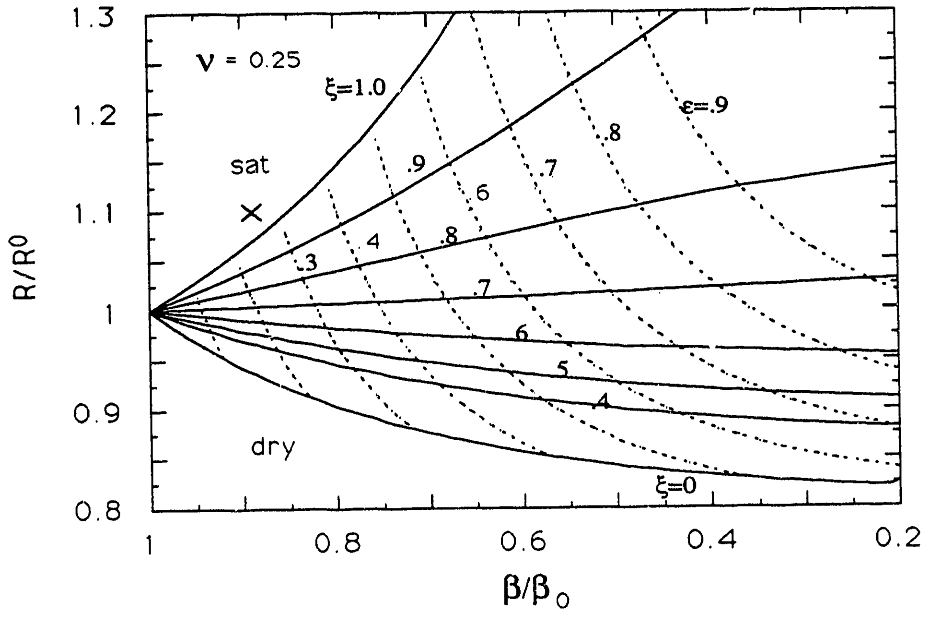

Figure 5.15: Fractional variation of V_S (β) and V_p/V_S (R) as functions of fracture density, ε (dotted curves), and fluid saturation, ξ (solid curves), for Poisson's ratio (ν) of 0.25. β_0 and R_0 are S-velocity and V_p/V_S ratio of uncracked solid, respectively. After O'Connell and Budiansky (1974). Data for positive V_p/V_S anomaly under Middle Mountain shown as cross.

the anomaly are plotted on this figure, and indicate that the damage zone has a modest fracture density compared with the country rock and is fully saturated.

The negative V_p/V_S anomalies within the Salinian and Franciscan blocks on either side of and above the positive anomaly and the relatively low V_p/V_S values within the fault zone to the NW of Middle Mountain suggest that the high saturation within the damage zone might be maintained by in-flow of fluid from these two zones. I propose that the permeability of the fault zone NW of the high-velocity body may be relatively high so that the fluid diffusion rate is comparable to the dilatancy rate within the damage zone. Therefore, the supply of fluid to the damage zone can be maintained without the fault zone to the NW becoming significantly undersaturated, and its V_p/V_s ratio remains only slightly below normal. Fluid could also be supplied from the wall rocks adjacent to the fault because the permeability of the rock near the fault is probably higher than normal due to fracturing associated with fault displacement (Chester and Logan, 1986). The intact rock away from the fault is less permeable. Therefore, the regions close to the fault that supply fluid to the damage zone will be recharged from the surrounding country rock at a lower rate than the dilatancy rate, and the pore pressure may drop. This will result in low V_p/V_s ratios in these regions, as observed, due to an increase in V_s. The feasibility of this hypothesis depends upon the actual permeabilities within the fault zone and in the wall rocks.

Once it is formed, the damage zone at Parkfield must be a permanent feature of the fault zone in front of the barrier which presumably is growing slowly towards the NW. The termination of seismicity at the NW end of the most intense part of the V_p/V_s anomaly suggests that dilatancy associated with the formation of new fractures is presently taking place only outside the core of the anomaly. This raises the possibility that the intensity of the anomaly may vary over the earthquake cycle in the following way. As the stress concentration in front of the barrier builds up after an earthquake, the pre-existing cracks within the core of the damage zone open parallel to the direction of the local shear stress. The hypothesized high permeability of the fault zone enables the cracks to remain close to saturation as they dilate, which means that the intensity of the positive V_p/V_s anomaly within the core of the damage zone would increase progressively as the stress builds up. When an earthquake and its foreshocks occur, the stress concentration is relaxed and the V_p/V_s ratio drops. The two negative anomalies on either side of the fault may also show a cyclical variation, depending on the diffusion time constants of the fractured rock on either side of the fault. If this scenario is correct, then it may provide a powerful earthquake prediction tool. This possibility is explored further in Chapter 6.

The possible cyclic variation in V_p/V_s discussed above is similar in some respects to that of the volume dilatancy/diffusion models, and to a fault zone dilatancy/diffusion model discussed by Rudnicki (1988). These models assume that significant changes in V_p/V_s occur on time scales of a few years and are caused by dilatancy of pre-existing and/or new cracks in response to the build-up of tectonic stress either in an extensive volume surrounding an incipient nucleation zone or within the fault zone itself. Because these models assume that the fluid diffusion rate is significantly less than the dilatancy rate, the dilatancy causes undersaturation and a drop in V_p/V_s. The attendant drop in pore pressure increases the effective normal stress, which leads to an increase in strength within the dilatant zone (dilatancy hardening) and further stress concentration. Fluid then diffuses into the dilatant zone, increasing the V_p/V_s ratio back to normal, increasing the pore pressure and causing weakening that results in earthquake nucleation.

However, the V_p/V_s.anomaly under Middle Mountain represents an average for the three-year period (1987-1989) covered by the travel time data set used in the inversion. Therefore, even if we are now in the immediate pre-nucleation phase of the cycle, the high value of the anomaly is not consistent with the previous models, which require a drop in V_p/V_s in the two or three years preceding an earthquake followed by a rise back to a normal (rather than an anomalously high) value. This leads to the most important difference between the possible cycle at Parkfield and the previous models, that of their implications on the strength and stability of the fault zone. The volume and fault zone dilatancy/diffusion models rely on the reduced pore pressure accompanying dilatancy to first strengthen the hypocentral zone so that it can act as an asperity, and then the rise in pore pressure accompanying diffusion to weaken it and so trigger unstable rupture. In contrast, the Parkfield model identifies the high-velocity body as the primary asperity/barrier and the dilatant zone as a subordinate feature.

The damage zone probably has a secondary effect on the nucleation process. Within the core of the zone the stress has been relieved by fracturing, and the normal to high fluid pore pressure implied by the high V_p/V_s ratio means that the effective pressure within this zone is normal to low. Therefore, tectonic loading (σ_1) within the high V_p/V_s zone is low. If the damage process has advanced to the stage of cataclasis and gouge production, the resulting granular material would be velocity weakening. Therefore, the core of the damage zone acts as a relaxation barrier with σ_1 being sufficiently low to inhibit even microearthquake activity, and this will retard the concentration of stress at the primary barrier.

If the hypothesized in-flow of fluid to the damage zone from the fault zone to the NW significantly lowers the pore pressure, then this may result in a strengthening of the fault plane there. This may account for the occurrence of relatively large earthquakes and foreshocks to the NW of the barrier on what is presumed to be inherently a Type 1 (stably sliding) contact. The relatively low stress drops of these events indicate a modest level of loading.

CHAPTER 6

GENERAL LITHOLOGICAL HETEROGENEITY MODEL

In this chapter I examine the application of the lithological heterogeneity model to fault zones in general. I begin by comparing the Loma Prieta and Parkfield asperity models. This enables common features of the models that may be of general applicability to be evaluated. Differences between the models indicate the variability in behavior that might be expected at different locations along a fault zone, under the influence such factors as scale, tectonic loading history and fault zone complexity. I also assess observational characteristics that may be diagnostic of lithological barriers/asperities, and suggest experiments that can be set up to detect and further investigate them.

6.1 Comparison of the Loma Prieta and Parkfield Asperity Models

The asperities imaged as high-velocity bodies at Parkfield and Loma Prieta are similar in many respects, the Parkfield asperity being a small-scale version of that at Loma Prieta. Both appear as ellipsoidal masses of anomalously high velocity rock that are cut by the active plane of the SAF. The fault planes within the rock masses are hypothesized to be Type 3 contacts, having high fracture strength and unstable frictional properties. Rupture of the asperity in each locality initiates at one end of the major axis of the ellipsoid, as predicted by the elliptical asperity model of Das and Kostrov (1985). Both nucleation points are apparently within the deepest part of the asperity, where the normal stress is highest. Rupture of the Parkfield asperity involved only the crustal section above about 12 km depth, whereas the Loma Prieta earthquake apparently ruptured through most of the crustal thickness, concomitant with the larger scale of the Loma Prieta asperity.

The important difference between the Loma Prieta and Parkfield ruptures is that the Loma Prieta earthquake nucleated at the end of the asperity furthest away from the Central Creeping Section of the SAF whereas the Parkfield earthquake nucleated at the end where stable sliding is arrested. I propose that this is because the build up in tectonic stress (σ_1) that caused the Loma Prieta barrier to evolved to an asperity included the contribution from dynamic loading by the 1906 earthquake as well as that from steady-state tectonic loading. This resulted in asymmetric loading of the Loma Prieta asperity and caused rupture to nucleate at its highly-stressed NW end. The Parkfield asperity, on the other hand, experiences only steady-state tectonic loading by arresting stable sliding at its NW end. Therefore, dynamic rupture nucleates at the NW end of the asperity, where the stress concentration is the highest.

The Parkfield earthquake ruptured through the entire asperity to the SE of the nucleation point. The Loma Prieta mainshock rupture appears to have been arrested within the SE part of the asperity. This may indicate that the stress distribution within the Parkfield asperity is not so severely asymmetric as that at Loma Prieta (Section 4.5), consistent with the lack of dynamic loading at Parkfield. The 1966 rupture propagated unilaterally to the SE and overshot the SE end of the asperity to trigger dynamic rupture on the presumed Type 2 (conditionally unstable) SAF plane to the SE. Dynamic rupture did not propagate to the NW because the low σ_1 on the fault plane NW of Middle Mountain meant that this plane acted as a relaxation barrier. The Loma Prieta rupture propagated both to the SE, through the asperity, and to the NW, where rupture on the relatively highly stressed Type 2 1906 earthquake plane was triggered by dynamic overshoot of the asperity rupture.

At both Loma Prieta and Parkfield the first effect of the barrier is seen as a fall-off in the surface creep rate. This is followed by an abrupt deepening of the microseismicity (see Hill et al., 1990, fig. 5.7), which is the manifestation of the build up of stress on the deep part of the fault plane immediately in front of the barrier as stable slip is arrested, and the resulting formation of a damage zone of intense fracturing.

At Pajaro Gap some of the deep microseismicity is seen as the cross-trends, which indicate that damage here has advanced to the stage of the formation of new faults having significant lengths. The most mature fault has developed along the favorable hard/soft contact between the high-velocity rock mass and the Franciscan rocks, thus relieving stress in the most efficient way possible. The damage zone at Middle

Mountain is less well developed and consists of series of short fractures. The damage process appears to be fairly well ordered, as indicated by the systematic alignment of the microearthquakes into sub-trends that dip at relatively shallow angles to the SW. The smaller size of the Middle Mountain barrier permits some stable sliding at shallow depths above it.

6.2 Application to Fault Zones in General: Geometrical Heterogeneity

The occurrence of large-scale material inhomogeneities associated with transitions in slip behavior along fault zones has been noted previously (Doser and Kanamori, 1986; Michael, 1988; Michael and Eberhart-Phillips, 1991). The fact that the few three-dimensional crustal velocity models of earthquake hypocentral zones that have been developed so far all image significant lithological inhomogeneities strongly suggests the fundamental role that such inhomogeneities play in controlling where and how earthquake ruptures nucleate and propagate.

Basic fracture and friction theory require fault zones to respond to material inhomogeneities in ways similar to those described at Loma Prieta and Parkfield. Such response may well be often the fundamental mechanism underlying the observed relationship between fault zone geometry and nucleation and arrest of earthquake rupture. The formation of splay faults, bends and offsets represent the more mature stage of the obstacle-avoiding process by which the fault system attempts to dissipate the stress concentration in front of a barrier. The formation of splay faulting at the frictional favorable hard/soft contact between the high-velocity body and Franciscan rocks at Pajaro Gap provides a good illustration of this process. In fact, on a larger scale the obstacle-avoiding process there may signal the incipient formation of a new main trace of the SAF. The tendency to circumvent the barrier is apparent a considerable distance to the SE, where the trend of the seismicity begins to describe a broad arc bending towards the north, and aligns with the cross-trends between Pajaro gap and Hecker Pass (U.S. Geological Survey, 1990). At the smallest scale, the fine structure of the damage zone revealed in the microseismicity under Middle Mountain suggests a relatively well-ordered process.

The response of fault zones to lithological heterogeneity is analogous to fracture processes in polycrystalline or two-phase materials such as ceramics (Lawn and Wilshaw, 1975, chap 6). In a two-phase material a crack tip that encounters a hard inclusion will either fracture through the inclusion, propagate along its boundary or propagate around the inclusion within the matrix, depending on which path offers the least fracture resistance. The behavior of a crack in this situation is controlled by a complex interplay between several factors, including the contrast in elastic properties between the inclusion and the matrix, the size and geometry of the inclusion, the cohesion of the boundary, the proximity of other fractures and inclusions, and the stressing history of the composite system. The same set of factors applies to fault zones, and we see all three types of obstacle-avoidance behavior at Loma Prieta and Parkfield. In the cases we are primarily concerned with, fracture of the intact inclusion is replaced by unstable slip on a pre-existing high-strength, unstable frictional contact within the inclusion. This contact heals and regains its fracture resistance (S) after dynamic rupture, so slip within the system is partitioned between dynamic slip within the body and quasi-static stable sliding along the boundary and on secondary faults within the matrix (country rock).

The behavior of a system once the obstacle avoiding process has been initiated depends upon the local stress field, which evolves along with the secondary fracture(s). Because the stress field evolves in a way that depends on the same set of factors that determines the initial response to the barrier, it rapidly becomes complex. Therefore, the detailed behavior of a given system can only be determined by numerical modeling. In some cases the geometry of the system and the evolving stress field will increasingly favor continued propagation of a particular splay fault and complete abandonment of the plane within the inclusion, thus leading to the development of a new main fault trace. In others, the splay fault will evolve to a geometry that is disfavored within the perturbed stress field and the splay will be abandoned. In the case that a fault encounters an intact obstacle (perhaps as a result of being previously deflected some distance away along strike, for example) the same set of factors pertains, and concentration of stress within the obstacle may eventually cause it to fracture, again creating a new main fault trace.

Since the partitioning of slip between dynamic rupture and stable sliding depends on the evolution of the local stress field, the earthquake cycle must also evolve with time. Therefore, the characteristic earthquake model can only involve quasi-stationary behavior. In addition, the lithological barrier/asperity concept demands that each barrier/asperity has a specific lifetime that is determined by the along-strike length of the fault contact within the inhomogeneity; once the two halves of the rock mass have slid past one another the unstable high-strength contact no longer exists. At an average Quaternary slip rate of about 40 mm/yr (Sims, 1989), the 10- and 30-km lengths of the Parkfield and Loma Prieta high-velocity bodies, respectively, imply barrier/asperity lifetimes on the order of 10^5-10^6 years, above the lower bound of 10^4 years set by the paleoseismicity data.

A macroscopic shear (Modes II and III) crack that develops in a compressional stress regime is oriented at an acute angle to the maximum principal stress direction, σ_I, in accordance with the Coulomb fracture criterion. The stress distribution (e.g. Segall and Pollard, 1980) resulting from the presence of the crack predicts that it will not propagate by new fracturing within its own plane (e.g. Lawn and Wilshaw, 1975, chap 3). Instead, extensional (Mode I) cracks propagate parallel to the σ_I direction from the Mode II and Mode III edges of the shear (see Scholz, 1990, p. 27). Propagation of the shear is achieved by the coalescence of the Mode I crack arrays to form a shear zone. Experimental evidence indicates that the Mode I cracks do not propagate for large distances, but the arrays of Mode I cracks are broken through by cracks parallel to the shear plane (Cox and Scholz, 1988a,b). Therefore, although this process can explain, and indeed requires, the complex geometries within fault zones themselves described in Chapter 1, it probably cannot account for large-scale bends, offsets and splays.

The differences between rupture nucleation, propagation and arrest within the Parkfield and Loma Prieta asperities during the 1966 and 1989 earthquakes illustrate the importance of previous loading history on asperity evolution and failure. Here again the stress field within and surrounding an asperity, even an isolated asperity that has uniform strength and frictional properties, rapidly becomes complex, and particularly so under asymmetric and dynamic loading. Therefore, evolution and failure of asperities can only be studied quantitatively by numerical modeling. However, the behavior of both asperities appears to be well described qualitatively by the simple elliptical asperity model of Das and Kostrov (1985).

6.3 Suggested Future Research

The above discussion suggests that detection and intensive investigation of large-scale heterogeneity should be an important part of research into fault zone segmentation and earthquake processes. The investigations of the Loma Prieta and Parkfield asperities suggest certain observational characteristics that may aid in targeting localities for detailed study.

The first symptom of the presence of the barrier at both Loma Prieta and Parkfield is the decline in the rate of surface creep. However, the high creep rate that characterizes the Central Creeping Section of the SAF has not been observed along other fault zones, so the fall off in creep rate would be much more subtle in most other places, and would therefore be of limited utility. The second observational feature is the abrupt increase in the intensity of deeper seismicity associated with the formation of the damage zone or secondary faulting at depth in front of the barriers at Loma Prieta and Parkfield. This is an inevitable result of the concentration of stress at a barrier as it evolves into an asperity, and is therefore likely to be a characteristic of many other barriers, including geometrical barriers (King, 1986). Previous workers (Poley et al., 1987) have commented on the deepening of seismicity at Middle Mountain and Pajaro Gap. In fact Moths et al. (1981) suggested that the latter may be symptomatic of a potential nucleation point NW of San Juan Bautista, thus correctly identifying the presence of the Loma Prieta asperity but not the actual nucleation zone. Olson (1986) has suggested that a zone of deeper seismicity adjacent to San Francisco may be associated with the epicenter of the 1906 earthquake.

A detailed systematic search for deeper than average background seismicity along the SAF and other fault zones, together with associated variations in surface creep rate and fault geometry, might enable areas for detailed study to be identified. The Hayward and Calaveras faults of East San Francisco Bay would be good candidates for this type investigation because they are characterized by intense microseismicity, have relatively high creep rates, and pose a significant earthquake risk. The high rate of seismicity in the East Bay, and in particular the broadness and relatively deep extent of the seismic zone (see Hill et al., 1990, figs. 5.6 and 5.8), would provide good constraint on three-dimensional velocity models to image potential asperities directly. This is even more true of the SAF system in southern California.

From a purely research perspective, detailed investigation of the variations in seismicity and creep rate associated with the rupture zones of M5 earthquakes along the Central Creeping Section, similar to the study of Wesson et al. (1973), would enable experiments to be carefully designed to image selected zones. Here again, the abundant seismicity provides constraint for three-dimensional velocity models. Along most of the Central Creeping Section the distribution of microearthquakes is essentially planar, as it is at Parkfield, and provides only limited ray coverage of the target volume. However, the seismic zone broadens at Bear Valley, which is also the source of M5 earthquakes (Ellsworth, 1975), so this would be a good candidate area.

Three-component, high-gain seismographs would be deployed to augment existing instruments in the selected areas, to achieve coverage similar to that at Parkfield. These networks would be designed to maximize ray coverage of the asperities. In addition, having identified target areas of limited extent, reflection and refraction surveys would be feasible.

The damage zone in front of the Middle Mountain barrier is apparently imaged directly as the positive V_p/V_s anomaly there. The possibility that the intensity of this anomaly may vary through the earthquake cycle may provide a potentially powerful tool for earthquake prediction. The present velocity models average the velocities within the model volume over the three year period of the data sample. Therefore, recomputing the models using the next three or four years of data will be required to detect possible changes in the damage zone as a whole. However, it should be possible to detect changes in P and S velocities within the zone by continuously sampling only specific ray paths that penetrate the damage zone and the surrounding rock. The deep microearthquake clusters under Middle Mountain provide an ideal energy source for this monitoring. The relative arrival times from these almost identical repeating earthquakes can be determined with a precision of approximately ±0.3 ms using the cross-correlation/cross-spectrum technique described in Section 5.4.3. It will be particularly important to look for the significant changes that this hypothesis predicts should follow the next Parkfield earthquake, when it should be possible to image the damage zone relatively accurately using aftershock data.

It is doubtful that the small damage zone at Parkfield could have been detected by routine monitoring using a regional network. However, the Parkfield barrier is a relatively small-scale feature and the larger damage zones that are likely to be associated with larger barriers, such as that at Loma Prieta, may be observable in the P- and S-wave data collected by the next generation of three-component, high-gain, broadband regional networks. It may be possible to detect larger scale anomalous V_p/V_s zones using relatively few selected ray paths, as suggested above. If V_p/V_s anomalies are indeed a ubiquitous feature associated with the damage zones adjacent to barriers, then attempting to image such an anomaly at Pajaro Gap, where the barrier and damage zone have been located, would provide a test of the feasibility of this idea. This could be achieved by deploying high-gain, three-component seismographs in this area to record P- and S-waves from the deeper earthquakes, and by making use of the limited S-wave data recorded from the 1989 aftershock sequence.

CHAPTER 7

CONCLUSIONS

The research described in this dissertation has demonstrated the utility of three-dimensional earthquake tomography in investigating the structure and mechanics of a major active fault zone. In particular, I have illustrated the major influence that large-scale along-strike lithological heterogeneity can have on fault strength and frictional stability, and hence on the nucleation and propagation of earthquake rupture. I propose that this influence may often provide the fundamental mechanical framework underlying commonly observed relationships between fault geometry and fault zone segmentation.

I have studied the creeping-to-locked transitions at either end of the Central Creeping Section of the San Andreas Fault (SAF) using available existing three-dimensional crustal velocity models of the Loma Prieta and Parkfield sections of the fault zone. The joint velocity/hypocenter inversion for Loma Prieta includes only P-wave data. Both P- and S-wave velocity models are available for Parkfield. The P-wave velocity (V_p) models are calibrated in terms lithology by experimental V_p-pressure and V_p-temperature data for known basement rock types on either side of the fault in the two areas, and by seismic refraction models. The shallow parts of the three-dimensional models generally correlate well with the surface geology, and the unperturbed deeper parts of the models are in good agreement with the refraction data. The resolution of the Loma Prieta model is about 2-3 km, while that of the smaller and more densely sampled Parkfield V_p model is about 1-2 km. The Parkfield V_s model is less well resolved than the V_p model.

Large anomalous high-velocity bodies are imaged at mid-crustal depths along both sections of the fault. The ellipsoidal shapes of the bodies are similar, but the Parkfield body is smaller. The southeastern extent of the Parkfield body is not resolved by the velocity model, and the depth extent of neither body is resolved. The Loma Prieta V_p model and other geophysical data suggest that the high-velocity body may be continuous with the outcrop of quartz-hornblende gabbro at Logan. A similar relationship is possible between the Parkfield high-velocity body and the gabbro outcrop at Gold Hill--which is correlative with the

Logan gabbro--but the association is more tenuous in this case. The theoretical velocity calculated for the Logan and Gold Hill gabbro composition is in general agreement with the velocities of the high-velocity bodies. The V_p/V_s ratio within the Parkfield high-velocity body is consistent with a gabbroic composition but only a small part of the high-velocity body is resolved by the V_p/V_s model so this result is not conclusive. The modestly high V_p/V_s value (1.8-1.85) of the high-velocity body suggests that the body is not composed of granitic gneiss of the type that outcrops SW of the SAF, and argues against a partially-serpentinized peridotite composition. The sum of evidence, therefore, favors a gabbroic composition for both high-velocity bodies, but is not adequate to rule out a range of alternative mafic, ultramafic or gneissic compositions.

Both high-velocity bodies are cut by the main active plane of the SAF. Both clearly play a primary role in arresting stable sliding at either end of the Central Creeping Section of the SAF, as evidenced by the fall off in surface creep rate and the cessation of minor creep-related seismicity as the fault encounters the bodies. The aftershocks of the 1966 Parkfield and 1989 Loma Prieta earthquakes define the active fault plane through the respective high-velocity bodies, indicating that these planes rupture unstably.

The mechanics of these slip transitions are investigated in terms of a general heterogeneous fault model that unifies the concepts of fault strength and frictional stability in terms of the material properties of the fault contact. I propose that the property that dictates the transition from stable to unstable sliding as the fault encounters a high-velocity body is the change in the relative hardnesses of the wall rocks that are in contact at the fault. Outside of the high-velocity bodies there is a hard/soft contact, while within the bodies the contact is hard/hard. High-contrast hard/soft contacts produce a thick gouge layer, which inherently results in stable sliding. Hard/soft contacts having a lower contrast produce less gouge and may be conditionally stable, failing unstably only when subjected to dynamic loading during an earthquake. Hard/hard contacts produce little gouge, have high fracture strengths, and exhibit only unstable stick-slip failure. The high fracture strength of a hard/hard contact enables it to act as a barrier to stable sliding and to dynamic rupture. The increasing stress concentration at the contact can cause it to evolve from a barrier to an asperity which ruptures unstably when the load reaches the fracture strength of the contact and nucleates dynamic rupture on the adjoining conditionally stable fault plane.

The hypocenters of the 1966 and 1989 earthquakes appear each to be located within the respective high-velocity body, indicating that the hard/hard fault contacts within the bodies evolved from barriers to asperities according to the above model. The nucleation points in both cases are at one end of the major axis of the elliptical fault plane within the body, and the primary ruptures propagated as strike-slip displacement along the plane. This agrees with a theoretical elliptical asperity model under quasi-static loading, in which rupture will always nucleate at one end of the major axis of the asperity and propagate in-plane though the asperity. The Loma Prieta earthquake nucleated at the NW end of its asperity, opposite to the point at which stable sliding is arrested. I propose that this is because the Loma Prieta high-velocity body was the barrier that arrested the 1906 earthquake rupture at its southeastern extent, and therefore was loaded dynamically. Subsequent steady-state tectonic loading brought the asperity to failure in 1989, but the stress distribution was highly asymmetric and the 1989 earthquake nucleated at its highly-stressed NW end. The Parkfield barrier undergoes only steady-state loading by arresting stable sliding at its NW end. Therefore, the NW end of this asperity is the most highly stressed, and rupture nucleates there. The aftershock distributions of both earthquakes indicate that the asperity failures triggered dynamic rupture on adjacent conditionally stable fault planes beyond the asperities, to the SE at Parkfield and to the NW at Loma Prieta.

The second response to the arrest of stable sliding at a barrier is for the fault system to attempt to avoid the obstacle by transferring slip to secondary structures. These may be existing secondary faults, such as the Sargent fault at Loma Prieta and perhaps the Southwest Fracture Zone at Parkfield. Microseismicity on the Sargent fault begins adjacent to Pajaro Gap, where creep-related seismicity shuts off on the main SAF plane as it enters the high-velocity body. At Parkfield most of the shallow seismicity both NW of Middle Mountain and directly above the high-velocity body occurs on a secondary fault that intersects the main SAF plane at depth and that may be a buried extension of the Southwest Fracture Zone that is mapped further SE. Locking the main fault plane within the high-velocity bodies perturbs the local stress fields in such a way as to initiate slip on the pre-existing faults.

New secondary structures are formed immediately in front of the barrier in an attempt to reduce the stress concentration there. At Pajaro Gap this process has advanced to the stage of formation of new secondary faults of appreciable length. The best developed secondary fault at Pajaro Gap appears to be growing along the hard/soft contact between the high-velocity body and Franciscan rocks, which, according to the strength/stability model, offers the minimum fracture resistance path. I propose that this kind of obstacle-avoidance process is an important mechanism in the development of fault splays, bends and offsets, and is often the fundamental cause of the observed relationship between fault geometry and the nucleation and arrest of earthquake rupture.

Formation of new splay faults represents the more mature stage of in the development of a damage zone of intense fracturing in front of barriers. Systematic trends in the deep seismicity under Middle Mountain indicate that the damage process is fairly well ordered. The Middle Mountain damage zone is imaged directly as an intense positive V_p/V_s anomaly that results from the dilatancy accompanying fracturing. I propose an hypothesis whereby the fluid saturation within the damage zone is maintained by in-flow from the fault zone to the NW and from the wall rocks on either side. The model includes the possibility that the intensity of the V_p/V_s anomaly could vary through the earthquake cycle as the existing fractures within the core of the damage zone open and close under the varying local stress concentration, but the present velocity models do not constrain such variation. This model differs from previous dilatancy/diffusion models of earthquake nucleation in that the strength of the nucleation zone does not derive from the dilatancy, but the damage zone is merely a consequence of the presence of the inherently strong and frictionally unstable lithological barrier. The dilatancy/diffusion model is speculative and its feasibility can only be tested by hydrological modeling based upon realistic estimates of the permeability of the fault zone and wall rocks.

The question of why the Central Creeping Section as a whole exhibits predominantly stable sliding behavior has been only partly resolved. Earlier workers have proposed that the presence of the Great Valley sequence as the NE wall rock of the fault promotes stable sliding. This is supported to some extent by the Loma Prieta velocity model SE of Pajaro Gap, where the intense creep-related microseismicity above 8 km depth is taking place at the contact between the Gabilan granite and the Great Valley sequence. This stable sliding behavior is attributed, according to the fault stability model, to the hard/soft nature of this contact, and does not rely on high pore pressure or the presence of serpentinite. However, the Salinian/Franciscan contact below 8 km presumably is also sliding stably, whereas the same contact NW of the high-velocity body is conditionally stable. The presence of serpentinite in the small quantities that are apparently needed to promote stable sliding cannot be resolved by the present velocity models. The northwestern end of the Parkfield V_p/V_s model is not resolved below 8 km depth so the possible role of high pore pressure at the Salinian/Franciscan contact within the Central Creeping Section cannot yet be addressed.

The chief limitation of earthquake travel time tomography is that it requires an abundance of well-distributed, well-recorded earthquakes, limiting its usefulness along sections of fault zones that have only low levels of background seismicity. The latter unfortunately include locked fault segments or seismic gaps where often we would particularly like to look for asperities and barriers. Of course, it should often be possible to image the asperity responsible for a large earthquake after the event using its aftershocks. Another limitation is the method's resolution, which at shallow and mid-crustal depths will probably remain limited to about one km at best. Resolution of the deeper parts of a model falls off very rapidly as the bottom of the seismogenic zone is approached, which is particularly troublesome because it is there that large earthquakes nucleate. V_p/V_s models, which enable elastic properties to be estimated and offer strong lithological constraints, are significantly less well resolved than V_p models owing to the inherently lower accuracy and paucity of S-wave travel times. Suggested experiments to identify potential barrier/asperity locations are outlined in Chapter 6. Once target zones have been defined, optimal results will be obtained by carefully designing monitoring networks to take full advantage of seismicity distributions to minimize these limitations.

The present study gives only a qualitative description of the mechanics of the lithological barriers/asperities imaged at Parkfield and Loma Prieta that are generally consistent with kinematic models of the earthquake ruptures. However, the fact that three-dimensional tomography studies are now feasible on a routine basis represents a large step forward in quantitative research into fault zone mechanics. For the first time barriers and asperities that hitherto could only be inferred from surface fault geometry and seismicity distributions can be imaged directly. These images provide not only the geometry and locations of the barriers and asperities, but also realistic constraints on their *in situ* elastic properties. Identifying the lithologies of the bodies and other fault wall rocks will enable laboratory research to be directed towards determining the strengths and frictional properties of appropriate lithological contacts. These data will provide the input to quasi-static and dynamic fault slip models that can be as realistic as evolving computational techniques allow. The images also provide data upon which to base research into the development of large-scale fault zone geometry, which will have an important bearing on models of fault zone evolution and displacement history on a geological time scale.

REFERENCES

Aggerwal, Y.P., L.R. Sykes, D.W. Simpson, and P.G. Richards, Spatial and temporal variations of t_s/t_p and in P wave residuals at Blue Mountain Lake, New York: Application to earthquake prediction, *J. Geophys. Res.*, 80, 718-732, 1973.

Aki, K., Characterization of barriers on an earthquake fault, *J. Geophys. Res.*, 84, 6140-6148, 1979.

Aki, K., Seismic displacements near a fault, *J. Geophys. Res.*, 73, 5359-5376, 1968.

Allen, C.R., The tectonic environments of seismically active areas along the San Andreas fault system, in *Proceedings of Conference on Geological Problems of the San Andreas Fault System, Stanford, Calif.*, ed. W.R. Dickinson and A. Grantz, Stanford Univ. Publications in the Geological Sciences, 11, 70-82, 1968.

Allen, C.R., The modern San Andreas fault, in *The Geotectonic Development of California*, ed. W.G. Ernst, Prentice Hall, Inc., Englewood Cliffs, New Jersey, 512-534, 1981.

Anderson, E.M., *The Dynamics of Faulting*, 2nd ed., Oliver and Boyd, Edinburgh, 1951.

Anderson, J., A dislocation model for the Parkfield earthquake, *Bull. Seismol. Soc. Am.*, 64, 671-686, 1974.

Andrews, D.J., Rupture propagation with finite stress in antiplane strain, *J. Geophys. Res.*, 81, 3575-3582, 1976.

Antolik, M., W. Foxall, and T.V. McEvilly, Microearthquake clusters at Parkfield: Constraint on fault-zone structure and failure processes, *EOS, Trans. Am. Geophys. Union*, 72, 483, 1991.

Archuleta, R.J., and S.M. Day, Dynamic rupture in a layered medium: The 1966 Parkfield earthquake, *Bull. Seismol. Soc. Am.*, 70, 671-689, 1980.

Aviles, C.A., C.H. Scholz, and J. Boatwright, Fractal analysis applied to characteristic segments of the San Andreas fault, *J. Geophys. Res.*,92, 331-344, 1987.

Bailey, E.H., M.C. Blake, and D.L. Jones, On-land Mezozoic oceanic crust in California Coast Ranges, *Geological Survey Research, 1970, U.S. Geol. Surv. Prof. Pap.* 700-C, C70-C81, 1970.

Bailey, E.H., W.P. Irwin, and D.L. Jones, Franciscan and related rocks, and their significance in the geology of western California, *California Div. Mines and Geol. Bull.* 183, 177 p., Sacramento, California, 1964.

Bakun, W.H., and T.V. McEvilly, Recurrence models and Parkfield, California earthquakes, *J. Geophys. Res.*, 89, 3051-3058, 1984.

Bakun, W.H., and T.V. McEvilly, P-wave spectra for M_L5 foreshocks, aftershocks, and isolated earthquakes near Parkfield, California, *Bull. Seismol. Soc. Am.*, 71, 423-436, 1981.

Bakun, W.H., and T.V. McEvilly, Earthquakes near Parkfield, California: Comparing the 1934 and 1966 sequences, *Science*, 205, 1375-1377, 1979.

Bakun, W.H., R. M. Stewart, C. G. Bufe, and S. M. Marks, Implication of Seismicity for failure of a section of the San Andreas fault, *Bull. Seismol. Soc. Am.*, 70, 185-201, 1980.

Bakun, W.H., and A.G. Lindh, The Parkfield, California, prediction experiment, *Earthquake Prediction Res.*, 3, 285-304, 1985.

Beroza, G.C., Near-source modeling of the Loma Prieta earthquake: Evidence for heterogeneous slip and implications for earthquake hazard, *Bull. Seismol. Soc. Am.*, 81, 1603-1621, 1991.

Beroza, G.C, and P. Spudich, Linearized inversion for fault rupture behavior: application to the 1984 Morgan Hill, California earthquake, *J. Geophys. Res.*, 93, 6275-6296, 1988.

Berry, F. A. F., High fluid potentials in California Coast Ranges and their tectonic significance, *Am. Assoc. Petrol. Geol. Bull*, 57, 1219-1249, 1973.

Birch, F., The velocity of compressional waves in rocks to 10 kilobars, part I, *J. Geophys. Res.*, 65, 1083-1102, 1960.

Boore, D. M., Strong-motion recordings of the California earthquake of April 18, 1906, *Bull. Seismol. Soc. Am.*, 67, 561-577, 1977.

Brabb, E. E., and W.F.Hanna,, Maps showing aeromagnetic anomalies, faults, earthquake epicenters, and igneous rocks in the southern San Francisco Bay region, California, *U.S. Geol..Surv. Geophys. Invest. Map* GP-977, scale 1:125,000, 1981.

Brace, W.F., Laboratory studies of stick-slip and their application to earthquakes, *Tectonophysics*, 14, 189-200,.1972.

Brace, W.F., B.W. Paulding, and C. Scholz, Dilatancy in the fracture of crystalline rocks *J. Geophys. Res.*, 71, 3939-3953, 1965.

Brown, R.D., Map showing recently active breaks along the San Andreas and related faults between the northern Gabilan Range and Cholame Valley, California, *U.S. Geol. Surv. Misc. Geol. Invest. Map* I-575, scale 1:24,000, 1970.

Brown, R.D., and J.G. Vedder, R.E. Wallace, E.F. Roth, R.F. Yerkes, R.O. Castle, A.O. Waananen, R.W. Page, and J.P. Eaton, The Parkfield-Cholame California, earthquakes of June-August 1966 - surface geological effects, water-resources aspects, and preliminary seismic data, *U.S. Geol. Surv. Prof. Pap.* 579, 66 p., 1967.

Burford, R.O., and P.W. Harsh, Slip on the San Andreas fault in central California from alinement array surveys, *Bull. Seismol. Soc. Am.*, 70,1223-1261, 1980.

Byerlee, J.D., Friction of rocks,*Pure and Applied Geophys*, 116, 615-626, 1978.

Byerlee, J.D., The mechanics of stick-slip, *Tectonophysics*, 9, 475-486, 1970.

Byerlee, J.D., and W.F. Brace, Stick-slip, stable sliding, and earthquakes - effect of rock type, pressure, strain rate, and stiffness, *J. Geophys. Res.*, 73, 6031-6037, 1968.

Carmichael, R.S., *Handbook of Physical Properties of Rocks*, vol II, CRC Press, Inc., Boca Raton, Florida, 345 p., 1982.

Chester, F.M., and J.M. Logan, Implications for mechanical properties of brittle faults from observations of the Punchbowl fault zone, California, *Pure and Applied Geophys*, 124, 79-106, 1986.

Choy, G.L., and J. Boatwright, Source characteristics of the Loma Prieta, California earthquake of October 18, 1989 from global digital seismic data, *Geophys. Res. Lett.*, 17, 1183-1186, 1990.

Christensen, N.I., Ophiolites, seismic velocities and oceanic crustal structure, *Tectonophysics.*, 47, 131-157, 1978.

Christensen, N.I., Elasticity of ultrabasic rocks, *J. Geophys. Res.*, 71, 5921-5931, 1966a.

Christensen, N.I., Shear wave velocities in metamorphic rocks at pressures to 10 kilobars, *J. Geophys. Res.*, 71, 3549-3556, 1966b.

Christensen, N.I., Compressional wave velocities in metamorphic rocks at pressures to 10 kilobars, *J. Geophys. Res.*, 70, 6147-6164, 1965.

Christensen, N.I., and M.H. Salisbury, Structure and constitution of the lower oceanic crust, *Rev. Geophys. Space Phys.*, 13, 57-86, 1975.

Clark, J.C., and J.D. Rietman, Oligocene stratigraphy, tectonics, and paleogeography southwest of the San Andreas fault, Santa Cruz Mountains and Gabilan Range, California Coast Ranges, *U.S. Geol. Surv. Prof. Pap.* 783, 18 p., 1973.

Cox, S.J.D., and C.H. Scholz, An experimental study of shear fracture in rocks: Mechanical observations, *J. Geophys. Res.*, 93, 3307-3320, 1988a

Cox, S.J.D., and C.H. Scholz, On the formation and growth of faults: An experimental study, *J. Struct. Geol.*, 10, 413-430, 1988b.

Daley, T.M., and T.V. McEvilly, Joint VSP and earthquake tomography for fault-zone structure, *Seismol. Res. Lett.*, 63, 62, 1992.

Das, S., and K. Aki, Fault plane with barriers: A versatile earthquake model, *J. Geophys. Res.*, 82, 5658-5670, 1977.

Das, S., and B.V. Kostrov, An elliptical asperity in shear: Fracture process and seismic radiation, *Geophys. J. Roy. Astr. Soc.*, 80, 725-742, 1985.

DeMets, C.G., S. Stein, and D.F. Argus, A revised estimate of Pacific-North American motion and implications for western North America plate boundary zone tectonics, *Geophys. Res. Lett.*, 14, 911-914, 1987.

Dibblee, T.W., Geology along the San Andreas fault from Gilroy to Parkfield, in *Studies of the San Andreas Fault Zone in Northern California*, eds. R. Streitz and R.W. Sherburne, Calif. Div. Mines Geol. Special Rept. 140, 3-18, 1980.

Dickinson, W.R., Structural relationships of San Andreas fault system, Cholame Valley and Castle Mountain Range, California, *Geol. Soc. Am. Bull.*, 77, 707-726, 1966.

Dieterich, J., Modeling of rock friction 1: Experimental results and constitutive equations, *J. Geophys. Res.*, 84, 2162-2168, 1979.

Doser, D.I., and H. Kanamori, Depth of seismicity in the Imperial Valley region (1977-1983) and its relation to heat flow, crustal structure, and the October 15, 1979, earthquake, *J. Geophys. Res.*, 91, 675-688, 1986.

Eaton, J.P., M.E. O'Neill, and J.N. Murdock, Aftershocks of the 1966 Parkfiled-Cholame, California, earthquake: A detailed study, *Bull. Seismol. Soc. Am.*, 60, 1151-1197, 1970.

Eberhart-Phillips, D., Investigations of crustal structure and active tectonic processes in the Coast Ranges, central California, Ph.D. thesis, Stanford Univ., 1989.

Eberhart-Phillips, D., V.F. Labson, W.D. Stanley, A.J.Michael, and B.D Rodriguez, Preliminary velocity and resestivity models of the Loma Prieta earthquake region, *Geophys. Res. Lett.*, 17, 1235-1238, 1990.

Ellsworth, W.L., The making of a quake: Some suprises from Loma Prieta, *EOS, Trans. Am. Geophys. Union*, 73, 44, 1992.

Ellsworth, W.L., Bear Valley, California earthquake sequence of February-March, 1972, *Bull. Seismol. Soc. Am.*, 65, 483-506, 1975.

Engelder, J.T., and C.H. Scholz, The role of asperity indentation and ploughing in rock friction - II. Influences of relative hardness and normal load, *Int. J. Rock Mech. Min. Sci. & Geomech. Abstr.*, 13, 155-163, 1976.

Ernst, W.G., Petrological reconaissance of Franciscan metagraywackes from the Diablo Range, central California Coast Ranges, *J. Petrol.*, 12, 413-437, 1971.

Feng, R. and T. V. McEvilly, Interpretation of seismic reflection profiling data for the structure of the San Andreas fault zone, *Bull. Seismol. Soc. Am.*, 73, 1701-1720, 1983.

Filson, J., and T.V. McEvilly, Love wave spectra and the mechanism of the 1966 Parkfield sequence, *Bull. Seismol. Soc. Am.*, 57, 1245-1257, 1967.

Foxall, W., and T.V. McEvilly, The microearthquake process as seen in high resolution with the Parkfield network, *Seismol. Res. Lett.*, 59, 1, 1988.

Foxall, W., and T.V. McEvilly, The Parkfield downhole seismic array: Preliminary analysis of microearthquakes, *EOS, Trans. Am. Geophys. Union*, 68, 1346, 1987.

Fuis, G.S., and W.D. Mooney, Lithosperic structure and tectonics from seismic-refraction and other data, in *The San Andreas Fault System, California*, ed. R.E. Wallace, U.S. Geol. Surv. Prof. Pap. 1515, 207-236, 1990.

Gu, J.C., J.R. Rice, A.L. Ruina,and S.T. Tse, Slip motion and stability of a single degree of freedom elastic system with rate and state dependent friction, *J. Mech. Phys. Sol.*, 32, 167-196, 1984.

Hanks, T.C., and R.K. McGuire, The character of high-frequency strong ground motion, *Bull. Seismol. Soc. Am.*, 71, 2071-2095, 1981.

Hanna, W.F., R.D Brown, D.C. Ross, and A. Griscom, Aeromagnetic reconnaissance and generalized geological map of the San Andreas fault between San Francisco and San Bernadino, California, *U.S. Geol. Surv. Geophys. Invest. Map* GP-815, 1972.

Harris, R.A., and P. Segall, Detection of a locked zone at depth on the Parkfield, California, segment of the San Andreas fault,. *J. Geophys. Res.*, 92, 7945-7962, 1987.

Haskell, N. A., Total energy and spectral density of elastic wave radiation from propagating faults, *Bull. Seismol. Soc. Am*, 54, 1811-1841, 1964.

Healy, J.H., and L.G. Peake, Seismic velocity structure along a section of the San Andreas fault near Bear Valley, California, *Bull. Seismol. Soc. Am.*, 65, 1177-1197, 1975.

Hill, D.P., J.P. Eaton, and L.M. Jones, Seismicity, 1980-86, in *The San Andreas Fault System, California*, ed. R.E. Wallace, U.S. Geol. Surv. Prof. Pap. 1515, 115-151, 1990.

Husseini, M.I., D.B. Jovanovich, M.J. Randall, and L.B. Freund, The fracture energy of earthquakes, *Geophys. J. Roy. Astr. Soc.*, 43, 367-385, 1975.

Irwin, W.P., Geology and plate tectonic development, in *The San Andreas Fault System, California*, ed. R.E. Wallace, U.S. Geol. Surv. Prof. Pap. 1515, 61-80, 1990.

Irwin, W.P., and I. Barnes, Effect of geologic structure and metamorphic fluids on seismic behaviour of the San Andreas fault system in central and northern California, *Geology*, 3, 713-716, 1975.

Irwin, W.P., and I. Barnes, Tectonic relations of carbon dioxide discharges and earthquakes, *J. Geophys. Res.*, 85, 3115-3121, 1980.

Jaeger, J.C., and N.G.W. Cook, *Fundamentals of Rock Mechanics*, 3rd ed., 593 p., Chapman and Hall, London, 1979.

Jennings,C.W., *Geologic Map of California*, California Div.Mines and Geol., Sacramento, California, 1: 750,000, 1977.

Kanamori, H., Rupture process of subduction-zone earthquakes, *Ann. Rev. Earth Planet. Sci.*, 14, 293-322, 1986.

Karageorgi, E., R. Clymer, and T.V. McEvilly, Seismological studies at Parkfield. II. Search for temporal variations in wave propagation using Vibroseis, *Bull. Seismol. Soc. Am.*, 82, 1388-1415, 1992.

Kern, H., and A. Richter, Temperature derivatives of compressional and shear wave velocities in crustal and mantle rocks at 6 kbar confining pressure, *J. Geophys.*, 49, 47-56, 1981.

King, G.C.P., Speculations on the geometry of the initiation and termination of earthquake rupture and the evolution of morphology and geological structures, *Pure and Applied Geophys*, 124, 567-585, 1986.

King, G.C.P., The accommodation of large strains in the upper lithosphere of the Earth and other solids by self-similar fault systems: The geometrical origin of b-value, *Pure and Applied Geophys.*, 121, 761-815, 1983.

King, G. C. P., and J. Nabelek, Role of fault bends in the initiation and termination of earthquake rupture, *Science*, 228, 984-987, 1985.

Lachenbruch, A.H., and J.H. Sass, Thermomechanical aspects of the San Andreas fault system, in *Proceedings of the Conference on Tectonic Problems of the San Andreas Fault System*, ed. R.L. Kovach and A. Nur, Stanford University Publications in the Geological Sciences, 13, 192-205, 1973.

Lawn, B.R., and T.R. Wilshaw, *Fracture of Brittle Solids*, Cambridge University Press, Cambridge, 204 p., 1975.

Lay, T., and H. Kanamori, Earthquake doublets in the Solomon Islands, *Phys. Earth Planet Interiors*, 21, 283-304, 1980.

Lay, T., H. Kanamori, and L. Ruff, The asperity model and the nature of large subduction zone earthquakes, *Earthquake Prediction Res.*, 1, 1-71, 1982.

Levy, N.A., and A.K. Mal, Calculation of ground motion in a three-dimensional model of the 1966 Parkfield earthquake, *Bull. Seismol. Soc. Am.*, 66, 405-423, 1976.

Lienkaemper, J.J., and W.H. Prescott, Historic surface slip along the San Andreas fault near Parkfield, California, *J. Geophys. Res.*, 94, 17,647-17,670, 1989.

Lin, W., and C.-Y. Wang, P-wave velocity in rocks at high pressure and temperature and the constitution of the central California crust, *Geophys. J. R. Astr. Soc.*, 61, 379-400, 1980.

Lindh, A.G., and D.M. Boore, Control of rupture by fault geometry during the 1966 Parkfield earthquake, *Bull. Seismol. Soc. Am*, 71, 95-116, 1981.

Logan, J.M., and L.W. Teufel, The effect of normal stress on the real area of contact during frictional sliding in rocks, *Pure and Applied Geophys*, 124, 471-485, 1986.

Louie, J.N., R.W. Clayton, and R.J. LeBras, Three-dimensional imaging of a steeply-dipping structure near the San Andreas fault, Parkfield, California, *Geophysics*, 53, 176-185, 1988.

Madariaga, R., High-frequency radiation from crack (stress drop) models of earthquake faulting, *Geophys. J. Roy. Astr. Soc.*, 51, 625-651, 1977.

Marone, C., C.B. Rayleigh, and C.H. Scholz, Frictional behavior and constitutive modeling of simulated fault gouge, *J. Geophys. Res.*, 95, 7007-7025, 1990.

Marone, C., and C.H. Scholz, The depth of seismic faulting and the upper transition from stable to unstable slip regimes, *Geophys. Res. Lett.*, 15,621-624, 1988.

McBride, J.H. and L.D. Brown, Reanalysis of the COCORP deep seismic reflection profile across the San Andreas fault, Parkfield, California, *Bull. Seismol. Soc. Am*, 76, 1668-1686, 1986.

McEvilly, T.V., W.H. Bakun, and K.B. Casaday, the Parkfield, California, earthquakes of 1966, *Bull. Seismol. Soc. Am*, 57, 1221-1244, 1967.

McLaughlin, R.J., The Sargent-Berrocal fault zone and its relation to the San Andreas fault system in the southern San Francisco Bay region and Santa Clara Valley, California, *J. Res. U.S. Geol. Surv.*, 2, 593-598, 1974.

McLaughlin, R.J., J.C. Clark, and E.E. Brabb, Geological map and structure sections of the Loma Prieta 7 1/2' quadrangle, Santa Clara and Santa Cruz Counties, California, *U.S. Geol. Surv. Open File Map* 88-752, 1988.

Mendoza, C., and S. Hartzell, Aftershock patterns and earthquake faulting, *Bull. Seismol. Soc. Am.*, 78,1438-1449, 1988.

Michael, A.J., Effects of three-dimensional velocity structure on the seismicity of the 1984 Morgan Hill, California, aftershock sequence, *Bull. Seismol. Soc. Am.*, 78, 1199-1221, 1988.

Michael, A.J., and D. Eberhart-Phillips, Relations among fault behavior, subsurface geology, and three-dimensional velocity models, *Science*, 253, 651-654, 1991.

Michelini, A., Fault zone structure determined through the analysis of earthquake arrival times, Ph.D. thesis, Univ. California., Berkeley, 1991.

Michelini, A., and T.V. McEvilly, Seismological studies at Parkfield: I. Simultaneous inversions for velocity structure and hypocenters using cubic B-splines parameterization, *Bull. Seismol. Soc. Am.*, 81, 524-552, 1991.

Moody, J.B., and E.M. Hundley-Goff, Microscopic characteristics of orthoquartzite from sliding friction experiments. II. Gouge, *Tectonophysics*, 62, 301-319, 1980.

Mooney, W.D., and R.H. Colburn, A seismic refraction profile across the San Andreas, Sargent, and Calaveras faults, west-central California, *Bull. Seismol. Soc. Am.*, 75, 175-191, 1985.

Mooney, W.D., and A. Ginzburg, Seismic measurements of the internal properties of fault zones, *Pure and Applied Geophys*, 124, 141-157, 1986.

Mooney, W.D., and J.H. Leutgert, A seismic refraction study of the Santa Clara Valley and southern Santa Cruz Mountains, west-central California, *Bull. Seimol. Soc. Am.*, 72, 901-909, 1982.

Moths, B.L., A.G. Lindh, W.L. Ellsworth, and L. Fluty, Comparison between the seismicity of the San Juan Bautista and Parkfield regions, California, (abs.), *EOS, Trans. Am. Geophys. Union*, 62, 958, 1981.

Nishioka, G.K., and A.J. Michael, A detailed seismicity study of the Middle Mountain zone at Parkfield, California, *Bull. Seismol. Soc. Am.*, 80, 577-588, 1990.

Nur, A., Dilatancy, pore fluids, and premonitory variations of t_s/t_p travel times, *Bull. Seismol. Soc. Am.*, 62, 1217-1222, 1972.

O'Connell, R.J., and B. Budiansky, Seismic velocities in dry and saturated cracked solids, *J. Geophys. Res.*, 79, 5412-5426, 1974.

O'Neill, M.E., Source dimensions and stress drops of small earthquakes near Parkfield, California, *Bull. Seismol. Soc. Am.*, 74, 27-40, 1984.

Okubo, P.G., Dynamic rupture modeling with laboratory-derived constitutive relations, *J. Geophys. Res.*, 94, 12,321-12,335, 1989.

Okubo, P.G., and K. Aki, Fractal geometry of the San Andreas fault system, *J. Geophys. Res.*, 92, 345-355, 1987.

Olson, J.A., Seismicity of the San Andreas Fault Zone in the San Francisco Peninsular area, California, *Bull. Roy. Soc. New Zealand*, 24, 87-97, 1986

Oppenheimer, D.H., Aftershock slip behavior of the 1989 Loma Prieta, California earthquake, *Geophys. Res. Lett*, 17, 1199-1202, 1990.

Page, B.M., The southern Coast Ranges, in *The Geotectonic Development of California*, ed. W.G. Ernst, Prentice Hall, Inc., Englewood Cliffs, New Jersey, 329-417, 1981.

Page, B.M., H.C. Wagner, D.S. McCulloch, E.A. Silver, and J.H. Spotts, Tectonic interpretation of a geological section of the continental margin off San Luis Obispo, the southern Coast Ranges, and the San Joaquin Valley, California: Cross-section summary, *Geol. Soc. Am. Bull.*, 90, 808-812, 1979.

Papageorgiou, A.S., and K. Aki, A specific barrier model for the quantitative description of inhomogeneous faulting and the prediction of strong ground motion. I. Description of the model, *Bull. Seismol. Soc. Am.*, 73, 693-722, 1983a.

Papageorgiou, A.S., and K. Aki, A specific barrier model for the quantitative description of inhomogeneous faulting and the prediction of strong ground motion. Part II. Applications of the model, *Bull. Seismol. Soc. Am.*, 73, 953-978, 1983b.

Poley, C.M., A.G. Lindh, W.H. Bakun, and S.S. Schulz, Temporal changes in microseismicity and creep near Parkfield, California, *Nature*, 327, 134-137, 1987.

Prescott, W.H., and R.O. Burford, Slip on the Sargent fault, *Bull. Seismol. Soc. Am.*, 66, 1013-1016, 1976.

Reasenburg, P.A., and W.L. Ellsworth, Aftershocks of the Coyote Lake, California, earthquake of August 6, 1979: A detailed study, *J. Geophys. Res.*, 87, 10637-10655, 1982.

Reasenberg, P., and D. Oppenheimer, FPFIT, FPPLOT, and FPPAGE: Fortran computer programs for calculating and displaying earthquake fault-plane solutions, *U.S. Geol. Surv., Open File Rept.* 85-739, 1985.

Rice, J.R., and A.L. Ruina, Stability of steady frictional slipping, *J. Appl. Mech.*, 105, 343-349, 1983.

Romanowicz, B., and H. Lyon-Caen, The Loma Prieta earthquake of October 18, 1989: Results of teleseismic mantle and body wave inversion, *Geophys. Res. Lett.*, 17, 1191-1194, 1990.

Ross, D.C., Possible correlations of basement rocks across the San Andreas, San Gregorio-Hosgri, and Rinconada-Reliz-King City faults, California, *U.S. Geol. Surv. Prof. Pap.* 1317, 1984.

Ross, D.C., The Salinian block: A Mesozoic granitic orphan in the California Coast Ranges, in *Mesozoic Paleogeography of the Western United States, Pacific Coast Paleogeography Symposium 2,* Los Angeles, California., Soc. Econ. Paleontologists and Mineralogists, Pacific Section, ed D.G. Howell and K.A. McDougall, 509-522, 1978.

Ross, D.C., Petrographic and chemical reconnaissance study of some granitic and gneissic rocks near the San Andreas fault from Bodega Head to Cajon Pass, California, *U.S. Geol. Surv. Prof. Pap.* 698, 92 p., 1972.

Ross, D.C., Quartz gabbro and anorthositic gabbro: Markers of offset along the San Andreas fault in the California Coast Ranges, *Geol. Soc. Am. Bull.*, 81, 3647-3662, 1970.

Rudnicki, J.W., Physical models of earthquake instability and precursory processes, *Pure and Applied Geophys*, 126, 531-554, 1988.

Rudnicki, J.W., and H. Kanamori, Effects of fault interaction on moment, stress drop, and strain energy release, *J. Geophys. Res.*, 86, 1785-1793, 1981.

Ruina, A.L., Slip instabilty and state variable friction laws, *J. Geophys. Res.*, 88, 10,359-10,3570, 1983.

Sammis, C.G., R.H. Osborne, J.L. Anderson, M. Banerdt, and P. White, Self-similar cataclasis in the formation of fault gouge, *Pure and Applied Geophys*, 124, 53-78, 1986.

Scholz, C.H., *The Mechanics of Earthquakes and Faulting*, Cambridge University Press, Cambridge, 439p., 1990.

Scholz, C.H., and J.T. Engelder, The role of asperity indentation and ploughing in rock friction - I. Asperity creep and stick-slip, *Int. J. Rock Mech. Min. Sci. & Geomech. Abstr.*, 13, 149-154, 1976.

Schulz, S.S., G.M. Mavko, R.O. Burford, and W.D. Stuart, Long-term fault creep observations in central California, *J. Geophys. Res.*, 87, 6977-6982, 1982.

Schwartz, D.P., and K.J. Coppersmith, Fault behaviour and characteristic earthquakes: Examples from the Wasatch and San Andreas faults, *J. Geophys. Res.*, 89, 5681-5698, 1984.

Segall, P., and M. Lisowski, Surface displacements in the 1906 San Francisco and 1989 Loma Prieta earthquakes, *Science*, 250, 1241-1244, 1990.

Segall, P., and D.D. Pollard, Mechanics of discontinuous faults, *J. Geophys. Res.*, 85, 4337-4350, 1980.

Shedlock, K.M., T.M. Brocher, and S.T. Harding, Shallow structure and deformation along the San Andreas fault in Cholame Valley, California, based on high-resolution reflection profiling, *J. Geophys. Res.*, 95, 5003-5020, 1990.

Shimazaki, K., and T. Nakata, Time-predictable recurrence model for large earthquakes, *Geophs. Res. Lett.*, 7, 279-282, 1980.

Sibson, R,. Rupture interaction with fault jogs, in *Earthquake Source Mechanics*, ed. S. Das, J. Boatwright, and C.H. Scholz, American Geophys.Union Monograph No. 37, Washington, D.C., 157-167, 1986.

Sieh, K., Lateral offsets and revised dates of of large prehistoric earthquakes at Pallet Creek, southern California, *J. Geophys. Res.*, 89, 7641-7670, 1984.

Sieh, K., and R. Jahns, Holocene activity of the San Andreas fault at Wallace Creek, California, *Geol. Soc. Am. Bull.*, 95, 883-896, 1984.

Simila, G. W , K. C. McNally, E. Nava, M. Protti-Quesada, and J. Yellin, Evidence of very early aftershock activity along the northwest portion of the 18 October 1989 earthquake rupture zone, *Geophys. Res. Lett* , 17, 1785-1788, 1990.

Sims, J.D., Geologic map of the San Andreas fault zone in the Parkfield 7-1/2 -minute quadrangle, Monterey and Fresno Counties, California, *U.S. Geol. Surv. Misc. Field studies Map* MF 2115, scale 1:24,000, 1990.

Sims, J.D., Chronology of displacement on the San Andreas fault in central California: Evidence from reversed positions of exotic rock bodies near Parkfield, California, *U.S. Geol. Surv. Open File Rept* 89-571, 40 p.,1989.

Sims, J.D, Geologic map of the San Andreas fault zone in the Cholame Valley and Cholame Hills quadrangles, San Luis Obispo and Monterey Counties, California, *U.S. Geol. Surv. Misc. Field studies Map* MF 1995, scale 1:24,000, 1988.

Steidl, J.H., R.J. Archuleta, and S.H. Hartzell, Rupture history of the 1989 Loma Prieta, California, earthquake, *Bull. Seismol. Soc. Am.*, 81, 1573-1602, 1991.

Stesky, R.M., Mechanisms of high temperature frictional sliding in Westerly granite, *Can. J. Earth Sci.*, 15, 361-375, 1978.

Stesky, R.M., W.F. Brace, D.K. Riley, and P.-Y.F. Robin, Friction in faulted rock at high temperature and pressure, *Tectonophysics*, 23, 177-203, 1974.

Stewart, R., and L. Peselnick, Velocity of compressional waves in dry Franciscan rocks to 8 kbar and 300°C, *J. Geophys. Res.*, 82, 2027-2039, 1977.

Stewart, R., and L. Peselnick, Systematic behaviour of compressional velocity in Franciscan rocks at high pressure and temperature, *J. Geophys. Res.*, 82, 2027-2039, 1978.

Stewart, S.W., and M.E. O'Neill, Seismic travel times and near-surface crustal velocity structure bounding the San Andreas fault zone near Parkfield, California, *U.S. Geol. Surv. Prof. Pap.* 800-C, C117-C125, 1972.

Stierman, D.J., Geophysical and geological evidence for fracturing, water circulation and chemical alteration in granitic rocks adjacent to major strike-slip faults, *J. Geophys. Res.*, 89, 5849-5857, 1984.

Tchalenko, J.S., and M. Berberian, Dasht-e-Bayez fault, Iran: Earthquake and related structures in bed rock, *Geol. Soc. Am. Bull.*, 86, 703-709, 1975.

Thatcher, W., Systematic inversion of geodetic data in central California, *J. Geophys. Res.*, 84, 2283-2295, 1979.

Thatcher, W., Strain accumulation and release mechanism of the 1906 San Francisco earthquake, *J. Geophys. Res.*, 80, 4862-4872, 1975.

Thurber, C.H., Earthquake locations and three-dimensional crustal structure in the Coyote Lake area, central California, *J. Geophys. Res.*, 88, 8226-8236, 1983.

Toomey, D.R., and G.R. Foulger, Tomographic inversion for local earthquake data from the Hengill-Grensdalur central volcano complex, Iceland, *J. Geophys. Res.*, 94, 17497-17511, 1989.

Trifunac, M.D., and Udwadia, F.E., Parkfield, California, earthquake of June 27, 1966; A three-dimensional moving dislocation, *Bull. Seismol. Soc. Am.*, 64, 511-533, 1974.

Tse, S.T., and J.R. Rice, Crustal earthquake instability in relation to the depth variation of frictional slip properties, *J. Geophys. Res.*, 91, 9452-9472, 1986.

Tullis, T.E., and J.D. Weeks, Constitutive behavior and stability of frictional sliding in granite,*Pure and Applied Geophys*, 124, 384-414, 1986.

U.S. Geological Survey, *San Francisco Bay Area Earthquakes* , map, 1990.

Wallace, R.E., and H.T. Morris, Characteristics of faults and shear zones in deep mines,*Pure and Applied Geopnys*, 124, 107-125, 1986.

Walter, A.W., and W.D. Mooney, Crustal structure of the Diablo and Gabilan Ranges, central California: A reinterpretation of existing data, *Bull. Seismol. Soc. Am.*, 72, 1567-1590, 1982.

Wang, C-y., On the constitution of the San Andreas fault zone in central California *J. Geophys. Res.*, 89, 5858-5866, 1984.

Wang, C-y., F. Rui, Y. Zhengsheng,and S. Xingjue, Gravity anomaly and deep density structures in the San Andreas fault zone,*Pure and Applied Geophys*, 124, 127-140, 1986.

Wang, C-y., W. Lin, and F.T. Wu, Constitution of the San Andreas fault zone at depth, *Geophys. Res. Lett.*, 5, 741-744, 1978

Wentworth, C.M., R.C. Jachens, R.W. Simpson, and A.J. Michael, Structure of the Parkfield region, CA, from geology and geophysics compiled in a geographic information system, *EOS, Trans. Am. Geophys. Union*, 43, 396, 1992.

Wesson, R.L., R.O Burford, and W.L. Ellsworth, Relationship between seismicity, fault creep, and crustal loading along the central San Andreas fault, in *Proceedings of the Conference on Tectonic Problems of the San Andreas Fault System*, ed. R.L. Kovach and A. Nur, Stanford University Publications in the Geological Sciences, 13, 192-205, 1973.

Whitcomb, J.H., J.D. Garmany, and D.L. Anderson, Earthquake prediction: Variation of seismic velocities before the San Francisco (*sic*) earthquake, *Science*, 180, 632-635, 1973.

Zandt, G., Seismic images of the deep structure of the San Andreas Fault system, central Coast Ranges, California, *J. Geophys. Res.*, 86, 5039-5052, 1981.

DATE

FILMED

9/20/93

END